Numerical Investigation of the Effects of Operational Shock and Disk Surface Pattern on the Dynamics of Head Disk Interface in Hard Disk Drives

by

Liping Li

A dissertation submitted in partial satisfaction of the

requirements of the degree of

Doctor of Philosophy

in

Engineering - Mechanical Engineering

in the

Graduate Division

of the

University of California, Berkeley

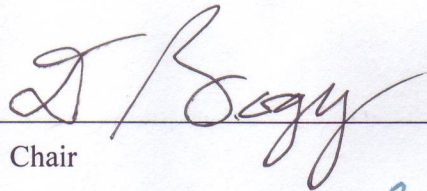Committee in charge:
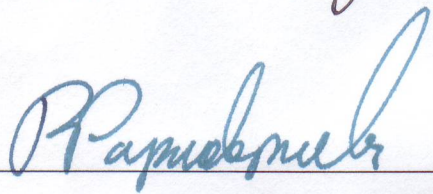
Professor David B. Bogy, Chair
Professor James Casey
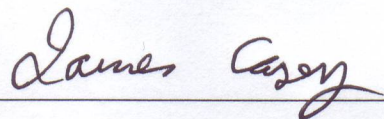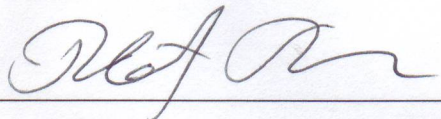Professor Panayiotis Papadopoulos
Professor Per-Olof Persson

Spring 2013

The thesis of Liping Li, titled Numerical Investigation of the Effects of Operational Shock and Disk Surface Pattern on the Dynamics of Head Disk Interface in Hard Disk Drives, is approved:

Chair   May 3, 2013.
         Date

         May 7, 2013
         Date

         9 May 2013
         Date

         5/15/2013
         Date

University of California, Berkeley

Spring 2013

Numerical Investigation of the Effects of Operational Shock and Disk Surface Pattern on the Dynamics of Head Disk Interface in Hard Disk Drives

Abstract

Numerical Investigation of the Effects of Operational Shock and Disk Surface Pattern on the Dynamics of Head Disk Interface in Hard Disk Drives

by

Liping Li

Doctor of Philosophy in Engineering - Mechanical Engineering
University of California, Berkeley

Professor David B. Bogy, Chair

This dissertation investigates the effects of shock and the disk surface pattern on the head disk interface (HDI) response in hard disk drives (HDDs). A new local adaptive mesh method is proposed at the end to improve the accuracy and efficiency of the algorithm to simulate the sliders' steady flying attitudes.

Over the past decades, there has been an increase in the demand of HDDs used in portable devices. In such applications, the work performance of a HDD mainly depends on its ability to withstand external disturbances. Studies of the HDD's responses and failures during external shocks can be very beneficial for improving the HDD's design.

A multi-body operational shock (op-shock) model is developed for this purpose in this thesis. The Guyan reduction method is used to model all the components considered in the op-shock model (a disk, a spindle motor, a base plate, a pivot and a head actuator assembly (HAA)). A fluid dynamic bearing (FDB), between the rotating and stationary units in the spindle motor, is simplified as a spring-dashpot system to save computation efforts. The same simplification is applied to a ball bearing (BB) system between the rotating and stationary units in the actuator pivot. Then the reduced models for all the components are assembled to obtain a complete multi-body op-shock model. Four models which include different components are introduced in this thesis to investigate various components' effects on the HDD's operating performance. The HDDs' failure mechanisms are also studied. It is found that different components influence the HDI responses in different ways.

The ramp load/unload (LUL) technology has been proved to be a better alternative to the contact start-stop (CSS) approach due to the advantages of increasing areal density and greater durability. However, the application of the LUL ramps in the HDDs increases the possibility of collisions between the disk and the ramps since the ramps sit closely to the disk's outer radius. Therefore, it is important to study the ramp effects on the HDD's response during a shock. A reduced model of a deformable ramp is developed and implemented to the multi-body op-shock model. Numerical analyses using three ramp models (no-ramp model, rigid ramp model and deformable ramp model) are carried out to study the HDD's failure dependence on different ramp models.

Bit patterned media (BPM) recording is one of the promising techniques for future disk drives in order to increase the areal density above 4 Tbit/in^2. In patterned media, an individual recorded bit is stored in a distinct magnetic island. Thus, the BPM can change the topography of the disk surface and has an effect on the flying characteristics of the air bearing sliders. Proper designs of sliders and disks in the HDDs are required in order to achieve a stable work performance. So a simulator to model a slider's flying condition over a BPM disk is particularly important. Three methods (the averaging method, the Homogenization method and the Taylor expansion Homogenization methods) are implemented to simulate a slider's flying attitude, and finally an economical accurate method is chosen (the Taylor expansion Homogenization method) to investigate the slider's dynamics on partially planarized patterned media.

In modern HDDs, the requirement of small and steady head disk spacing leads to more complicated air bearing surface designs. Thus it is challenging for an air bearing simulator to accurately capture the pressure under a slider's surface. A new local adaptive grid-generating algorithm is developed and is used to simulate the sliders' steady flying attitude. Local finer meshes (mesh's dimension decreases to half) are created on the nodes of the current grids, which have pressure gradients or geometry gradients larger than a pre-defined tolerance. Two sliders are used to demonstrate the applicability of this method. It is found that this new local adaptive grid-generating method improves the stability and efficiency of the simulation scheme.

To my family

Acknowledgements

First of all, I would like to express my heartfelt gratitude to my research advisor, Professor David B. Bogy, for his support and encouragement during my doctoral studies at UC Berkeley. I am grateful to him for his efforts to direct my research, while at the same time giving me the freedom to explore my research interests. I greatly appreciate his help for my professional and personal development.

I would also like to express my appreciation to Professor James Casey, Professor Panayiotis Papadopoulos, Professor Oliver O'Reilly, and Professor Per-Olof Persson for their valuable contributions and feedbacks to my thesis and my qualify exam.

During my research in the Computer Mechanics Laboratory (CML), I have had an opportunity to discuss my research with members from the hard disk drive industry. I would specially give thanks to Samuel Gan, HongJoo Goh and Joseph HT Lau from Seagate Technologies Singapore for their helpful discussion and feedbacks for my research. I would also like to thank Yiao-Tee Hsia and John Xu from Western Digital Corporation for their support during my internship.

It has been a great pleasure to work with my colleagues at CML: Sean Moseley, Liang Pan, Nan Liu, Sripathi Vangipuram Canchi, Rahul Rai, Jinglin Zheng, Ning Li, Joanna Bechtel, Shaoming Xiong, Yung-kan Chen, Alejandro Rodriguez, Jia Zhao, Yuliang Liu, Dequan Shi and Soroush Sarabi. Research discussion and life sharing with them make my study in CML a wonderful experience. Sincere thanks should be given to Dolf Mardan for helping me with the computer setups required for the work.

Life in Berkeley would not have been so wonderful without my church brothers and sisters: Guiqiao Gan, Royan Yuen, Candice Yuen, Xiaoyan Luo, Anne Chen, Xianzhi Wang, Hui Chen, Hui Zheng, Baoping Liu, Haojun Liu, Hanyu Zhu, Shanshan Ni and Gabriel Tan. They make my life warm and sweet. I would also like to show my gratitude to Diana Willard, Yao Du and Ziman Zhang for support when I was writing this dissertation.

Finally, I should give my heartfelt thanks to my parents, sister and brother for their unconditional love and support throughout my life in Berkeley.

Table of Contents

List of Figures

List of Tables

List of Abbreviations

HDD: Hard Disk Drives
RAMAC: random access method of accounting and control
MB: Megabytes
TB: Terabyte
GB: Gigabyte
RPM: Revolution Per Minute
GMR: Giant Magneto-Resistive
BPM: Bit Patterned Media
HAMR: Heat-Assisted Magnetic Recording
DLC: Diamond Like Carbon
ABS: Air Bearing Surface
VCM: Voice Coil Motor
HAA: Head Actuator Assembly
TFC: Thermal Fly-height Control
R/W: Reading/Writing
op-shock: operational shock
HDI: Head Disk Interface
FE: Finite Element
BB: Ball Bearing
FDB: Fluid Dynamic Bearing
BC: Boundary Conditions
FEM: Finite Element Method
PDE: Partial Differential Equation
DOF: Degree Of Freedom
HGA: Head Gimbal Assembly
LUL: Load/Unload
FFT: Fast Fourier Transform
CSS: Contact Start-Stop
MFH_0: Slider's minimum flying height over an un-patterned disk.
AR: Area Ratio
PH: bit pattern height non-dimensionalized by MFH_0
CVM: Control Volume Method

Chapter 1 Introduction

1.1 The History of Hard Disk Drives

The hard disk drive (HDD) is well known as a data storage device for storing and retrieving digital information to disks or platters. The first HDD, which is called IBM 350 disk storage unit, was introduced in 1956 with the IBM 305 RAMAC (random access method of accounting and control) computer [1]. The 350's cabinet was 60-inch long, 68-inch high and 29-inch deep and weighed over one ton (shown in Figure 1.1) [2]. It had fifty 24-inch diameter disks. Digital information was recorded on both sides of the disk surface, and each surface had 100 tracks. The total capacity of this HDD is 5 million 6-bit characters (3.75 megabytes (MB)). Under the servo control, a pair of heads moved up and down to select a disk and in and out to select a recording track on a pair of disk surfaces [3], which can be simply shown in Figure 1.2. The design of this first generation HDDs was so sophisticated at that time that they needed regular maintenance, so IBM decided to rent the 305 RAMAC system at a rate of $3,200 per month, of which $650 was for the disk storage unit.

A lot of effort was made by IBM in the next two decades to improve the performance of HDDs, such as the introduction of a lighter self-acting air bearing read/write head, the disk spindle and bearings, the head-arm assemblies etc. [4]. In 1973, the first Winchester HDD was introduced, which had almost the same internal structure designs as modern HDDs. The storage capacity could be as high as 70 MB, which was a substantial advance compared with the first HDD generation. This version of HDD is probably the easiest to operate disk storage device at that time, so the customers were able to buy it rather than rent it in November 1973.

Since then, the development of HDDs has been astonishing, due to improvements in the storage capacity, physical volume, price, etc., making it the dominant storage device. The capacity per HDD increases from 3.75 MB in the first generation of HDDs to 4 terabytes (TB) or more. In 2011, Seagate shipped the world's first 4-terabyte external HDD. It is 3.5-inch desktop drive with a rotating speed at 7200 RPM (Revolutions per minute), and the retail price is less than US$250.

Figure 1.3 shows the HDD areal density growth, which is defined as its capacity on an area of one square inch, with the production year [5]. The introduction of the innovation known as giant magneto-resistive (GMR) heads in 1997 advanced the growth rate to 100% until 2001. Continuous increase of HDD areal density requires a smaller and smaller magnetic recording grain size. However, the decrease of grain size approached a limit even the recently introduced perpendicular recording could not avoid, and that is called thermal stability or 'superparamagnetic' limit [6, 7]. To overcome the thermal stability limit and further increase the HDD capacity, some new recording technologies have been proposed, such as bit patterned media (BPM) recording and heat assisted magnetic recording (HAMR) [8,9].

The average price per MB from 1990 to 2015 is plotted in Figure 1.4[5]. The price reduction is as surprising as the capacity increase. Customers can easily buy a 3 TB desktop drive for less than $150 now. Moreover, the disk size has decreased from 24-inch to 3.5-inch and 2.5-inch or even less depending on its application. Nowadays, there are mainly three types of form factors:

3.5-inch for desktop application, 2.5-inch for laptop and netbook application and 1.8-inch for audio players and subnotebooks, among which 3.5-inch and 2.5-inch are the most popular sizes.

Figure 1.1 IBM350 disk storage unit [2]

(1) Heads moved up and down   (2) Head moved in and out
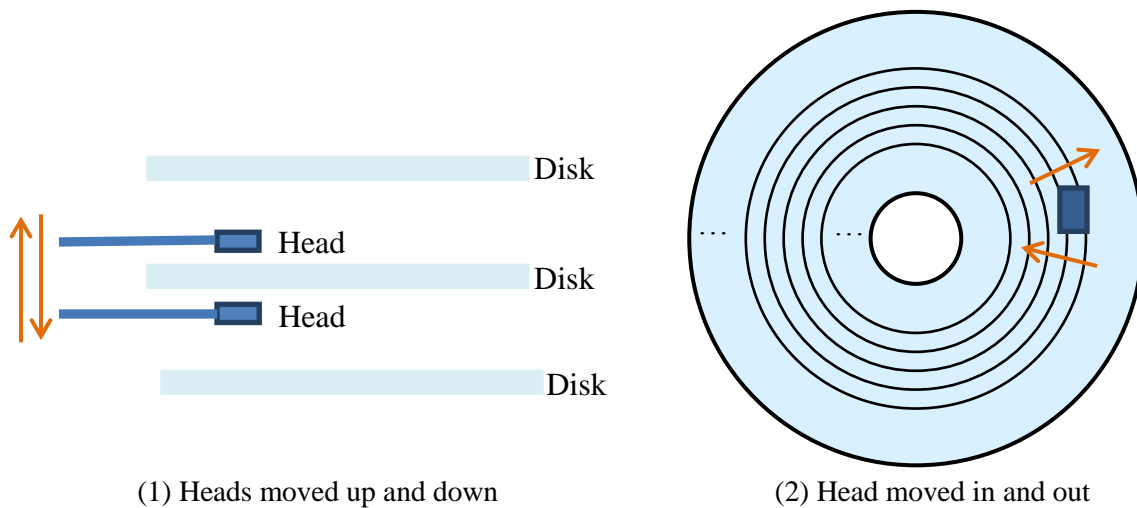
Figure 1.2 IBM350 access mechanism
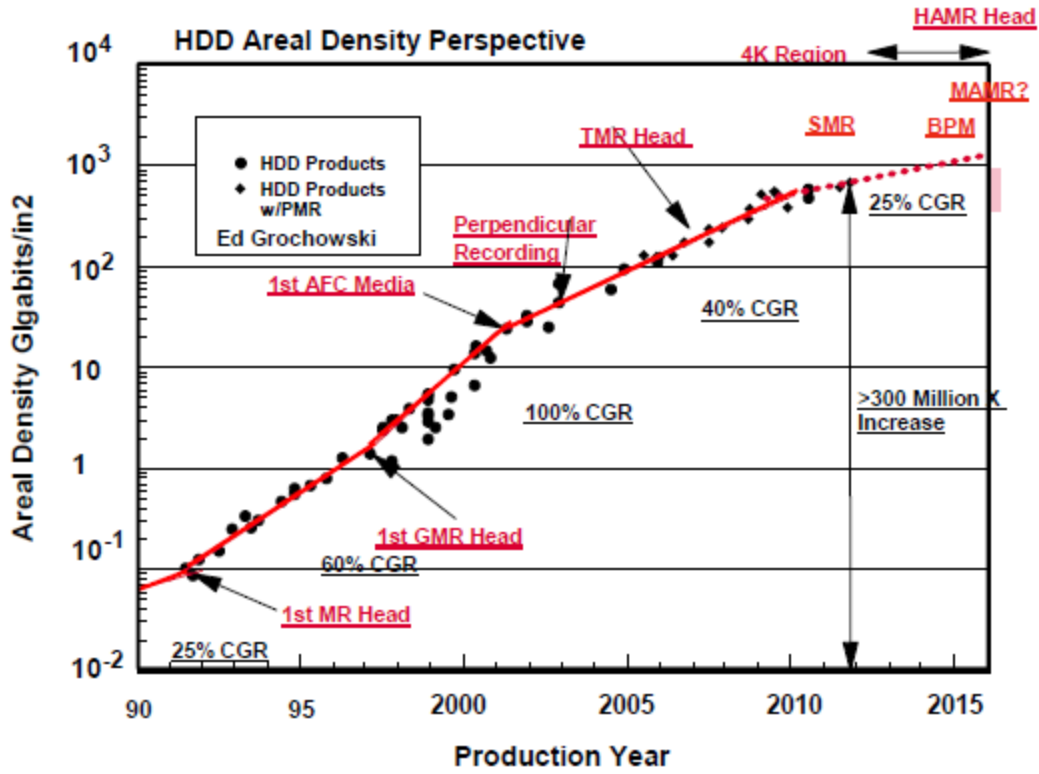
Figure 1.3 HDD areal density growths with production year [5]
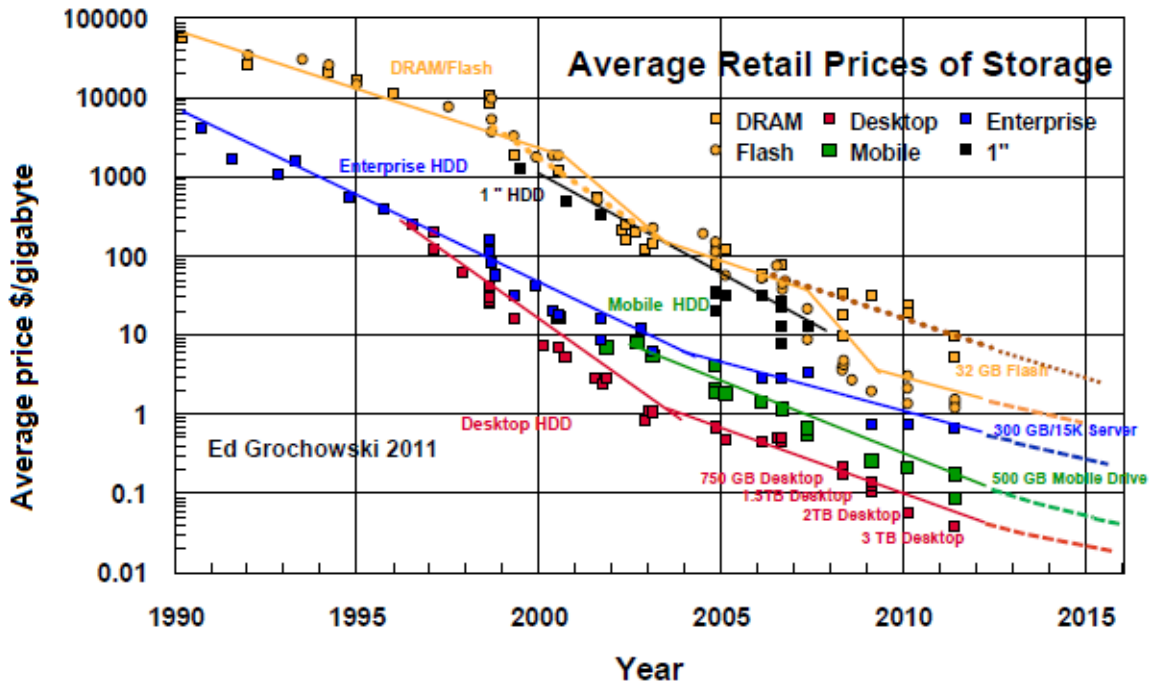
Figure 1.4 Average price per gigabyte (GB) for HDD and flash [5]

1.2 Basics of Modern Hard Disk Drives

To understand how a HDD works, the construction of a sample HDD without its cover is shown in Figure 1.5[10]. Although the HDDs have been improved a lot, the components do not change much in terms of their overall design. A typical HDD includes one or more disks (also called platters), which are usually made of aluminum or glass substrate with multi-layer structures deposited on the top of it (shown in Figure 1.6). The digital information is stored in the magnetic layer. A thin film of diamond-like-carbon (DLC) overcoat is deposited on the top of the magnetic layer in order to protect it from the wear and abrasive impact of a slider. On the top of the overcoat, a thin layer of lubricate is applied to further dampen the occasional tribological contacts between sliders and disks. A slider, which has read/write transducers embedded in it, is attached at the end of a suspension (Figure 1.6). The sliders surface that faces the disk is called the air bearing surface (ABS). A lift force on the ABS, arisen from the air flow between the slider and disk, balances the load provided on the slider by the suspension in order to stabilize the slider's flying condition. The ABS design can be very complicated in current commercial HDDs, and an example of it is shown in Figure 1.7. Different colors indicate different recess depths formed by etching processes. The suspension is mounted to an actuator arm (Figure 1.5). The arm is actuated by a voice coil motor (VCM) so that it can rotate about the actuator axis in
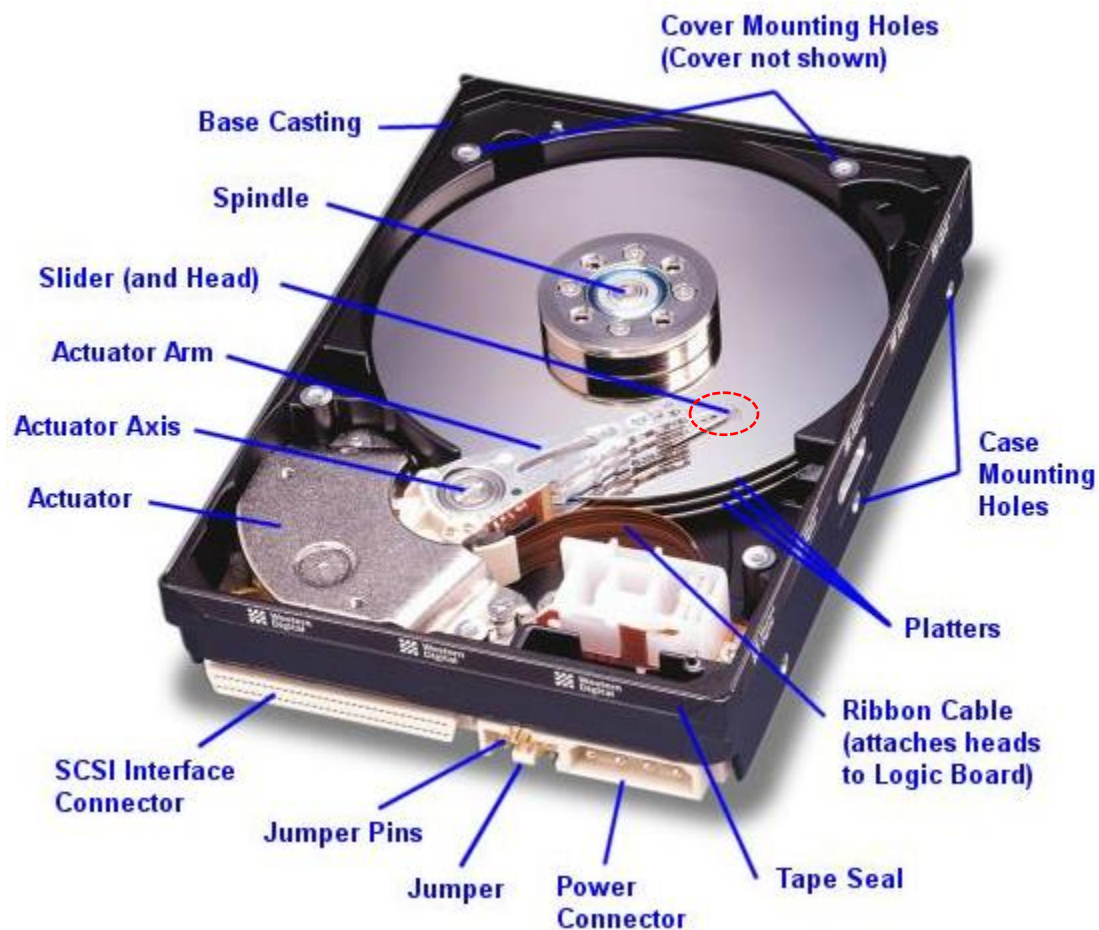
Figure 1.5 Basic constructions of a hard disk drive [10]
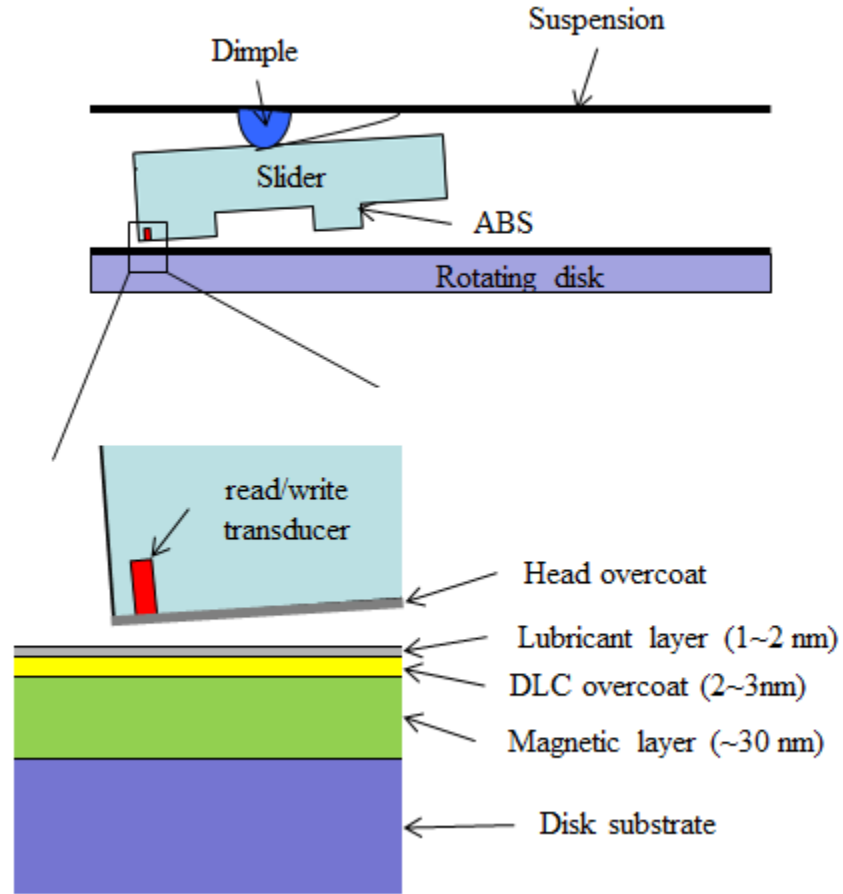
Figure 1.6 An illustration of a slider flying over a rotating disk surface
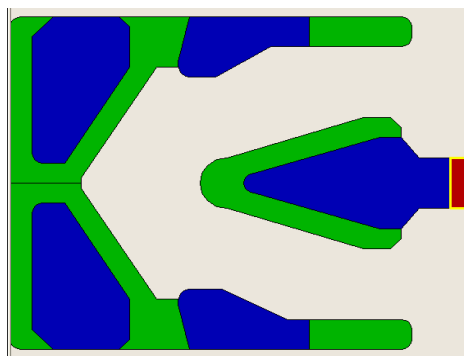
Figure 1.7 An example of ABS design

order to move the slider along a radius to a specific track. The head, suspension, actuator arm and the VCM together are known as the head actuator assembly (HAA). The disks are clamped

on a spindle motor. The spindle and the actuator axis are mounted on a base plate, which is the black case in Figure 1.5.

In most state-of-the-art HDDs, a thermal fly-height control (TFC) technology is used to reduce the head disk spacing and further increase the disk areal density [11,12]. The TFC concept involves a heater element imbedded near the read/write transducer as shown in Figure 1.8. An electrical power is applied to the heater during reading and writing processes, so that there is a local thermal protrusion underneath the transducer (see the red dash curve in Figure 1.8), thus reducing the spacing between the transducer and the disk.
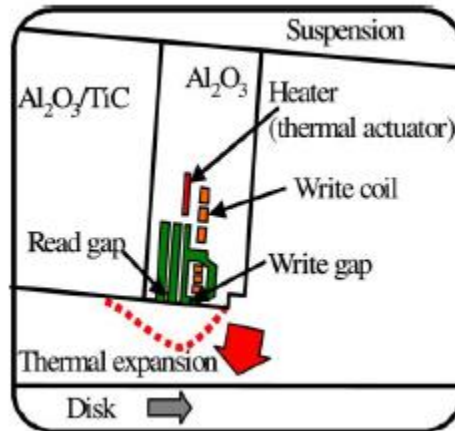
Figure 1.8 Concept of TFC [12]

1.3 Motivation

There has been an increase in the demand of HDDs in the mobile computing devices, such as laptops, digital video recording systems and mp3 players over the past decade. In such applications, the HDDs are often subjected to some harsh working environments, which can degrade the reading/writing (R/W) performance or even lead to the loss of magnetic information. Hence it is crucial to design a robust air bearing system to provide higher operational shock (op-shock) resistance in order to improve the reliability of its working performance. An accurate shock simulator to study the structural and the head disk interface (HDI) response during an op-shock event could be very helpful for this design.

The BPM recording is one of the promising techniques for future disk drives to overcome the superparamagnetic limit to further increase the areal density above 4 Tbit/in^2. In this method, the magnetic layer is created as an ordered array of highly uniform islands, each island capable of storing a bit as shown in Figure 1.9[13], so magnetic transitions no longer occur between random grains; while in conventional media, the magnetic recording layer is a thin film of a magnetic alloy and each recorded bit is made up of many random grains. Thus, BPM is thermally stable at higher density than can be achieved with the conventional media. However, the BPM can change the topography of the disk surface and furthermore has an effect on the flying characteristics of the air bearing sliders. Hence, achieving a stable flying attitude for the slider becomes one of the main considerations for BPM, and a simulator to study the slider's flying condition over a BPM disk becomes desirable.

As the ABS designs in current hard disk drives have complicated rail shapes, multiple etch depths and highly recessed regions between the rails, the pressure distribution between the slider and disk varies greatly under the slider surface. Therefore, a robust numerical scheme is required to solve the generalized lubrication equation efficiently.
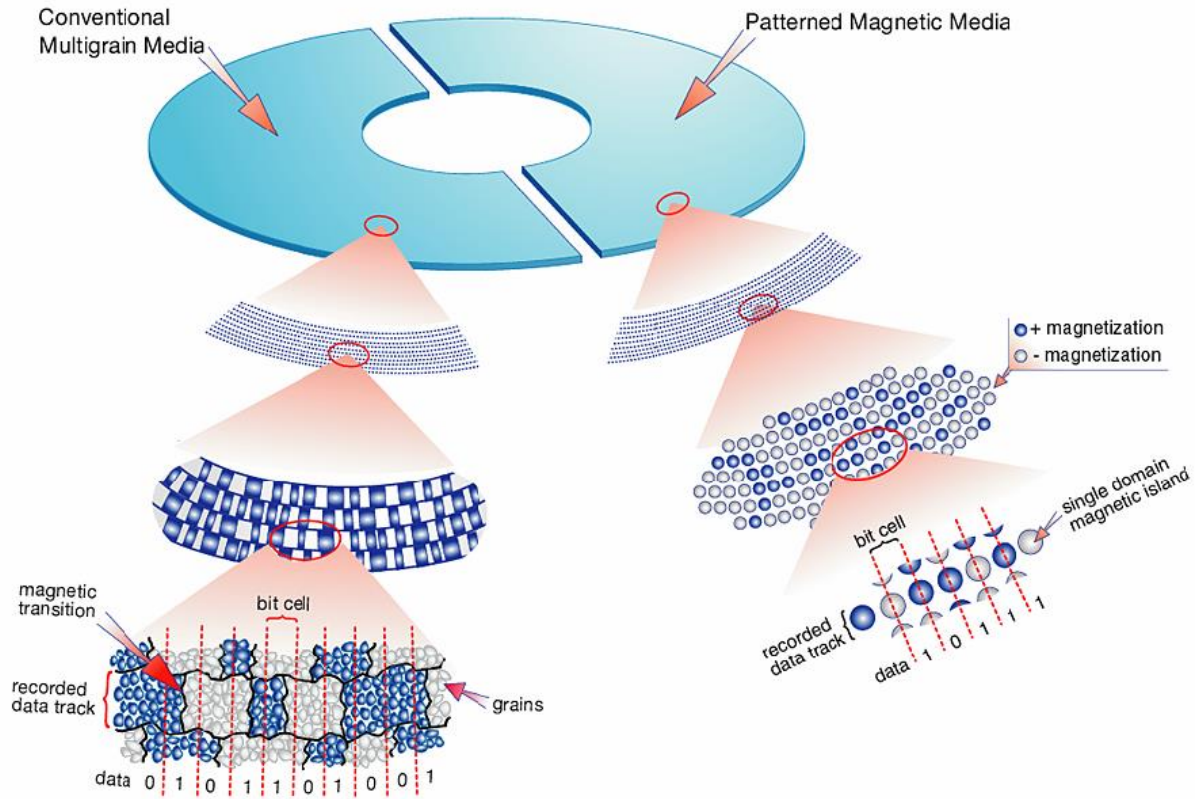
Figure 1.9 Conventional Media vs. Patterned Media [13]

1.4 Objectives and the dissertation outline

In order to investigate the HDI response when a disk drive is under a severe external disturbance or when a slider is flying over a BPM disk, we develop a shock simulator and a BPM simulator in this thesis.

Chapter 2 describes an accurate multi-body op-shock structural model including a spinning disk, a spindle motor, a base plate, a pivot and a HAA. The dynamic analysis of the equation of motion of the structural model is also developed. Some numerical techniques are applied to solve the equation accurately and efficiently, such as Newmark-beta method and block factorization.

In Chapter 3, the op-shock investigations are carried out for four models with different components. The HDI failure mechanisms when a drive is experiencing different shocks are also studied.

Chapter 4 studies the disk-ramp contact during a shock, as the ramp sits near the outer radius of the disk and may affect HDI response.

In Chapter 5, three numerical techniques (Average, Homogenization and Taylor expansion Homogenization methods) are proposed to study a slider's flying attitude when flying over a BPM disk. Then a most economical accurate method is determined among these three, and it is used to study the air bearing dynamics in Chapter 6.

In Chapter 6, the changes of slider's flying attitude when experiencing transitions between different pattern designs are discussed, as well as the air bearing dynamic stability over a BPM disk.

As the ABS designs become more complicated, an effective mesh is very beneficial to capture the air bearing pressure changes under the ABS. A local adaptive mesh method to solve the air bearing governing equation in HDDs is implemented in Chapter 7.

Chapter 8 presents a summary of this dissertation and some suggestions for future work.

Chapter 2 Multi-Body Operational Shock Model in Hard Disk Drives

2.1 Introduction

The arrival of a new generation of portable media and mobile computing devices has increased the demand for the mobile HDDs. In such applications, HDDs are often subjected to some external disturbances which can be modeled as mechanical shocks. Hence it is important to design a robust air bearing systems that can withstand severe external shocks, and numerical studies that znalyze the slider's flying condition and HDD's mechanical response would be very helpful for that purpose.

In order to accurately predict the dynamic response of the HDI in HDDs, it is required to build a model that is not only capable of capturing the true mechanical system as accurately as possible, but is also computational effective. Several researchers [14, 15] used a HDI model, which includes a slider and air bearing model, to predict the HDI response. This model completely fails to tell the dynamics of the suspension and the disk. Over the past two decades, various experimental and numerical studies have been done to investigate the shock response of the mechanical system and its effects on the HDI. However, many of these [16, 17, 18, 19] are limited to the non-operating state of the drives, and/or to the component level. As the head disk spacing has been reduced to just a few nanometers, operating effects become important and cannot be ignored during the shock. Two following studies [20, 21] have considered the operating state. However, they used quite different approaches. In [20], they focused on the air bearing and simplified the suspension and slider as a multiple DOF spring-mass system; while it is opposite in [21], where they built detailed components finite element (FE) models and used linear springs to represent the air bearing stiffness of the HDI.

In 2002, Zeng and Bogy [22] proposed a method considering both a detailed structure model and complete air bearing model. They developed a FE model of the disk-suspension-slider air bearing system, in which the air bearing was modeled as a linear spring, and used it to get the normal load and moments applied on the slider. Then these were used as the input data for the CML dynamic simulator [15] to study the slider's dynamic flying attitude. This procedure was later adopted by Jayson et al. [23] and Murthy et al. [24]. They were able to get the structural response using commercial software and the HDI response by solving the generalized Reynolds equation. However the uncoupled two procedures may lead some inaccuracies of the simulation. Moreover, the iterations between the structural and air bearing simulations can make the process computationally expensive.

In an alternative approach, Yap et al. [25] and Liu et al. [26] developed a flexible multi-body dynamics formulation to analyze the HDD's shock response. The main components, including the VCM, the HAA, the disk-spindle system, the shafts and the housing, were considered as flexible parts connected by bearing joints such as ball bearings (BB), fluid dynamic bearings (FDB), or air bearing. The air pressure between the slider and the disk is obtained by solving the steady state Reynolds equation in order to form an air pressure table, which is used to model the nonlinear air bearing. However, they did not provide analysis to the flexible structure base plate. A following study by Liu et al. [27] added a base plate to their previous work [26]. They

investigated the effect of the base stiffness on the shock tolerance of the HDD, and it was found that a stiffer base would benefit to improve the HDDs' working performance during a shock. They showed that this multi-body dynamics formation method is significantly faster than a full FE approach. However, the disk-slider contact model is not included in their model.

A new coupled structural-fluid model, proposed by Bhargava et al. [28], is used to simulate an op-shock response of a disk-suspension-slider air bearing system. The mass and stiffness matrices of the disk and the suspension were first exported from a commercial FE software ANSYS, and then imported to a modified CML dynamic simulator, which solves the air bearing equation of the system. This procedure solves the structural and air bearing problems simultaneously, so it is convenient for practical application as well as accurate. However, the disk is considered as stationary, which is only applicable when the system is subjected to an axisymmetric shock. Rai et al. [29] applied a spinning disk model to the coupled structural-fluid model [28] to simulate non-axisymmetric disturbances. Moreover, some important disk drive components, such as spindle motor and base plate, are considered in this modified structural-fluid model in order to calculate the shock response more accurately. However, in this model the HAA was assumed to be mounted on a fixed support and hence the flexibility of the base plate effects on the HAA was neglected.

In this chapter, we will extend the work on the structural-fluid model [29] by adding another component pivot so that we can account for the base plate effects on the dynamics of the HAA.

2.2 Multi-Body System Modeling in Hard Disk Drives
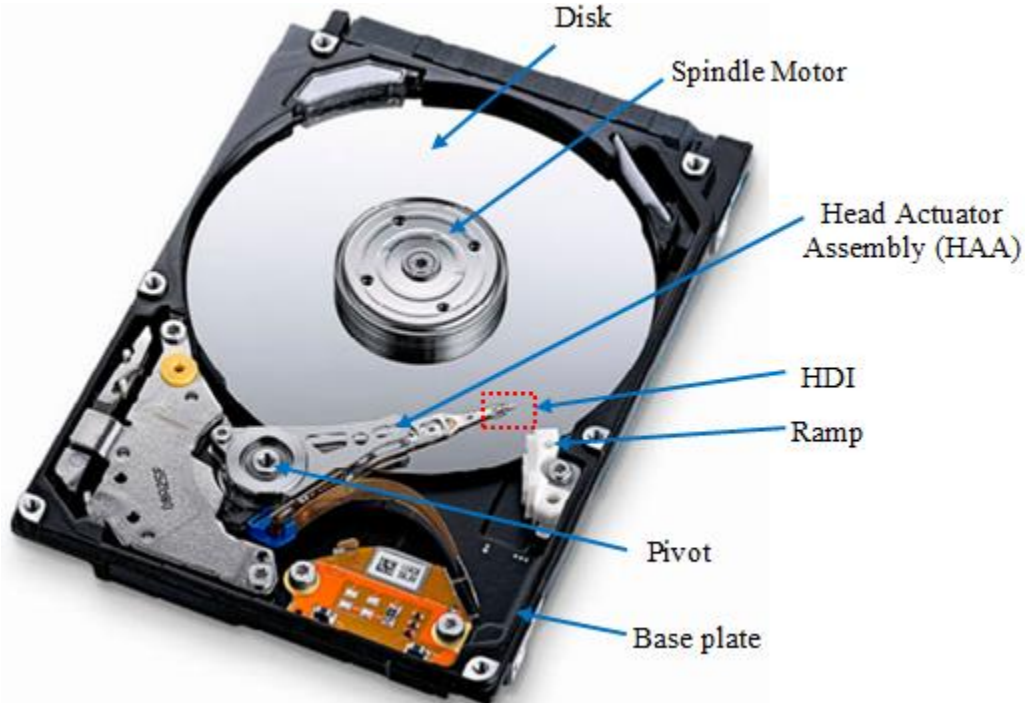
Figure 2.1 The mainly components of a hard disk drive [30]

The structural components we considered in this structural-fluid multi-body model include: a HAA, a pivot, a base plate, a spindle motor, a disk and a HDI. The integration of them is shown in Figure 2.1. The HDI in a mobile drive consists of a slider, a spinning disk and an air bearing coupling these two components. Hence the stability of the HDI strongly depends on the dynamic response of the structural components in a HDD.

2.2.1 Disk

The earliest study on the vibration of a spinning elastic disk is the classical work by Lamb and Southwell [31], who derived the linearized equation of transverse deflection and identified the respective contribution of the bending stress and in-plane stress. In that paper and a later work by Southwell [32], they presented the frequencies and modes of a free vibration for complete disks. A more thorough presentation of the Lamb and Southwell results was shown by Prescott [33]. In that book, it extends the analyses to disks with different clamping geometries and cross sections. Iwan and Stahl [34] investigated the dynamic response of a circular elastic disk excited by a moving load. In this study, the load is distributed over a small portion of the disk and is represented by a mass, spring and dashpot. The stability of a spinning disk with a stationary transverse load was studied by Iwan and Moeller [35]. Similar to [34], the load is also modeled as a mass-spring- dashpot in [35]. Vibrations of a spinning disk when subject to a stationary point load was investigated by Benson [36], in which the analytical approach to study the dynamics of a spinning disk considering and without considering the bending stiffness are presented. In this thesis, we use a finite element method (FEM) to study the vibration of a spinning disk when it is subject to a uniform load on the whole disk surface.

In polar coordinates (r, θ), the governing equation for the transverse displacement (w) of a spinning disk with an angular velocity Ω (Figure 2.2) is as follows:
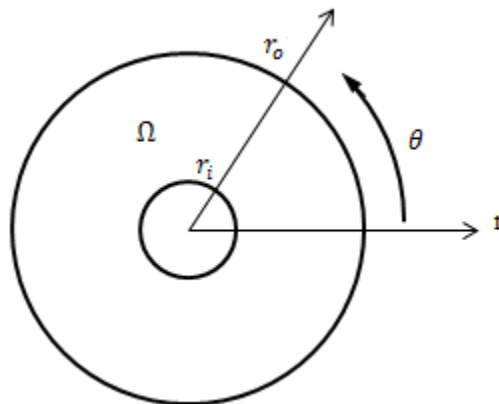
Figure 2.2 A schematic of a spinning disk

$$\rho h \left(\frac{\partial^2 w}{\partial t^2} + 2\Omega \frac{\partial^2 w}{\partial t \partial \theta} + \Omega^2 \frac{\partial^2 w}{\partial \theta^2} \right) + D\nabla^4 w - \frac{\partial}{r \partial r}\left(r q_r \frac{\partial w}{\partial r} \right) - \frac{\partial}{r \partial \theta}\left(q_\theta \frac{\partial w}{r \partial \theta} \right) = p(r, \theta, t), \quad (2.1)$$

where ρ is the disk density, h is the thickness and $D = Eh^3/(12(1 - v^2))$ is the flexural rigidity of the disk, respectively. $p(r, \theta, t)$ is the external pressure applied to the disk. q_r and q_θ are the

linearized internal forces in the radial and circumferential directions, which have the following expressions:

$$q_r = \left(\frac{Eh}{12(1-v^2)}\right)\left(\frac{\partial u}{\partial r} + v\frac{u}{r}\right), \tag{2.2}$$

$$q_\theta = \left(\frac{Eh}{12(1-v^2)}\right)\left(\frac{u}{r} + v\frac{\partial u}{\partial r}\right), \tag{2.3}$$

where u is the steady disk in-plane displacement governed by the equation:

$$\rho h \Omega^2 r + \frac{\partial q_r}{\partial r} + \frac{q_r - q_\theta}{r} = 0, \tag{2.4}$$

The boundary conditions (BCs) for the disk with free outer radius are given as follows:

$$M_{rr} = -D\left[\frac{\partial^2 w}{\partial r^2} + \frac{v}{r}\left(\frac{\partial w}{\partial r} + \frac{1}{r}\frac{\partial^2 w}{\partial \theta^2}\right)\right]|_{r=r_o} = 0, \tag{2.5}$$

$$V_r = -D\left[\frac{\partial \nabla^2 w}{\partial r} + \frac{(1-v)}{r^2}\frac{\partial^2}{\partial \theta^2}\left(\frac{\partial w}{\partial r} - \frac{w}{r}\right)\right]|_{r=r_o} = 0, \tag{2.6}$$

where M_{rr} is the bending moment and V_r is the shear force[37]. As the disk inner radius is clamped on the spindle motor, we also have the following boundary condition at $r = r_i$:

$$\frac{\partial w}{\partial r}|_{r=r_i} = 0. \tag{2.7}$$

The displacement at inner radius should also be equal to the spindle motor's interfacial displacement given in Eqn. (2.28).

The FEM is used to get an approximate solution for the disk deformation under a generalized load. Firstly, a weak form needs to be developed for the partial differential equation (PDE) Eqn. (2.1). As the PDE involves a fourth order differentiation, we choose a test function:

$$\tilde{w}(r,\theta) \in W = \left\{\tilde{w} \in H^2(\Omega) \mid \frac{\partial \tilde{w}}{\partial r}|_{r=r_i} = 0\right\}. \tag{2.8}$$

Multiply $\tilde{w}$ on both sides of Eqn. (2.1) and its BCs, and then integrate them over the disk area and outer radius, respectively:

$$\int_\Omega \tilde{w}\left[\rho h\left(\frac{\partial^2 w}{\partial t^2} + 2\Omega\frac{\partial^2 w}{\partial t \partial \theta} + \Omega^2\frac{\partial^2 w}{\partial \theta^2}\right) + D\nabla^4 w - \frac{\partial}{r\partial r}\left(rq_r\frac{\partial w}{\partial r}\right) - \frac{\partial}{r\partial \theta}\left(q_\theta\frac{\partial w}{r\partial \theta}\right) - p\right]dA +$$
$$\tilde{w}\left[\frac{\partial^2 w}{\partial r^2} + \frac{v}{r}\left(\frac{\partial w}{\partial r} + \frac{1}{r}\frac{\partial^2 w}{\partial \theta^2}\right)\right]|_{r=r_o} + \tilde{w}\left[\frac{\partial \nabla^2 w}{\partial r} + \frac{(1-v)}{r^2}\frac{\partial^2}{\partial \theta^2}\left(\frac{\partial w}{\partial r} - \frac{w}{r}\right)\right]|_{r=r_o} = 0. \tag{2.9}$$

A special annular planar element that conforms to the disk's geometry is used for the spatial discretization (Figure 2.3) and degrees of freedom (DOFs) of one element are: $\left\{(w)_1, \left(\frac{\partial w}{\partial r}\right)_1, \left(\frac{\partial w}{\partial \theta}\right)_1, \left(\frac{\partial^2 w}{\partial r \partial \theta}\right)_1, \dots, (w)_4, \left(\frac{\partial w}{\partial r}\right)_4, \left(\frac{\partial w}{\partial \theta}\right)_4, \left(\frac{\partial^2 w}{\partial r \partial \theta}\right)_4\right\}.$

After some algebra calculation and simplification (more details were presented in Rai [38]), the weak form Eqn. (2.9) can be finally written as a set of standard dynamic equations of motion:

$$[M_{disk}]\{\ddot{w}\} + [C_{disk}^{gyro}]\{\dot{w}\} + [K_{disk}]\{w\} = \{F_{disk}\}, \qquad (2.10)$$

where M_{disk}, C_{disk}^{gyro} and K_{disk} are the disk's inertia, gyroscopic and stiffness matrices respectively. w is the unknown DOF vector and $\{F_{disk}\}$ is the external load vector applied on the disk.

The intrinsic damping effect is modeled using the proportional damping method, which can be written as:

$$[C_{disk}^{prop}] = \alpha_1 [M_{disk}] + \alpha_2 [K_{disk}], \qquad (2.11)$$

where α_1 and α_2 are damping coefficients that are chosen such that the damping values at 10 Hz and 50 kHz are 2%. So the disk damping matrix can be calculated in the form:

$$[C_{disk}] = [C_{disk}^{prop}] + [C_{disk}^{gyro}]. \qquad (2.12)$$

And the final dynamic equation of motion for the disk is:

$$[M_{disk}]\{\ddot{w}\} + [C_{disk}]\{\dot{w}\} + [K_{disk}]\{w\} = \{F_{disk}\}. \qquad (2.13)$$
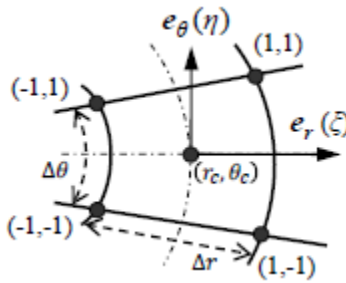
Figure 2.3 An annular planar element [38]

2.2.2 Spindle Motor

The spindle motor is responsible for spinning the hard disks when a HDD is working. A typical HDD spindle system has the structure shown in Figure 2.4 [39]. The spindle motor mainly consists of a rotating hub and a stationary housing. The FDB is used to reduce the friction between the rotating part and the stationary part in the spindle motor.

The FEM is used to calculate the response of the structural units in the spindle motor. Due to the large number of DOFs (~100000) in the FE structural model, a Guyan FE reduction method [40] is used to save the computational time. Here number of DOFs is reduced while retaining the low frequency response of the system. In this method, the master DOFs are selected based on the criterion proposed by Shah and Raymund [41]. However, the DOFs presented at the FDB locations on the hub and housing surface are always selected as the master DOFs in order to

evaluate the response of the FDB, even if those DOFs violate the selection criterion. The equations of motion for the reduced hub and housing models can be written as:

$$[M_{hub}]\{\ddot{u}^{hub}\} + [C_{hub}]\{\dot{u}^{hub}\} + [K_{hub}]\{u^{hub}\} = \{F_{hub}\}, \tag{2.14}$$

$$[M_{hsng}]\{\ddot{u}^{hsng}\} + [C_{hsng}]\{\dot{u}^{hsng}\} + [K_{hsng}]\{u^{hsng}\} = \{F_{hsng}\}, \tag{2.15}$$

where $\{u^{hub}\}$ and $\{u^{hsng}\}$ are the displacements $(u_x, u_x, u_x)^T$ of the final reduced hub and housing models, respectively.
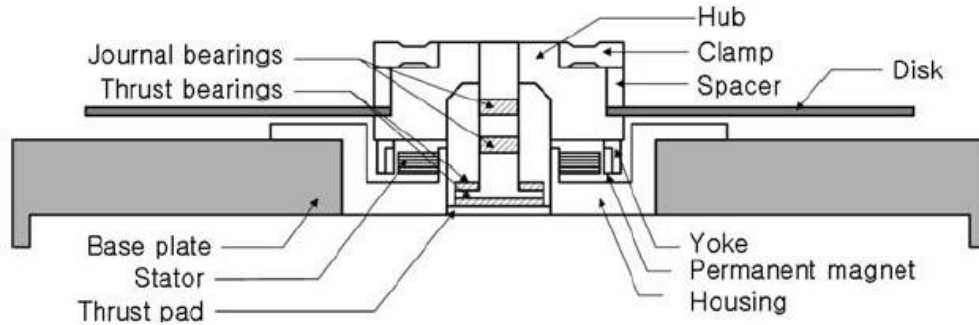
Figure 2.4 HDD spindle systems [39]

The FDBs in a spindle motor usually include journal and thrust bearings, which are differentiated based on their load carrying components (Figure 2.4). The journal bearing carries the radial load while the thrust bearing supports the axial load. These two kinds of bearings are governed by the two sets of Reynolds equation [42]:

$$\frac{\partial}{R\partial\theta}\left(\frac{h^3}{12\mu}\frac{\partial p}{R\partial\theta}\right) + \frac{\partial}{\partial z}\left(\frac{h^3}{12\mu}\frac{\partial p}{\partial z}\right) = \frac{\Omega}{2}\frac{\partial h}{\partial\theta} + \frac{\partial h}{\partial t}, \tag{2.16}$$

$$\frac{\partial}{r\partial r}\left(r\frac{h^3}{12\mu}\frac{\partial p}{\partial r}\right) + \frac{\partial}{r\partial\theta}\left(\frac{h^3}{12\mu}\frac{\partial p}{r\partial\theta}\right) = -\frac{r\Omega}{2}\frac{\partial h}{r\partial\theta} + \frac{\partial h}{\partial t}, \tag{2.17}$$

where p, h, μ, R and Ω are the bearing pressure, thickness, viscosity coefficient, radius of journal and angular speed of shaft, respectively. (θ, z) and (r, θ) are two sets of coordinate systems. Solving the above two equations to get the reaction force at the FDBs is very time consuming. One approach is to simplify the FDBs as spring-dashpot systems (Figure 2.5[38]). The damping and stiffness coefficients for the simplified models are calculated by solving the perturbed Reynolds equations. More details of how to evaluate the coefficients can be found in [42] and [38]. So the reaction forces on the hub (f^{r_1}) and housing (f^s) due to the deformation of the FDBs can be written as:

$$f^{r_1} = -f^s = -K_{FDB}(u^{r_1} - u^s) - C_{FDB}(\dot{u}^{r_1} - \dot{u}^s), \tag{2.18}$$

where $\boldsymbol{u}^{r_1} = (u_x^{r_1}, u_y^{r_1}, u_z^{r_1})^T$ and $\boldsymbol{u}^s = (u_x^s, u_y^s, u_z^s)^T$ are the displacements of the hub (rotating unit) and housing (stationary unit) at the FDB locations, respectively. $\boldsymbol{K}_{FDB}$ and $\boldsymbol{C}_{FDB}$ are the equivalent FDB stiffness and damping coefficient matrices.

a) Side View   b) Top View
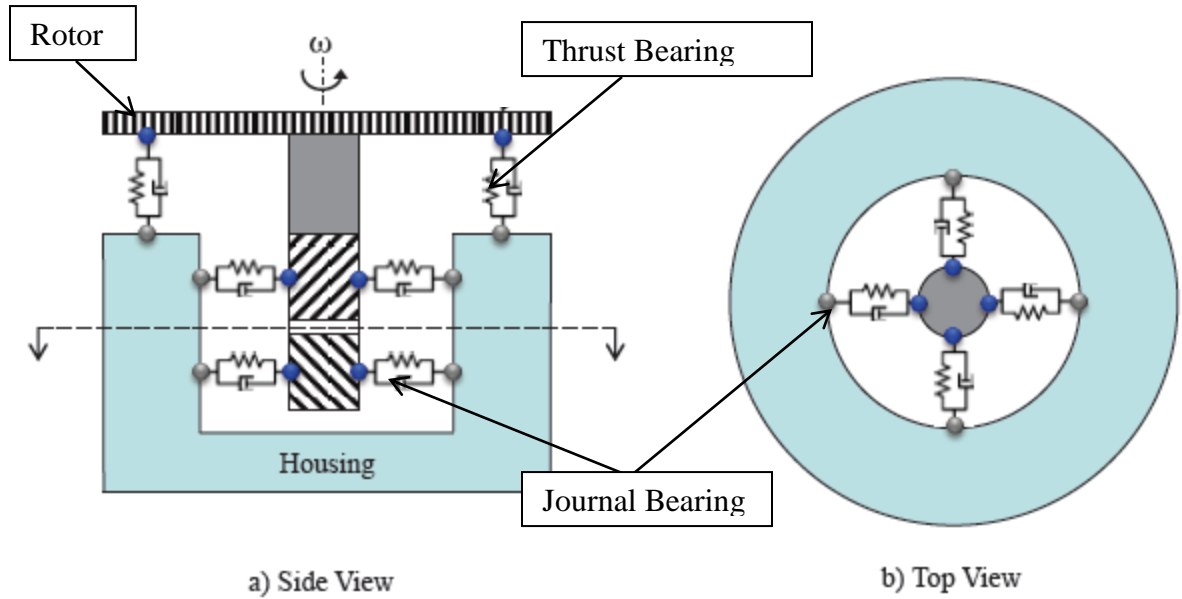
Figure 2.5 Simplified spring-dashpot model equivalent to the FDBs [38]

2.2.3 Base Plate

The base plate is the black casing shown in Figure 2.1, having the disks rotatably mounted on it, and the HAA pivotally installed to it. The FE reduction method is also applied to model the dynamics of the base plate:

$$[M_{base}]\{\ddot{u}^{base}\} + [C_{base}]\{\dot{u}^{base}\} + [K_{base}]\{u^{base}\} = \{F_{base}\}, \qquad (2.19)$$

where $\{\boldsymbol{u}^{base}\}$ is the displacement of the final reduced base plate model.

2.2.4 Pivot

The HAA is mounted to the base plate via a pivot. A particular design of a pivot consists of a shaft, two sets of balls and a sleeve (Figure 2.6[43]). It is attached to the HAA by a screw or a clip. The pivot is connected to the base plate through its shaft. The FE reduced form for the dynamics of the pivot shaft and sleeve can be written as:

$$[M_{shft}]\{\ddot{u}^{shft}\} + [C_{shft}]\{\dot{u}^{shft}\} + [K_{shft}]\{u^{shft}\} = \{F_{shft}\}, \qquad (2.20)$$

$$[M_{slev}]\{\ddot{u}^{slev}\} + [C_{slev}]\{\dot{u}^{slev}\} + [K_{slev}]\{u^{slev}\} = \{F_{slev}\}, \qquad (2.21)$$

where $\{\boldsymbol{u}^{shft}\}$ and $\{\boldsymbol{u}^{slev}\}$ are the displacements of the reduced shaft and sleeve models, respectively.

Ball bearings are used to reduce the friction between the pivot shaft and sleeve. The non-linearity of the BB effects makes it very complicated to calculate the reaction between the BB and pivot units. Similar to the FDB model, we use spring-dashpot systems to simplify the BB effects (Figure 2.7). The damping and stiffness coefficients for the simplified models are obtained by experiments. It should be noted that the damping and stiffness both have two

components: one is the axial component and the other is the radial component. The reaction forces on the shaft (f^s) and sleeve (f^{r_2}) due to the deformation of the BBs can be written as:

$$f^s = -f^{r_2} = -K_{BB}(u^s - u^{r_2}) - C_{BB}(\dot{u}^s - \dot{u}^{r_2}),\qquad(2.22)$$

where $\boldsymbol{u}^s = (u_x^s, u_y^s, u_z^s)$ and $\boldsymbol{u}^{r_2} = (u_x^{r_2}, u_y^{r_2}, u_z^{r_2})$ are the displacements of the shaft (stationary unit) and sleeve (rotating unit) at the BB locations, respectively. $\boldsymbol{K}_{BB}$ and $\boldsymbol{C}_{BB}$ are the equivalent BB stiffness and damping coefficient matrices.
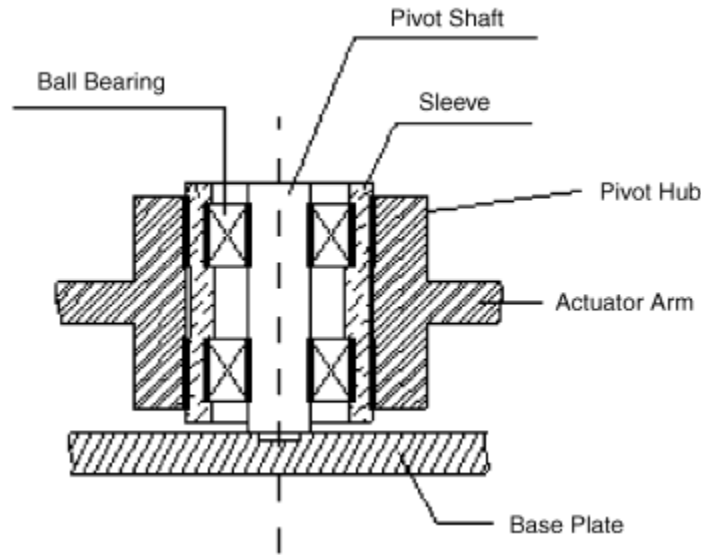
Figure 2.6 Cross-section of a pivot [43]
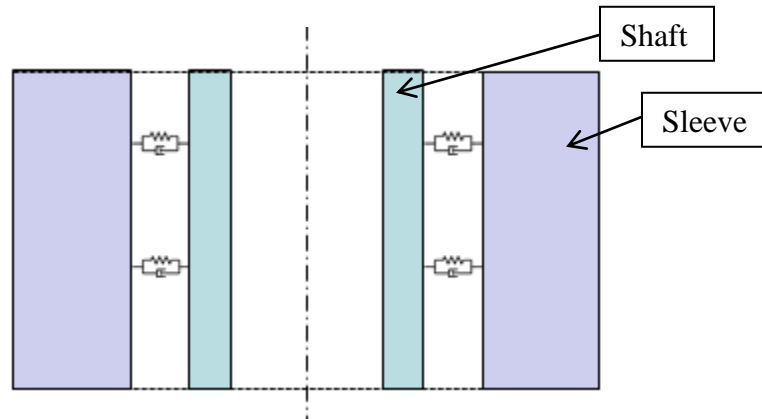
Figure 2.7 Simplified spring-dashpot model equivalent to the BBs

2.2.5 Head Actuator Assembly (HAA)

The HAA includes a head gimbal assembly (HGA), an actuator arm and a VCM. The HGA is used to load a slider to or unload it from a rotating disk. The schematic of a HGA is shown in Figure 2.8. The slider is attached to the flexure of the suspension and is pressed in proximity to the disk by the load beam through the dimple during the loading process. During the unloading process, the LUL (load/unload) tab moves onto a parking ramp and pulls the slider up from the

disk. Due to the negative air bearing developed underneath the slider, the slider will be pulled back to the disk, and the dimple contact will be opened up. The limiter is designed to control the maximum gap between the load beam and the flexure beam, as the spring-back action of the slider will damage the HGA system if the separation between the two beams keeps increasing. The opening of the dimple and engaging of limiters also occur during the op-shock event. We use a FE reduction method to model the response of the HAA. A technique proposed by Hughes et al. [44] is used to model the contact between the pairs during the opening and engaging of the dimple and the limiters. The dynamic equation of motion of the HAA is written as:

$$[M_{HAA}]\{\ddot{u}^{HAA}\} + [C_{HAA}]\{\dot{u}^{HAA}\} + [K_{HAA}]\{u^{HAA}\} = \{F_{HAA}\}, \tag{2.23}$$

where $\{u^{HAA}\}$ is the displacement of the reduced HAA model.
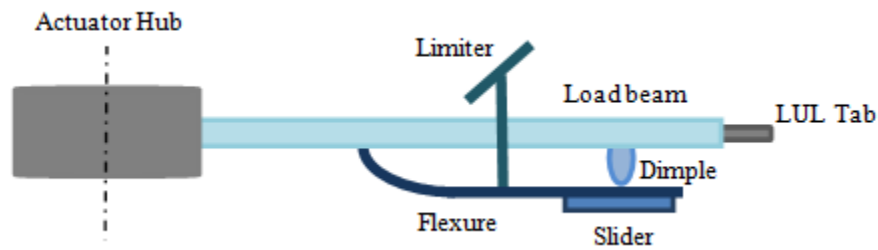
Figure 2.8 A schematic diagram of a head gimbal

2.2.6 Air Bearing

The robustness of the air bearing between the slider and the disk strongly determines the work performance of the HDDs during an op-shock event. In order to get a satisfactory HDI response, it is essential to accurately capture the dynamic behavior of the air bearing during the disturbance. Figure 2.9 shows a schematic of a slider flying over a disk. The slider, included in the HAA model, is represented by a mass element which has 6-DOF: translations in the x, y and z directions and rotations about the nodal x, y, and z axes. The C ML dynamic program [15] treats the slider as a separate rigid body with 3-DOF as will be seen in Chapter 5.
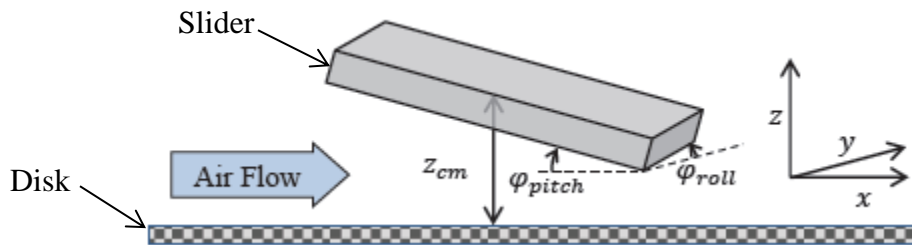
Figure 2.9 Slider flying over a spinning disk [38]

The air flow between the slider and the disk is governed by the generalized Reynolds equation:

$$\frac{\partial}{\partial X}\left(Q(K_n)PH^3\frac{\partial P}{\partial X} - \Lambda_x PH\right) + \frac{\partial}{\partial Y}\left(Q(K_n)PH^3\frac{\partial P}{\partial Y} - \Lambda_Y PH\right) = \sigma\frac{\partial(PH)}{\partial T}, \tag{2.24}$$

where $P = p/p_a$, $H = h/h_m$, $X=x/L$, $Y=y/L$ and $T=\omega t$ are the dimensionless pressure, bearing clearance, coordinates in the slider's length and width directions and time respectively; p_a is the ambient atmospheric pressure; h_m is the reference clearance at the trailing edge center; L is the length of the slider; ω is the disk rotating angular frequency. $\Lambda_x = 6\mu UL/p_a h_m^2$ and $\Lambda_y = 6\mu VL/p_a h_m^2$ are the bearing numbers in the x and y directions; μ is the viscosity of the air; U and V are the velocity components of the rotating disk surface in the x and y directions. $Q(K_n)$ is the Poiseuille flow factor to accommodate the slip effect at the boundary using Fukui and Kaneko correction [45,46] and K_n is the Knudsen number, which is defined as the ratio of the air mean free path to the local clearance. $\sigma = 12\mu\omega L^2/p_a h_m^2$ is the squeeze number.

As the clearance between the slider and the disk continues to reduce to less than 5 nm in modern HDDs, some interfacial forces, like intermolecular force, electrostatic force and contact force, become significant and will affect the HDI response.

The intermolecular potential for two molecules is the summation of the attractive and repulsive components. The total potential between the disk and the slider is obtained by integrating the potential per unit area over the slider surface. The intermolecular force between the slider and disk can be expressed as [47, 48]:

$$f_{IMF} = -\frac{d(U_{IMF\ Total})}{dz} = -\frac{A}{6\pi} \iint \frac{dxdy}{z^3} + \frac{B}{45\pi} \iint \frac{dxdy}{z^9} , \qquad (2.25)$$

where A and B are the Hamaker constants, which depend on the dielectric constant and refractive index of the media. Typical values for A and B are about 10^{-19} J and 10^{-76} J·m^6, respectively.

Tribocharging phenomenon [49] appears when the slider flies very close to the disk so that a charge will be built up on the surfaces of the slider and the disk. The potential difference developed between the slider and the disk produces an electrostatic force, which has the following formulation:

$$f_{Elec} = -\frac{d(Elec)}{dz} = -\frac{\epsilon_0 \kappa_e V^2}{2} \iint \frac{dxdy}{z^2} , \qquad (2.26)$$

where ϵ_0, κ_e and V are the permittivity constant, dielectric constant for air and potential difference between the slider and the disk.

As the surfaces of the slider and disk are not perfectly smooth, asperity contact occurs when the head disk spacing reduces to a certain value. The Greenwood-Williamson method [50] is used to calculate the contact force arising between the slider and disk. In this model, the asperities are assumed to have the same radius of curvature but statistical distribution of asperity height. The asperity contact force is evaluated by the Hertzian contact model:

$$f_c = \frac{4}{3} E^* R^{1/2} \omega^{3/2} , \qquad (2.27)$$

where E^* is Hertz elastic modulus of the contact surfaces, R is the radius of curvature of the asperity and ω is the depth of indentation.

The failure of the HDI is usually caused by a collision between the slider and the disk. The impact force during the collision is solved by a semi-analytical method proposed by Bhargava [51]. In this approach, the interaction between the slider and the disk is modeled as the Boussinesq problem, in which the displacement u in the half space is determined by the concentrated force F applied on the surface. The boundary element method is used to solve the inverse problem to obtain the contact pressure for a given disk deformation profile.

2.3 System Assembly

In a HDD, the disk is clamped on the hub of the spindle motor; the spindle motor is mounted on the base plate; the HAA is connected to the pivot, and the pivot is attached to the base plate. So all these components are assembled and can be divided into three parts according to their rotating and stationary characteristics: rotating part I which includes the spinning disk and the rotor (hub); stationary part consisting of the motor housing, the base plate and the pivot shaft; rotating part II including the pivot sleeve and the HAA. The compatibility conditions for the three parts are shown in Figure 2.10-2.12.

For rotating part I, the compatibility condition is

$$\{w_i^{disk}\} = \{w_i^{hub}\}, \tag{2.28}$$

where $\{w_i^{disk}\}$ and $\{w_i^{hub}\}$ are the z displacements of the disk-hub interfacial nodes (Figure 2.10). Applying Eqn. (2.28), we can combine the dynamic equation of motion for the spinning disk (Eqn. (2.13)) and the hub (Eqn. (2.14)):

$$\begin{bmatrix} M_{oo}^d & M_{oi}^d & 0 \\ M_{io}^d & M_{ii}^d + M_{ii}^h & M_{io}^h \\ 0 & M_{oi}^h & M_{oo}^h \end{bmatrix} \begin{Bmatrix} \ddot{w}_o^d \\ \ddot{w}_i^d \\ \ddot{u}_o^h \end{Bmatrix} + \begin{bmatrix} C_{oo}^d & C_{oi}^d & 0 \\ C_{io}^d & C_{ii}^d + C_{ii}^h & C_{io}^h \\ 0 & C_{oi}^h & C_{oo}^h \end{bmatrix} \begin{Bmatrix} \dot{w}_o^d \\ \dot{w}_i^d \\ \dot{u}_o^h \end{Bmatrix}$$

$$+ \begin{bmatrix} K_{oo}^d & K_{oi}^d & 0 \\ K_{io}^d & K_{ii}^d + K_{ii}^h & K_{io}^h \\ 0 & K_{oi}^h & K_{oo}^h \end{bmatrix} \begin{Bmatrix} w_o^d \\ w_i^d \\ u_o^h \end{Bmatrix} = \begin{Bmatrix} F_o^d \\ F_i^d \\ F_o^h \end{Bmatrix}, \tag{2.29}$$

where the subscripts i and o represent the interfacial and other nodes; the superscripts d and h stand for the nodes on the disk and the hub, respectively.

(1) Disk   (2) Hub
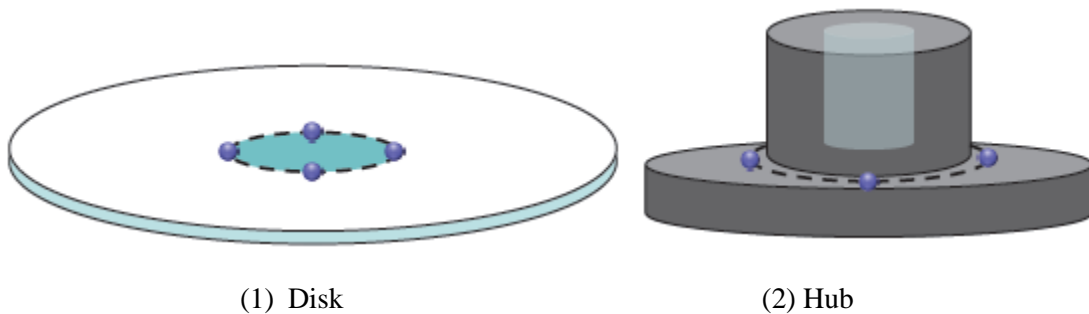
Figure 2.10 Rotating part I [38]

(1) Housing   (2) Pivot shaft

(3) Base plate
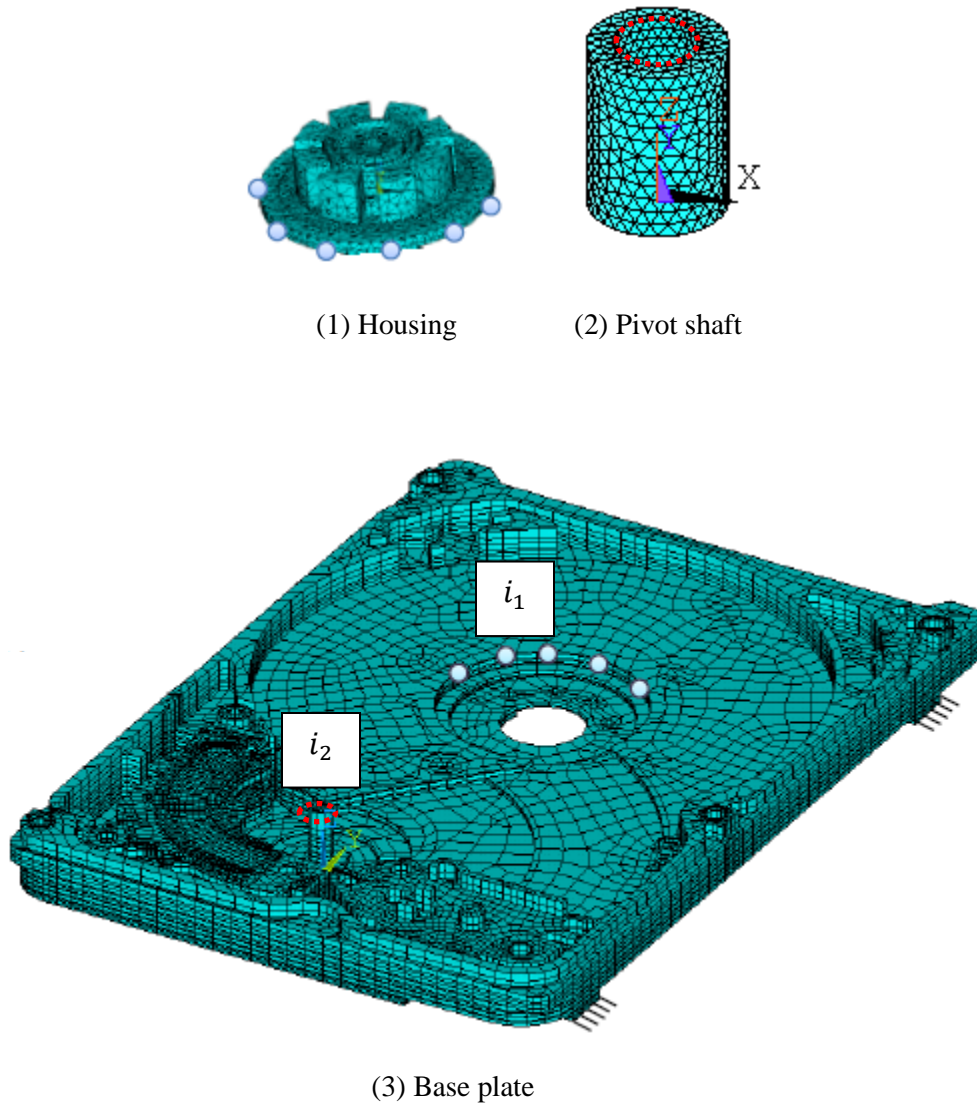
Figure 2.11 Stationary part

For stationary part, the compatibility conditions are

$$\{u_i^{hsng}\} = \{u_{i_1}^{base}\}, \tag{2.30}$$

and

$$\{u_{i_2}^{base}\} = \{u_i^{shft}\}, \tag{2.31}$$

where $\{u_i^{hsng}\}$ and $\{u_{i_1}^{base}\}$ are the displacements of the housing-base interfacial nodes and $\{u_{i_2}^{base}\}$ and $\{u_i^{shft}\}$ are the displacements of the base-shaft interfacial nodes (Figure 2.11).

Applying Eqn. (2.30) and (2.31), we can combine the dynamic equation of motion for the housing (Eqn. (2.15)), the base plate (Eqn. (2.19)) and the pivot shaft (Eqn. (2.20)):

$$
\begin{bmatrix}
M_{oo}^h & M_{oi}^h & 0 & 0 & 0 \\
M_{io}^h & M_{ii}^h + M_{i_1 i_1}^b & M_{i_1 o}^b & M_{i_1 i_2}^b & 0 \\
0 & M_{oi_1}^b & M_{oo}^b & M_{oi_2}^b & 0 \\
0 & M_{i_2 i_1}^b & M_{i_2 o}^b & M_{i_2 i_2}^b + M_{ii}^s & M_{io}^s \\
0 & 0 & 0 & M_{oi}^s & M_{oo}^s
\end{bmatrix}
\begin{Bmatrix}
\ddot{u}_o^h \\
\ddot{u}_{i_1}^b \\
\ddot{u}_o^b \\
\ddot{u}_{i_2}^b \\
\ddot{u}_o^s
\end{Bmatrix}
+
\begin{bmatrix}
C_{oo}^h & C_{oi}^h & 0 & 0 & 0 \\
C_{io}^h & C_{ii}^h + C_{i_1 i_1}^b & C_{i_1 o}^b & C_{i_1 i_2}^b & 0 \\
0 & C_{oi_1}^b & C_{oo}^b & C_{oi_2}^b & 0 \\
0 & C_{i_2 i_1}^b & C_{i_2 o}^b & C_{i_2 i_2}^b + C_{ii}^s & C_{io}^s \\
0 & 0 & 0 & C_{oi}^s & C_{oo}^s
\end{bmatrix}
\begin{Bmatrix}
\dot{u}_o^h \\
\dot{u}_{i_1}^b \\
\dot{u}_o^b \\
\dot{u}_{i_2}^b \\
\dot{u}_o^s
\end{Bmatrix}
$$

$$
+
\begin{bmatrix}
K_{oo}^h & K_{oi}^h & 0 & 0 & 0 \\
K_{io}^h & K_{ii}^h + K_{i_1 i_1}^b & K_{i_1 o}^b & K_{i_1 i_2}^b & 0 \\
0 & K_{oi_1}^b & K_{oo}^b & K_{oi_2}^b & 0 \\
0 & K_{i_2 i_1}^b & K_{i_2 o}^b & K_{i_2 i_2}^b + K_{ii}^s & K_{io}^s \\
0 & 0 & 0 & K_{oi}^s & K_{oo}^s
\end{bmatrix}
\begin{Bmatrix}
u_o^h \\
u_{i_1}^b \\
u_o^b \\
u_{i_2}^b \\
u_o^s
\end{Bmatrix}
=
\begin{Bmatrix}
F_o^h \\
F_{i_1}^b \\
F_o^b \\
F_{i_2}^b \\
F_o^s
\end{Bmatrix}
\tag{2.32}
$$

where the subscripts i_1 and i_2 represent the two sets of the base plate interfacial nodes. The superscripts h, b and s stand for the nodes on the housing, the base plate and the pivot shaft, respectively.
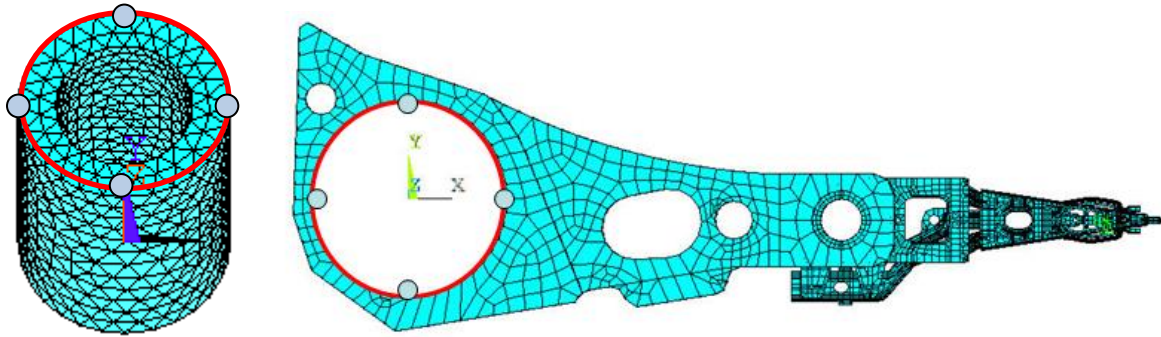
(1) Pivot sleeve   (2) HAA

Figure 2.12 Rotating part II

For rotating part II, the compatibility condition is

$$
\{u_i^{slev}\} = \{u_i^{HAA}\}, \tag{2.33}
$$

where $\{u_i^{slev}\}$ and $\{u_i^{HAA}\}$ are the displacements of the sleeve-HAA interfacial nodes (Figure 2.12). We can combine the dynamic equation of motion for the sleeve (Eqn. (2.21)) and the HAA (Eqn. (2.23)) using Eqn. (2.33):

$$\begin{bmatrix} M_{oo}^s & M_{oi}^s & 0 \\ M_{io}^s & M_{ii}^s + M_{ii}^h & M_{io}^h \\ 0 & M_{oi}^h & M_{oo}^h \end{bmatrix} \begin{Bmatrix} \ddot{u}_o^s \\ \ddot{u}_i^s \\ \ddot{u}_o^h \end{Bmatrix} + \begin{bmatrix} C_{oo}^s & C_{oi}^s & 0 \\ C_{io}^s & C_{ii}^s + C_{ii}^h & C_{io}^h \\ 0 & C_{oi}^h & C_{oo}^h \end{bmatrix} \begin{Bmatrix} \dot{u}_o^s \\ \dot{u}_i^s \\ \dot{u}_o^h \end{Bmatrix}$$

$$+ \begin{bmatrix} K_{oo}^s & K_{oi}^s & 0 \\ K_{io}^s & K_{ii}^s + K_{ii}^h & K_{io}^h \\ 0 & K_{oi}^h & K_{oo}^h \end{bmatrix} \begin{Bmatrix} u_o^s \\ u_i^s \\ u_o^h \end{Bmatrix} = \begin{Bmatrix} F_o^s \\ F_i^s \\ F_o^h \end{Bmatrix}, \tag{2.34}$$

where the superscripts s and h are used for the nodes on the sleeve and the HAA, respectively.

Considering the FDB effects between the rotating part I and the stationary part, and BB effects between stationary part and rotating part II, we can rewrite the three equations of motion (Eqn.(2.29), (2.32) and (2.34)) as following:

$$\begin{bmatrix} M_{oo}^{r_1} & M_{of}^{r_1} \\ M_{fo}^{r_1} & M_{ff}^{r_1} \end{bmatrix} \begin{Bmatrix} \ddot{u}_o^{r_1} \\ \ddot{u}_f^{r_1} \end{Bmatrix} + \begin{bmatrix} C_{oo}^{r_1} & C_{of}^{r_1} \\ C_{fo}^{r_1} & C_{ff}^{r_1} \end{bmatrix} \begin{Bmatrix} \dot{u}_o^{r_1} \\ \dot{u}_f^{r_1} \end{Bmatrix} + \begin{bmatrix} K_{oo}^{r_1} & K_{of}^{r_1} \\ K_{fo}^{r_1} & K_{ff}^{r_1} \end{bmatrix} \begin{Bmatrix} u_o^{r_1} \\ u_f^{r_1} \end{Bmatrix} = \begin{Bmatrix} 0 \\ f_f^{r_1} \end{Bmatrix} + \begin{Bmatrix} F_o^{r_1} \\ F_f^{r_1} \end{Bmatrix}, \tag{2.35}$$

$$\begin{bmatrix} M_{ff}^s & M_{fo}^s & 0 \\ M_{of}^s & M_{oo}^s & M_{ob}^s \\ 0 & M_{bo}^s & M_{bb}^s \end{bmatrix} \begin{Bmatrix} \ddot{u}_f^s \\ \ddot{u}_o^s \\ \ddot{u}_b^s \end{Bmatrix} + \begin{bmatrix} C_{ff}^s & C_{fo}^s & 0 \\ C_{of}^s & C_{oo}^s & C_{ob}^s \\ 0 & C_{bo}^s & C_{bb}^s \end{bmatrix} \begin{Bmatrix} \dot{u}_f^s \\ \dot{u}_o^s \\ \dot{u}_b^s \end{Bmatrix}$$

$$+ \begin{bmatrix} K_{ff}^s & K_{fo}^s & 0 \\ K_{of}^s & K_{oo}^s & K_{ob}^s \\ 0 & K_{bo}^s & K_{bb}^s \end{bmatrix} \begin{Bmatrix} u_f^s \\ u_o^s \\ u_b^s \end{Bmatrix} = \begin{Bmatrix} f_f^s \\ 0 \\ f_b^s \end{Bmatrix} + \begin{Bmatrix} F_f^s \\ F_o^s \\ F_b^s \end{Bmatrix}, \tag{2.36}$$

$$\begin{bmatrix} M_{bb}^{r_2} & M_{bo}^{r_2} \\ M_{ob}^{r_2} & M_{oo}^{r_2} \end{bmatrix} \begin{Bmatrix} \ddot{u}_b^{r_2} \\ \ddot{u}_o^{r_2} \end{Bmatrix} + \begin{bmatrix} C_{bb}^{r_2} & C_{bo}^{r_2} \\ C_{ob}^{r_2} & C_{oo}^{r_2} \end{bmatrix} \begin{Bmatrix} \dot{u}_b^{r_2} \\ \dot{u}_o^{r_2} \end{Bmatrix} + \begin{bmatrix} K_{bb}^{r_2} & K_{bo}^{r_2} \\ K_{ob}^{r_2} & K_{oo}^{r_2} \end{bmatrix} \begin{Bmatrix} u_b^{r_2} \\ u_o^{r_2} \end{Bmatrix} = \begin{Bmatrix} f_b^{r_2} \\ 0 \end{Bmatrix} + \begin{Bmatrix} F_b^{r_2} \\ F_o^{r_2} \end{Bmatrix}, \tag{2.37}$$

where the superscripts r_1, s and r_2 indicate the nodes of the rotating part I, stationary part and rotating part II, respectively. The subscripts f and b are used for the nodes at the FDB and BB locations, respectively. F represents the system's external force (disturbances, shocks etc.) and f represents the reaction force due to the deformation of the two bearings.

As the disk spins when the HDD is working and the HAA rotates during the seeking process, there might be a relative motion between the two surfaces which produce the bearing force (FDB or BB). Since the number of model nodes is finite in the FEM, the pair of nodes representing one spring-dashpot system keeps changing or even worse, a node on one surface often gets intercepted between two nodes on the other surface as shown in Figure 2.13 for the BB nodes. The detailed analysis of the FDB nodes between the hub and the housing can be found in [38]. For condition shown in Figure 2.13, the reaction force at one equivalent spring system can be obtained by modifying Eqn. (2. 22):

$$f^s = -f^{r_2} = -K_{BB}(u^s - \tilde{u}^r) - C_{BB}(\dot{u}^s - \dot{\tilde{u}}^r), \tag{2.38}$$

where $\{\tilde{u}^r\}$ is the projected displacement of pivot sleeve nodes coinciding with the pivot shaft nodes containing the BB springs.
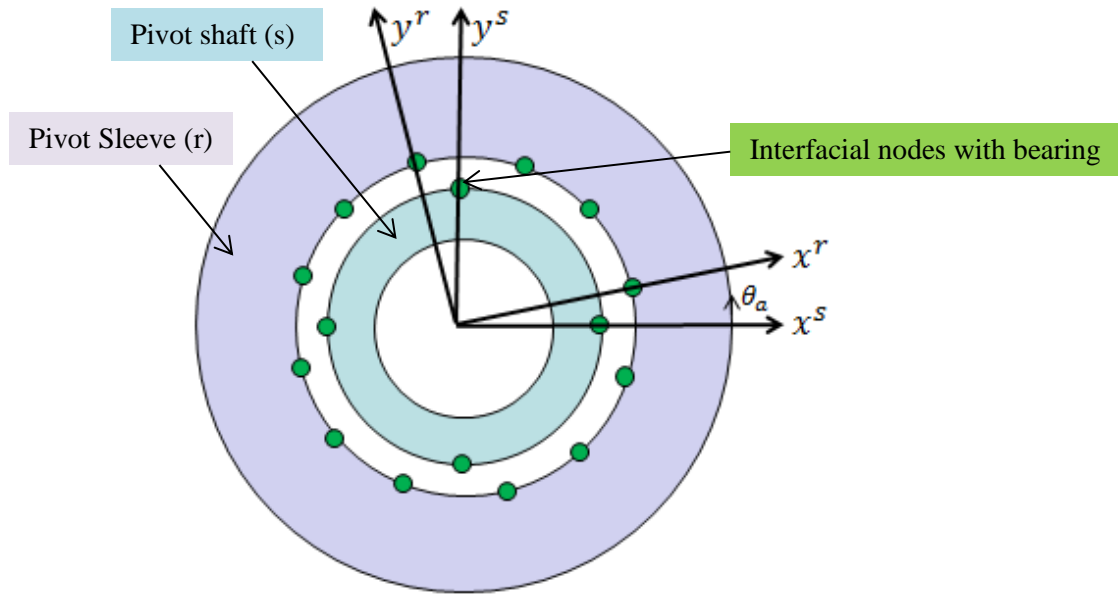
Figure 2.13 Rotating sleeve nodes intercepted between shaft nodes
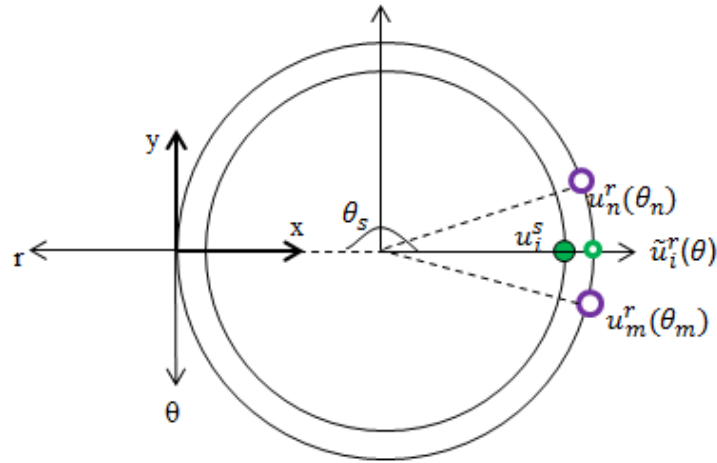
Figure 2.14 Interpolation formula to get the reaction force at BB

The projected displacement on the sleeve node can be calculated by interpolating the two adjacent nodes' displacements as shown in Figure 2.14 and can be written as:

$$\tilde{u}_i^r(\theta) = c_1 \cdot u_m^r(\theta_m) + c_2 \cdot u_n^r(\theta_n), \tag{2.39}$$

where $\{\tilde{u}_i^r\}$, $\{u_m^r\}$ and $\{u_n^r\}$ are the displacements of the projected nodes and its two adjacent nodes, respectively. θ, θ_m and θ_n are the angular coordinates of the three nodes. And

$$c_1 = \frac{\theta_n - \theta}{\theta_n - \theta_m}, \tag{2.40}$$

$$c_2 = \frac{\theta - \theta_m}{\theta_n - \theta_m}. \tag{2.41}$$

The displacement evaluated in Eqn. (2.39) is calculated in the sleeve orthogonal coordinate system. It is required to transform it to the shaft frame. So the projected sleeve nodes' displacement in the shaft frame ($\{\tilde{u}^r\}$) is:

$$\begin{Bmatrix} \tilde{u}_x^r \\ \tilde{u}_y^r \\ \tilde{u}_z^r \end{Bmatrix} = \begin{bmatrix} cos\theta & -sin\theta & 0 \\ sin\theta & cos\theta & 0 \\ 0 & 0 & 1 \end{bmatrix} \begin{Bmatrix} u_x^r \\ u_y^r \\ u_z^r \end{Bmatrix}. \tag{2.42}$$

As the BB damping and stiffness coefficients have two components, which are in the axial and radial directions, all the displacements $\{u_x, u_y, u_z\}^T$ at the BB locations should be transformed to the cylindrical coordinate system and can be calculated as:

$$\begin{Bmatrix} u_r \\ u_a \end{Bmatrix} = \begin{bmatrix} cos\theta_s & sin\theta_s & 0 \\ 0 & 0 & 1 \end{bmatrix} \begin{Bmatrix} u_x \\ u_y \\ u_z \end{Bmatrix}, \tag{2.43}$$

where u_r and u_a are the displacements of the nodes on the sleeve and the shaft at BB locations in the cylindrical coordinate system. θ_s is the angle of x-axis and the radial direction of the nodes representing BB on the sleeve. For example, in Figure 2.13, $\theta_s = 0, \pi/2, \pi, 3\pi/2$.

Once the BB reaction forces $\{f_r, f_a\}^T$ have been obtained on the sleeve and the shaft by Eqn. (2.38), they should be first transformed back to the shaft orthogonal coordinate system:

$$\begin{Bmatrix} f_x \\ f_y \\ f_z \end{Bmatrix} = \begin{bmatrix} cos\theta_s & 0 \\ sin\theta_s & 0 \\ 0 & 1 \end{bmatrix} \begin{Bmatrix} f_r \\ f_a \end{Bmatrix}. \tag{2.44}$$

The projected reaction forces $\{\tilde{f}_x^r, \tilde{f}_y^r, \tilde{f}_z^r\}^T$ on the sleeve are required to transform to the sleeve frame after solving Eqn. (2.44):

$$\begin{Bmatrix} f_x^r \\ f_y^r \\ f_z^r \end{Bmatrix} = \begin{bmatrix} cos\theta & sin\theta & 0 \\ -sin\theta & cos\theta & 0 \\ 0 & 0 & 1 \end{bmatrix} \begin{Bmatrix} \tilde{f}_x^r \\ \tilde{f}_y^r \\ \tilde{f}_z^r \end{Bmatrix}. \tag{2.45}$$

The reaction force at the BB nodes of the sleeve can be redistributed as:

$$\boldsymbol{f}_m^r(\theta_m) = c_1 \cdot \boldsymbol{f}_i^r(\theta), \tag{2.46}$$

$$\boldsymbol{f}_n^r(\theta_n) = c_2 \cdot \boldsymbol{f}_i^r(\theta), \tag{2.47}$$

where $\{\boldsymbol{f}_i^r\}$, $\{\boldsymbol{f}_m^r\}$ and $\{\boldsymbol{f}_n^r\}$ are the reaction forces of the projected nodes and its two adjacent nodes, respectively, shown in Figure 2.14.

Substituting the reaction force arising due to the deformation of FDB and BB into Eqn. (2.35)-(2.37), we can get the equation of motion for the whole assembly system:

$$
\begin{bmatrix}
M_{oo}^{r_1} & M_{of}^{r_1} & 0 & 0 & 0 & 0 & 0 \\
M_{fo}^{r_1} & M_{ff}^{r_1} & 0 & 0 & 0 & 0 & 0 \\
0 & 0 & M_{ff}^{s} & M_{fo}^{s} & 0 & 0 & 0 \\
0 & 0 & M_{of}^{s} & M_{oo}^{s} & M_{ob}^{s} & 0 & 0 \\
0 & 0 & 0 & M_{bo}^{s} & M_{bb}^{s} & 0 & 0 \\
0 & 0 & 0 & 0 & 0 & M_{bb}^{r_2} & M_{bo}^{r_2} \\
0 & 0 & 0 & 0 & 0 & M_{ob}^{r_2} & M_{oo}^{r_2}
\end{bmatrix}
\begin{Bmatrix}
\ddot{u}_o^{r_1} \\
\ddot{u}_f^{r_1} \\
\ddot{u}_f^{s} \\
\ddot{u}_o^{s} \\
\ddot{u}_b^{s} \\
\ddot{u}_b^{r_2} \\
\ddot{u}_o^{r_2}
\end{Bmatrix}
$$

$$
+
\begin{bmatrix}
C_{oo}^{r_1} & C_{of}^{r_1} & 0 & 0 & 0 & 0 & 0 \\
C_{fo}^{r_1} & C_{ff}^{r_1}+C_{f}^{rr}(t) & C_{f}^{rs}(t) & 0 & 0 & 0 & 0 \\
0 & C_{f}^{sr}(t) & C_{ff}^{s}+C_{f}^{ss}(t) & C_{fo}^{s} & 0 & 0 & 0 \\
0 & 0 & C_{of}^{s} & C_{oo}^{s} & C_{ob}^{s} & 0 & 0 \\
0 & 0 & 0 & C_{bo}^{s} & C_{bb}^{s}+C_{b}^{ss}(t) & C_{b}^{sr}(t) & 0 \\
0 & 0 & 0 & 0 & C_{b}^{rs}(t) & C_{bb}^{r_2}+C_{b}^{rr}(t) & C_{bo}^{r_2} \\
0 & 0 & 0 & 0 & 0 & C_{ob}^{r_2} & C_{oo}^{r_2}
\end{bmatrix}
\begin{Bmatrix}
\dot{u}_o^{r_1} \\
\dot{u}_f^{r_1} \\
\dot{u}_f^{s} \\
\dot{u}_o^{s} \\
\dot{u}_b^{s} \\
\dot{u}_b^{r_2} \\
\dot{u}_o^{r_2}
\end{Bmatrix}
$$

$$
+
\begin{bmatrix}
K_{oo}^{r_1} & K_{of}^{r_1} & 0 & 0 & 0 & 0 & 0 \\
K_{fo}^{r_1} & K_{ff}^{r_1}+K_{f}^{rr}(t) & K_{f}^{rs}(t) & 0 & 0 & 0 & 0 \\
0 & K_{f}^{sr}(t) & K_{ff}^{s}+K_{f}^{ss}(t) & K_{fo}^{s} & 0 & 0 & 0 \\
0 & 0 & K_{of}^{s} & K_{oo}^{s} & K_{ob}^{s} & 0 & 0 \\
0 & 0 & 0 & K_{bo}^{s} & K_{bb}^{s}+K_{b}^{ss}(t) & K_{b}^{sr}(t) & 0 \\
0 & 0 & 0 & 0 & K_{b}^{rs}(t) & K_{bb}^{r_2}+K_{b}^{rr}(t) & K_{bo}^{r_2} \\
0 & 0 & 0 & 0 & 0 & K_{ob}^{r_2} & K_{oo}^{r_2}
\end{bmatrix}
\begin{Bmatrix}
u_o^{r_1} \\
u_f^{r_1} \\
u_f^{s} \\
u_o^{s} \\
u_b^{s} \\
u_b^{r_2} \\
u_o^{r_2}
\end{Bmatrix}
=
\begin{Bmatrix}
F_o^{r_1} \\
F_f^{r_1} \\
F_f^{s} \\
F_o^{s} \\
F_b^{s} \\
F_b^{r_2} \\
F_o^{r_2}
\end{Bmatrix}
$$

…… (2.48)

where $C_f^{\alpha\beta}(t)$ and $K_f^{\alpha\beta}(t)$ (α, β= r, s which represent rotating and stationary units) are the damping and stiffness coefficients for the FDB. They are time dependent because of the structural rotating characteristics. $C_b^{\alpha\beta}(t)$ and $K_b^{\alpha\beta}(t)$ (α, β= r, s) are the time dependent damping and stiffness coefficients for the BB.

2.4 Numerical Techniques

2.4.1 Transient Solution

We can rewrite the equation of motion for the assembly system (Eqn. (2.48)) and disk BC (Eqn. (2.57) as:

$$\begin{cases} [M]\{\ddot{u}\} + [C]\{\dot{u}\} + [K]\{u\} + [Q]^T\{\lambda\} = \{F\} \\ \qquad\qquad [Q]\{u\} = \{u_i\} \end{cases}, \tag{2.49}$$

where $\{\lambda\}$ is the reaction force arising due to the disk inner radius BC. $[Q]$ is the constraint matrix.

The Newmark-beta method [52] is applied to solve this equation numerically as it is widely used in finite element analysis to model dynamic systems. Discretizing the time into uniform time steps of Δt, the equation of motion at the time $t = t_{n+1} = (n+1)\Delta t$ is as following:

$$\begin{cases} [M]\{\ddot{u}\}_{n+1} + [C]_{n+1}\{\dot{u}\}_{n+1} + [K]_{n+1}\{u\}_{n+1} + [Q]^T_{n+1}\{\lambda\}_{n+1} = \{F\}_{n+1} \\ \qquad\qquad [Q]_{n+1}\{u\}_{n+1} = \{u_i\}_{n+1} = \{0\} \end{cases}. \tag{2.50}$$

In the Nwemark-beta approach, the displacement and velocity at time t_{n+1} can be expressed as:

$$\{u\}_{n+1} = \{\breve{u}\}_{n+1} + \beta\Delta t^2\{\ddot{u}\}_{n+1}, \tag{2.51a}$$

$$\{\dot{u}\}_{n+1} = \{\breve{\dot{u}}\}_{n+1} + \gamma\Delta t\{\ddot{u}\}_{n+1}. \tag{2.51b}$$

$\{\breve{u}\}_{n+1}$ and $\{\breve{\dot{u}}\}_{n+1}$ are calculated based on the information at time t_n:

$$\{\breve{u}\}_{n+1} = \{u\}_n + \Delta t\{\dot{u}\}_n + (1-2\beta)\frac{\Delta t^2}{2}\{\ddot{u}\}_n, \tag{2.52a}$$

$$\{\breve{\dot{u}}\}_{n+1} = \{\dot{u}\}_n + (1-\gamma)\Delta t\{\ddot{u}\}_n, \tag{2.52b}$$

where β and γ are chosen such that

$$0 \le \beta \le {}^1/_2, 0 < \gamma \le 1. \tag{2.53}$$

Substituting Eqn. (2.51a)-(2.52b) to the Eqn. (2.50), we can finally get the equation of motion:

$$\begin{bmatrix} [A]_{n+1} & [Q]^T_{n+1} \\ [Q]_{n+1} & [0] \end{bmatrix}\begin{Bmatrix} \{\ddot{u}\}_{n+1} \\ \{\lambda\}_{n+1} \end{Bmatrix} = \begin{Bmatrix} \{X\}_{n+1} \\ \{Y\}_{n+1} \end{Bmatrix}, \tag{2.54}$$

where

$$[A]_{n+1} = [M] + \gamma\Delta t[C]_{n+1} + \beta\Delta t^2[K]_{n+1}, \tag{2.55a}$$

$$\{X\}_{n+1} = \{F\}_{n+1} - [C]_{n+1}\{\breve{\dot{u}}\}_{n+1} - [K]_{n+1}\{\breve{u}\}_{n+1}, \tag{2.55b}$$

$$\{Y\}_{n+1} = \left(\frac{1}{\beta\Delta t^2}\right)(\{u_i\} - [Q]_{n+1}\{\breve{u}\}_{n+1}). \tag{2.55c}$$

By solving Eqn. (2.54), the system's acceleration $\{\ddot{u}\}_{n+1}$ can be obtained at time t_{n+1}. The displacement and velocity at the new time step can be determined by Eqn. (2.51a) and (2.51b).

Assembling various components in the multi-body model makes it very time consuming to finish one simulation. As the reaction force arising due to the disk inner radius BC is not quite

interesting to us, we use an elimination method to remove the reaction force term and disk boundary constraint term. So the final form of the equation of motion (comparing with Eqn. (2.54)) after applying Newmark-beta scheme is:

$$[A']_{n+1}\{\ddot{u}'\}_{n+1} = \{X'\}_{n+1},$$
(2.56)

2.4.2 Block Factorization

The coefficient matrix $[A]$ in Eqn.(2.56) changes at every time step. Applying a direct scheme, like Gauss Elimination, to solve Eqn. (2.56) is still very computationally expensive even though we have reduced the matrix size by the elimination method introduced in the section 2.4.1. From Eqn. (2.48) the time varying terms in $[A]$ are all caused by the FDB and BB contributions, which means that the other terms do not need to be updated at each time step. A block factorization method is proposed for the LU decomposition for the matrix $[A]$ in order to achieve this goal.

First, the block form of matrix $[A]$ according to Eqn. (2.48) and (2.55a) can be written as:

$$\begin{bmatrix} A_{11} & A_{12} & 0 & 0 & 0 \\ A_{21} & A_{22}(t) & A_{23} & 0 & 0 \\ 0 & A_{32} & A_{33} & A_{34} & 0 \\ 0 & 0 & A_{43} & A_{44}(t) & A_{45} \\ 0 & 0 & 0 & A_{54} & A_{55} \end{bmatrix} = \begin{bmatrix} M_{11} & M_{12} & 0 & 0 & 0 \\ M_{21} & M_{22} & M_{23} & 0 & 0 \\ 0 & M_{32} & M_{33} & M_{34} & 0 \\ 0 & 0 & M_{43} & M_{44} & M_{45} \\ 0 & 0 & 0 & M_{54} & M_{55} \end{bmatrix} +$$

$$\gamma \Delta t \begin{bmatrix} C_{11} & C_{12} & 0 & 0 & 0 \\ C_{21} & C_{22}(t) & C_{23} & 0 & 0 \\ 0 & C_{32} & C_{33} & C_{34} & 0 \\ 0 & 0 & C_{43} & C_{44}(t) & C_{45} \\ 0 & 0 & 0 & C_{54} & C_{55} \end{bmatrix} + \beta \Delta t^2 \begin{bmatrix} K_{11} & K_{12} & 0 & 0 & 0 \\ K_{21} & K_{22}(t) & K_{23} & 0 & 0 \\ 0 & K_{32} & K_{33} & K_{34} & 0 \\ 0 & 0 & K_{43} & K_{44}(t) & K_{45} \\ 0 & 0 & 0 & K_{54} & K_{55} \end{bmatrix}.$$
(2.57)

The LU decomposition for the matrix $[A]$ is:

$$\begin{bmatrix} A_{11} & A_{12} & 0 & 0 & 0 \\ A_{21} & A_{22}(t) & A_{23} & 0 & 0 \\ 0 & A_{32} & A_{33} & A_{34} & 0 \\ 0 & 0 & A_{43} & A_{44}(t) & A_{45} \\ 0 & 0 & 0 & A_{54} & A_{55} \end{bmatrix} = \begin{bmatrix} L_{11} & 0 & 0 & 0 & 0 \\ L_{21} & L_{22} & 0 & 0 & 0 \\ 0 & L_{32} & L_{33} & 0 & 0 \\ 0 & 0 & L_{43} & L_{44} & 0 \\ 0 & 0 & 0 & L_{54} & L_{55} \end{bmatrix} \begin{bmatrix} U_{11} & U_{12} & 0 & 0 & 0 \\ 0 & U_{22} & U_{23} & 0 & 0 \\ 0 & 0 & U_{33} & U_{34} & 0 \\ 0 & 0 & 0 & U_{44} & U_{45} \\ 0 & 0 & 0 & 0 & U_{55} \end{bmatrix}.$$
(2.58)

Expanding Eqn. (2.58) in component form, we find that the following matrices need to be calculated only once:

$$L_{11}U_{11} = A_{11} \qquad\qquad \rightarrow L_{11}, U_{11}$$

$$L_{11}U_{12} = A_{12} \qquad\qquad \rightarrow U_{12}$$

$$L_{21}U_{11} = A_{21} \qquad\qquad \rightarrow L_{21}$$

However, the rest of the L and U matrices are solved at every time step:

$$L_{22}U_{22} = A_{22} - L_{21}U_{12} \qquad \rightarrow L_{22}, U_{22}$$

$$L_{22}U_{23} = A_{23} \qquad \rightarrow U_{23}$$

$$L_{32}U_{22} = A_{32} \qquad \rightarrow L_{32}$$

$$L_{33}U_{33} = A_{33} - L_{32}U_{23} \qquad \rightarrow L_{33}, U_{33}$$

$$L_{33}U_{34} = A_{34} \qquad \rightarrow U_{34}$$

$$L_{43}U_{33} = A_{43} \qquad \rightarrow L_{43}$$

$$L_{44}U_{44} = A_{44} - L_{43}U_{34} \qquad \rightarrow L_{44}U_{44}$$

$$L_{44}U_{45} = A_{45} \qquad \rightarrow U_{45}$$

$$L_{54}U_{44} = A_{54} \qquad \rightarrow L_{54}$$

$$L_{55}U_{55} = A_{55} - L_{54}U_{45} \qquad \rightarrow L_{55}, U_{55}$$

Figure 2.15 shows the sizes of the block matrices defined in Eqn. (2.57) for the full multi-body op-shock model. It can be observed that the sizes of the LU matrices, that need to be computed at every time step, are much smaller than the size of the matrix, which is decomposed only once. Hence the block factorization method can save a lot of computation time.

$$\begin{bmatrix} A_{11} & A_{12} & 0 & 0 & 0 \\ A_{21} & A_{22}(t) & A_{23} & 0 & 0 \\ 0 & A_{32} & A_{33} & A_{34} & 0 \\ 0 & 0 & A_{43} & A_{44}(t) & A_{45} \\ 0 & 0 & 0 & A_{54} & A_{55} \end{bmatrix} \begin{array}{l} m \approx 1750 \\ n \approx 150 \\ p \approx 600 \\ o \approx 100 \\ q \approx 300 \end{array}$$

Figure 2.15 Size of block matrices generated in a full multi-body op-shock model

2.5 Simulation Algorithm

The flowchart of the multi-body op-shock simulation is shown in Figure 2.16. After the simulation starts, the FE matrices for the spinning disk are computed and then coupled with the imported reduced matrices for the other components to develop the FE formula for the whole assembly system. Then an air bearing simulation starts with an initial guess for the slider's flying attitude, including the nominal flying height, pitch and roll. The structural displacement at that time step t_n is computed, including the disk deformation and the slider center's displacement. Then the minimum clearance between the slider and disk can be determined. If the minimum clearance is less than the glide height, then the time step (Δt) is reduced to one tenth in order to capture the slider's dynamics. The air bearing problem is solved to get the pressure profile under the slider surface, which is further integrated over the slider surface to get the bearing force and moments. Other interfacial forces, such as the contact force, intermolecular force and electrostatic force, are also included to obtain the net force acting on the slider. Next we solve the structural dynamic equation again to get a new slider center's displacement x_n^t. If the difference between the new displacement x_n^t and the old displacement x_o^t is larger than a pre-defined threshold, the slider's displacement is updated with the new one. The fixed point

iteration is carried out until the two displacements' difference is small enough. Once the convergence is obtained, the whole structural system is advanced to its new location. If the current time is smaller than the designated simulation time, the program goes back to the structural displacement solving step and starts a new iteration.
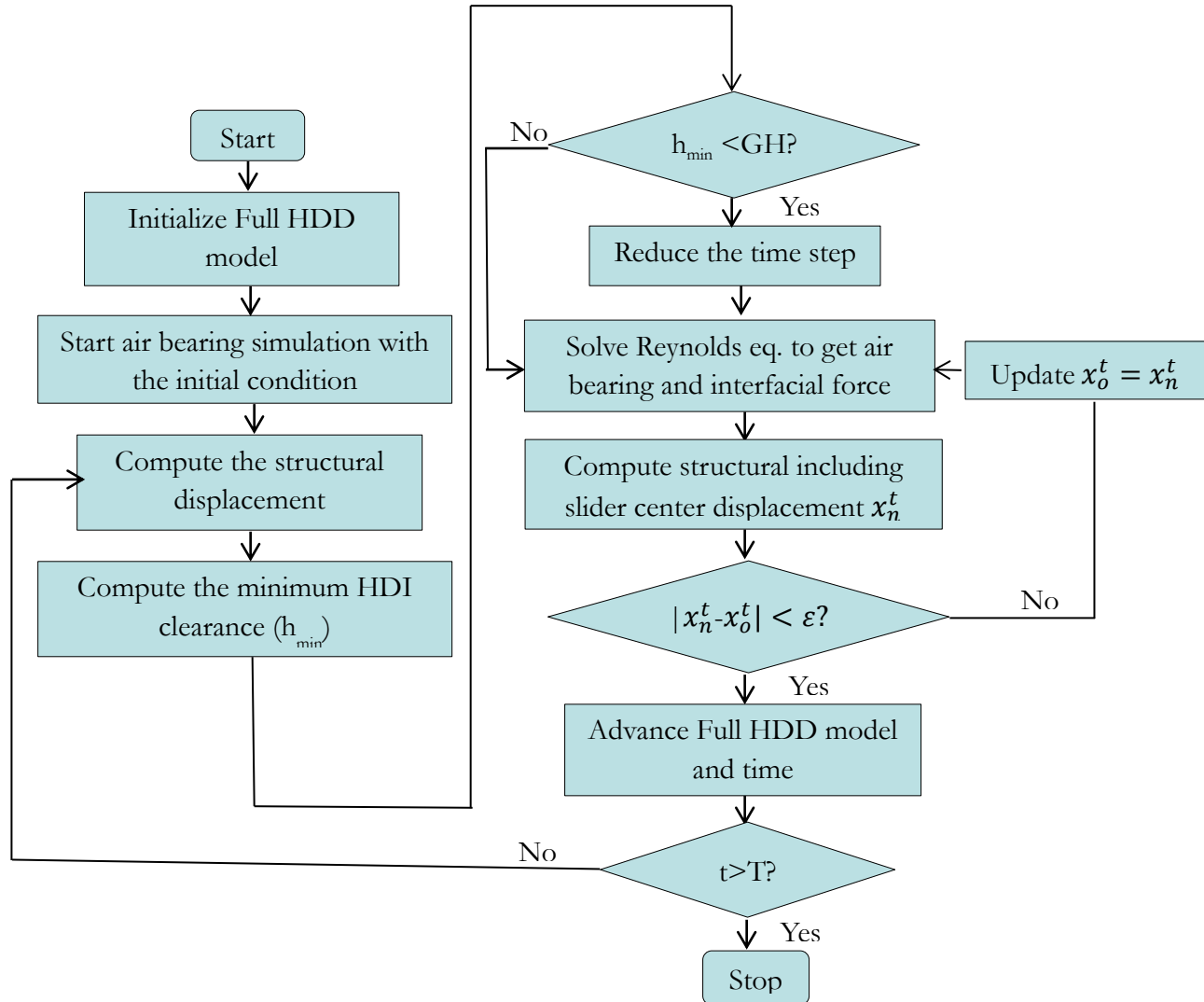
Figure 2.16 A flowchart of the multi-body op-shock simulator

2.6 Conclusion

In this chapter, we introduced the method to model each component we considered in the HDD. The process of assembling the individual components to get the complete system response during a dynamic event is explained. Finally a simulation algorithm flowchart is given to show the multi-body op-shock simulation procedure.

Chapter 3 Operational Shock Simulation in Hard Disk Drives

3.1 Introduction

There have been many experimental and numerical studies [16-29] to investigate the shock response of the mechanical and air bearing systems. However, they are either limited to component level or not considering slider-disk contacts. In this chapter, we use the structural-fluid (multi-body op-shock) model developed in Chapter 2 to study the effects of certain components on the HDI response and the failure mechanisms for different sliders.

3.2 Structural-Fluid Model and Operational Shock model

In the structural-fluid model we use the following equation of motion to calculate the system's structural response:

$$[M]\{\ddot{u}\} + [C]\{\dot{u}\} + [K]\{u\} = \{F\}, \tag{3.1}$$

in which $[M]$, $[C]$ and $[K]$ are the mass, damping and stiffness matrices of the structure, $\{u\}$ is the displacement vector and $\{F\}$ is the external load vector. The air flow between the slider and the disk is governed by the generalized Reynolds equation:

$$\frac{\partial}{\partial X}\left(Q(K_n)PH^3\frac{\partial P}{\partial X} - \Lambda_x PH\right) + \frac{\partial}{\partial Y}\left(Q(K_n)PH^3\frac{\partial P}{\partial Y} - \Lambda_Y PH\right) = \sigma\frac{\partial(PH)}{\partial T}. \tag{3.2}$$

The meaning of each term is explained in Chapter 2. Equation (3.1) and (3.2) are solved together to get the structural and HDI response in order to investigate the HDD working performance during an op-shock event.

A shock is modeled as a half sine acceleration wave which is defined by its amplitude and its pulse width. The pulse width determines the excitation frequency by the following relation:

$$f = \frac{1}{2T_{pw}}. \tag{3.3}$$

One shock model is shown in Figure 3.1, in which the amplitude is 400G (G is the gravity acceleration) and the pulse width is 2ms. A positive shock is defined as one that causes the disk to move towards the slider, while in a negative shock, the disk is followed by the slider.

3.3 Components' Effects on the Head Disk Interface Response

This investigation is conducted on a commercial 2.5-inch mobile drive with a femto slider (0.85 mm × 0.7 mm× 0.23 mm) which has the ABS design shown in Figure 3.2.
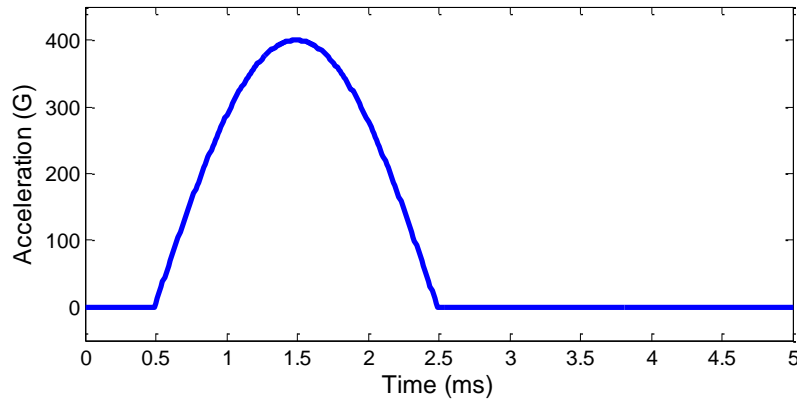
Figure 3.1 Op-shock model
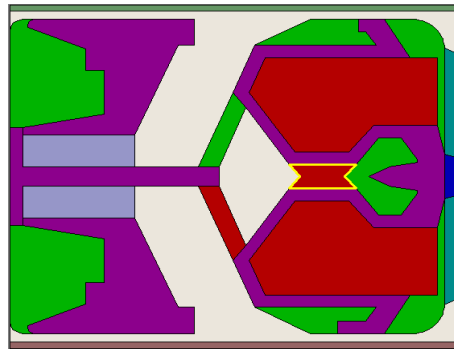
Figure 3.2 ABS design of the first slider we used in op-shock investigation

3.3.1 Structure components effects

In order to study the components' effects on the HDI, we analyze four structure models in this section. Model I which is called the "disk model" consists of a disk (with fixed inner radius) and a HAA (fixed at the pivot); Model II, "the disk support model", consists of a disk, a disk support system (spindle motor and base plate) and a HAA (fixed at pivot); Model III, "the actuator model", includes a disk (with fixed inner radius), a HAA, a pivot and a base plate; Model IV, "the full model" contains a disk, a spindle motor, a base plate, a pivot and a HAA. The shock model used in this section is a positive shock with shock amplitude of 400G and pulse width of 2.0 ms.

Figure 3.3 shows plots of the disk displacements at the slider's center position for the four models. The disk displacements are the same for Case I and Case III, which correspond to Model I and Model III, respectively. It is easy to understand because the disk's BCs are the same for these two models. The disk displacements are also the same for Case II and Case IV (corresponding to Model II and Model IV) because the disk is mounted on the disk support system in both models.

The relative displacements between the slider and the disk are shown in Figure 3.4. It is found that the slider's displacements are quite different even when the disk displacements are the same, such as in Case I and Case III. A suspension is designed to be more flexible than a disk.
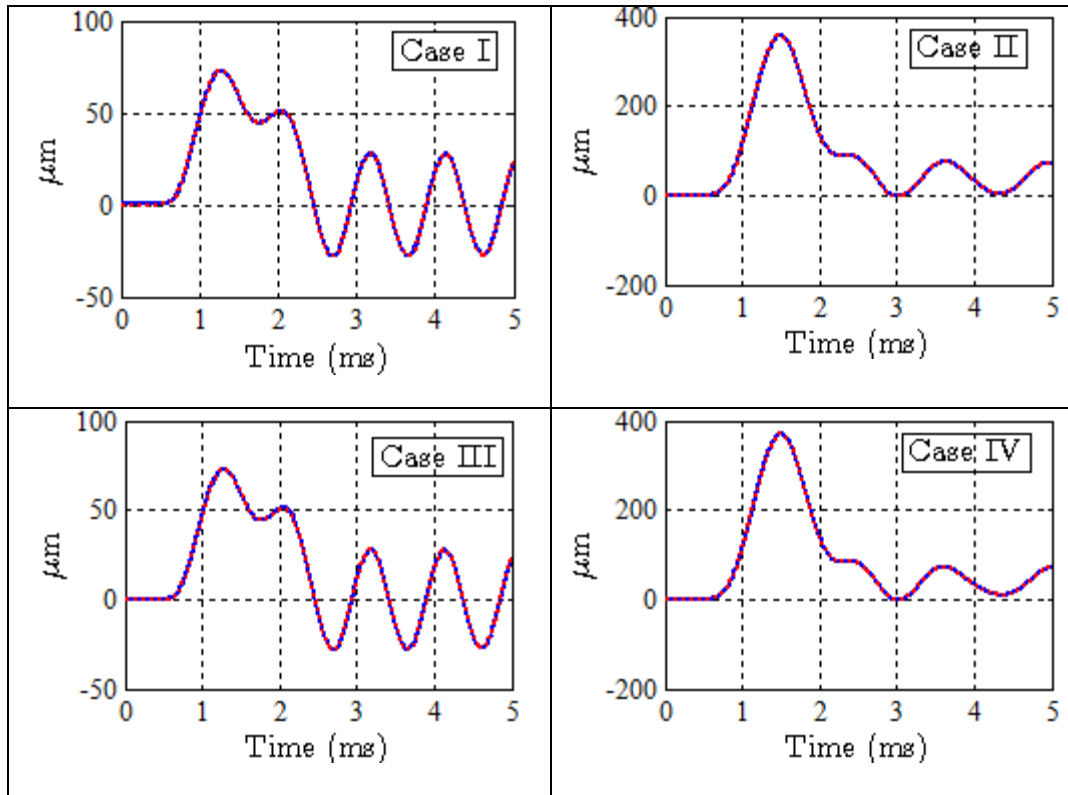
Figure 3.3 Disk displacements for the four cases
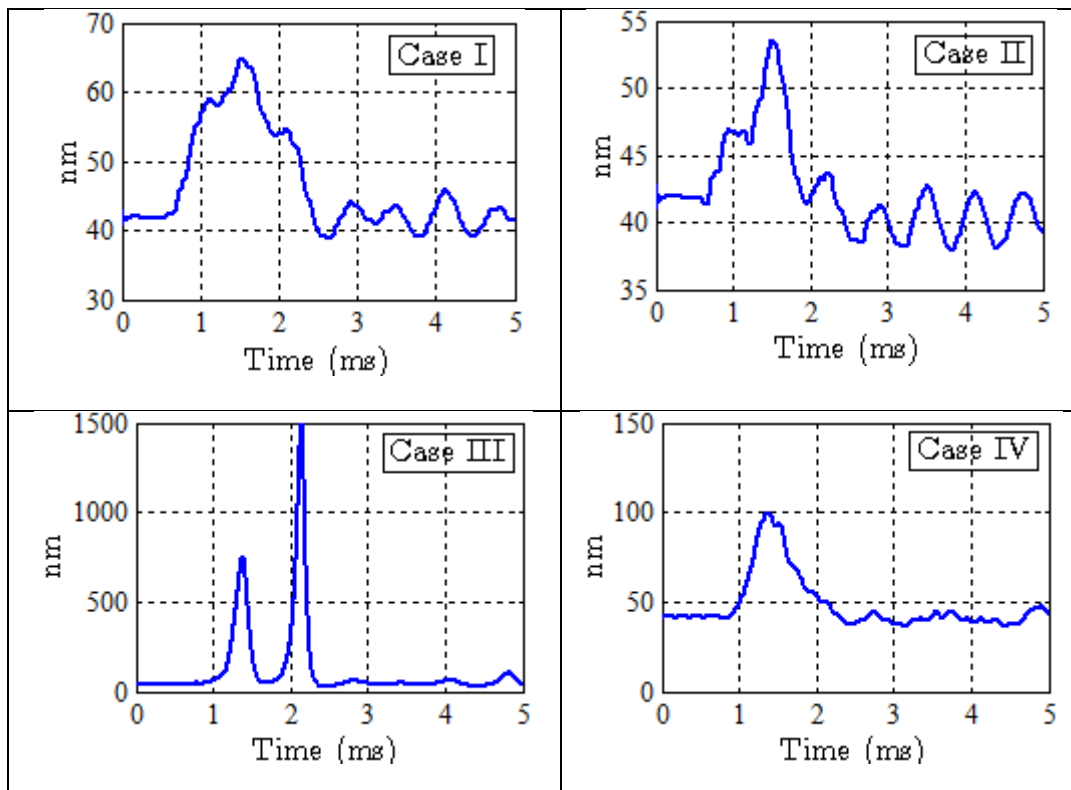
Figure 3.4 Relative displacements for the four cases

When a HDD is experiencing a positive shock, the suspension has a larger displacement than the disk due to the flexibility difference. Thus, the relative displacement increases during a positive shock. Compared with the fixed actuator in Model I, the actuator is connected to the base plate in Model III, which increases the flexibility of the actuator assembly. Thus, the flexibility difference between the HAA and the disk increases. That is why the relative displacement in Case III is larger than that in Case I. Similar analysis to the other two cases, the relative displacement is larger in Case IV than in Case II. Comparing Model II with Model I, the disk is mounted on the disk support system in Model II, which increases the flexibility of the disk system and decreases the flexibility difference between the HAA and the disk system. That is why a smaller relative displacement is detected in Case II than in Case I. From the above analysis, it is found that the flexibility difference is largest in Model III and smallest in Model II.
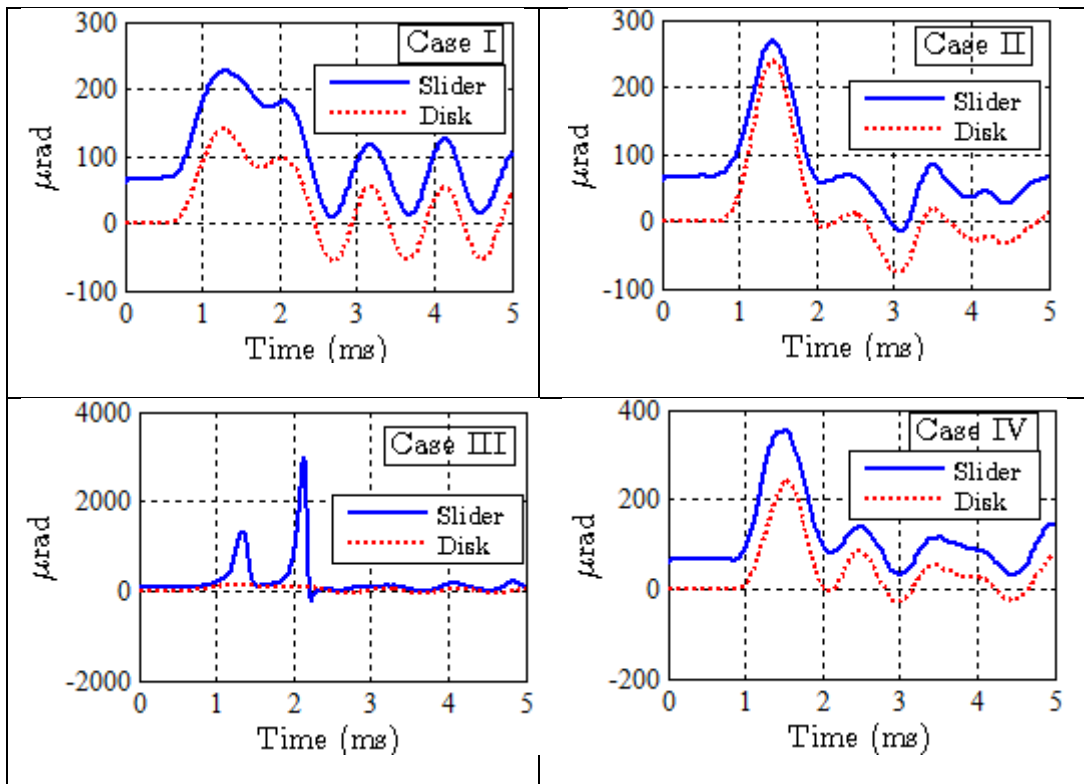
Figure 3.5 Absolute pitches for the four cases

The different responses of the slider can also be easily seen from Figure 3.5 and Figure 3.6 which give the slider's absolute and relative pitches. The pitches of the disk and the slider increase during the shock period for all the cases. In Case III, the flexibility difference between the HAA and the disk is largest, so the relative pitch changes most. It is also found that the slider's absolute pitch (Figure 3.5) changes very severely in this case, which is likely to be caused by the resonance vibration of the suspension. The big change of the pitch in Case III also causes the two peaks in the relative displacement (Figure 3.4). In Case II, however, the flexibility difference between the HAA and the disk is smallest, so a minimum relative pitch is found in this case during the shock period. Moreover, the relative pitch in this case starts to decrease after a slight increase and arrives at its local minimum at around 1.5 ms.
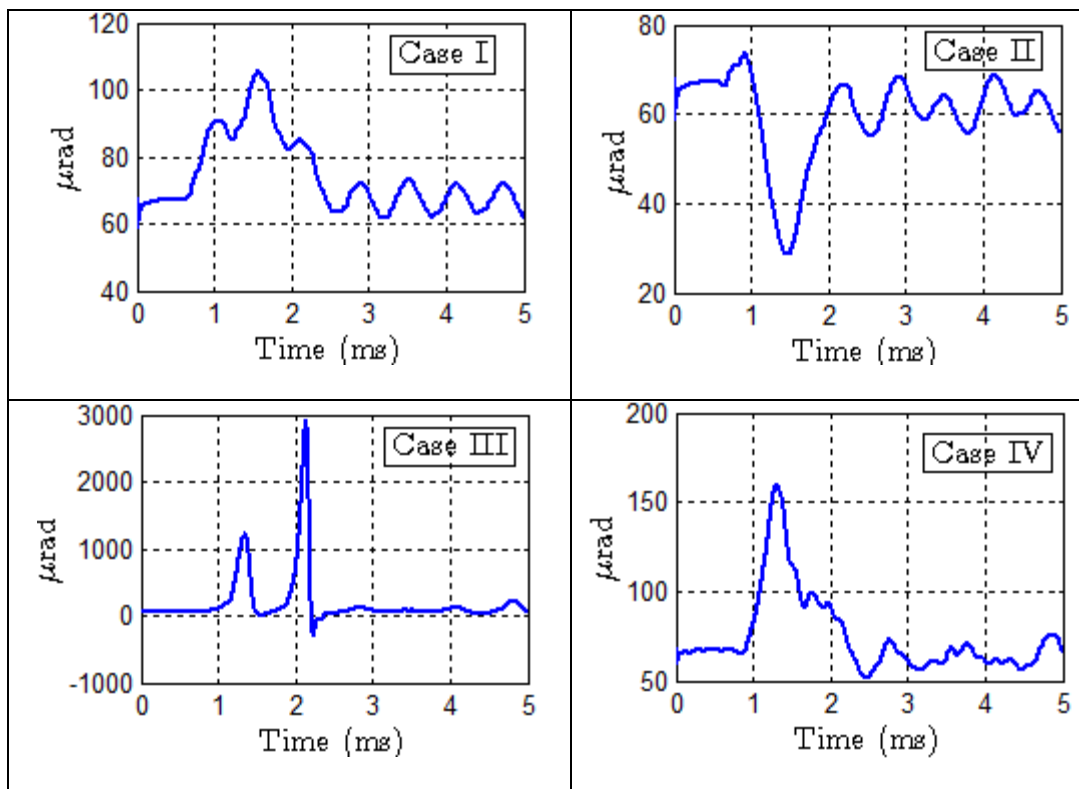
Figure 3.6 Relative pitches for the four cases
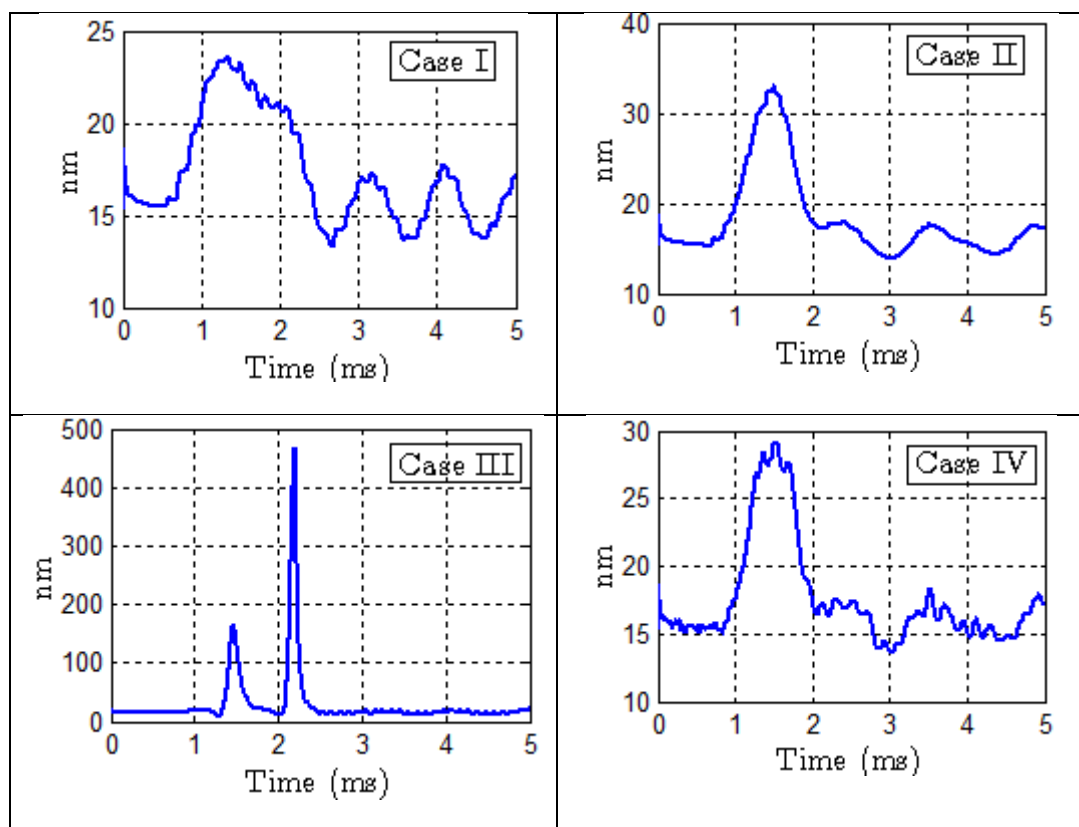
Figure 3.7 Minimum clearances for the four cases

Figure 3.7 shows the minimum clearances between the slider and the disk for the four cases. It is not surprising that the minimum clearance has significant changes in Case III and there are two obvious peaks. The minimum clearance in Case II is larger than that in Case I and Case IV, even though the relative displacement in Case II is smaller than the other two cases (from Figure 3.4) . This is due to a smaller relative pitch in Case II than in the other two cases. Nevertheless, the minimum clearance is smaller in Case II than in Case I and Case IV when they undergo negative shocks.

The first few mode frequencies of the three drive components are listed in Table 3.1. It shows that the HAA's second mode frequency is very close to the disk's third forward mode frequency and the HAA's third mode frequency is close to the base plate's third mode frequency. It is also found that the disk's second forward mode frequency and the base plate's first mode frequency are near each other.

Table 3.1 Structure model frequencies

HAA		Disk			Base plate	
Mode	Frequency (Hz)	Mode	Frequency (Hz)		Mode	Frequency (Hz)
			Forward	Backward		
1st bending	472	(0,0)	1043	1043	Umbrella	1313
2nd bending	1631	(0,1)	1210	850	Bending	2243
Flexure	2489	(0,2)	1604	885	Twisting	2595
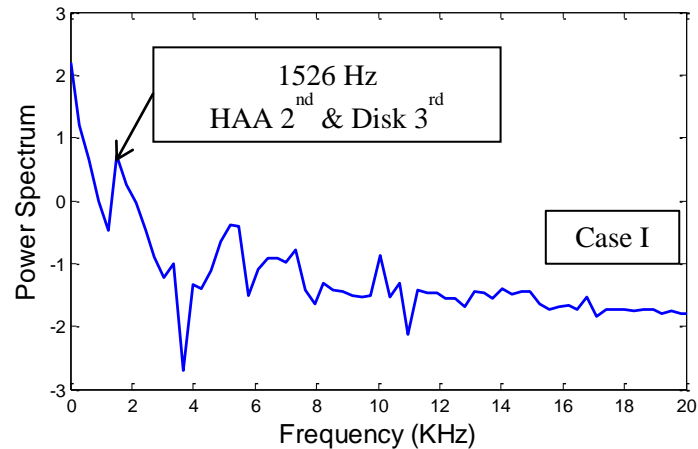
Figure 3.8 FFT of relative pitch in case I

Fast Fourier transform (FFT) analysis of the relative pitches for the four cases is carried out in order to study the components' effects on the HDI, and the results are plotted in Figure 3.8, 3.9, 3.10 and 3.11. From the result of Case I, it is found that the first peak frequency is 1526 Hz, which is close to the HAA's second mode and the disk's third forward mode frequencies. As the HAA and disk have fixed B.C. in Model I, the HDI is directly affected by the HAA and disk, just
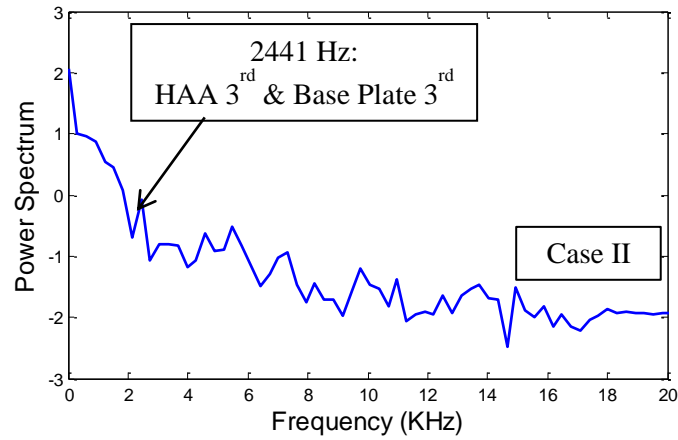
Figure 3.9 FFT of relative pitch in case II
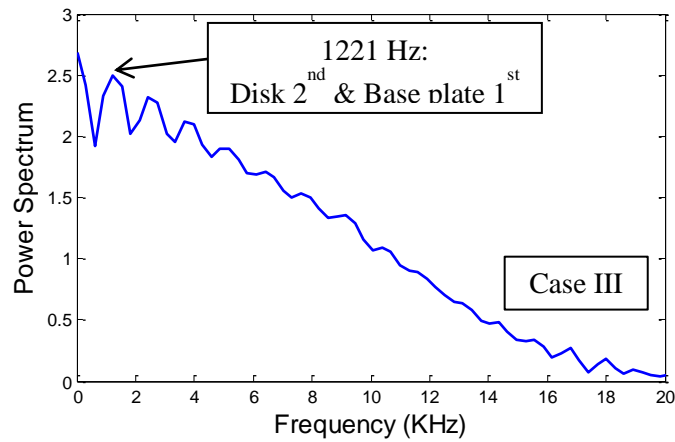
Figure 3.10 FFT of relative pitch in case III
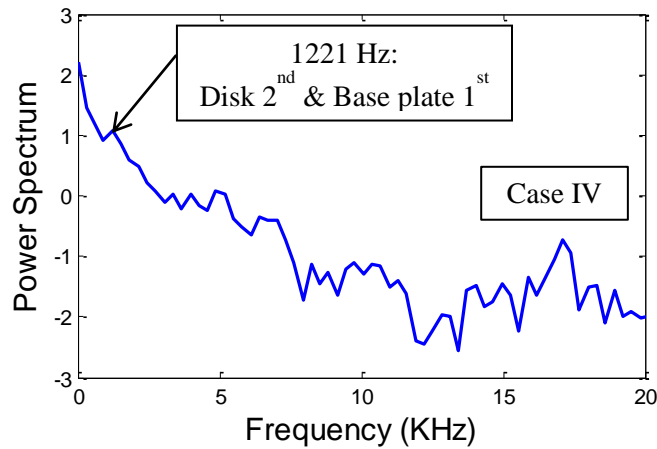
Figure 3.11 FFT of relative pitch in case IV

as predicted in Figure 3.8. The FFT result of Case II (Figure 3.9) shows that the HDI is mostly affected by the HAA and base plate as the first peak frequency is very close to the HAA's third mode and the base plate's third mode frequencies. It is because the disk is connected to the base plate in Model II, that the base plate's vibration affects the disk and the air bearing vibrations. Figure 3.10 and Figure 3.11 indicate that the HDI responses in Case III and IV are mostly affected by the disk and base plate. That is because in both cases the HAA is connected to the base plate, the HAA and the air bearing vibrations depend on the base plate's movement.

3.3.2 Head Disk Interface Failure Mechanism

In this dissertation, the minimum clearance between the slider and the disk surface (h_{min}) is used as the failure criterion. When h_{min} becomes less than zero, the HDI is failed. As the HDI failure mechanisms are the same when the HDD undergoes positive and negative shocks with short pulse width (≤ 1.0 ms), we only analyze a positive shock case. For a shock with long pulse width (>1.0 ms), however, the failure mechanisms are different for positive and negative shock cases. As the failure mechanisms for positive shock cases are the same for all ranges of pulse width, we will not show the HDI failure when the HDD is under a positive shock with long pulse width.
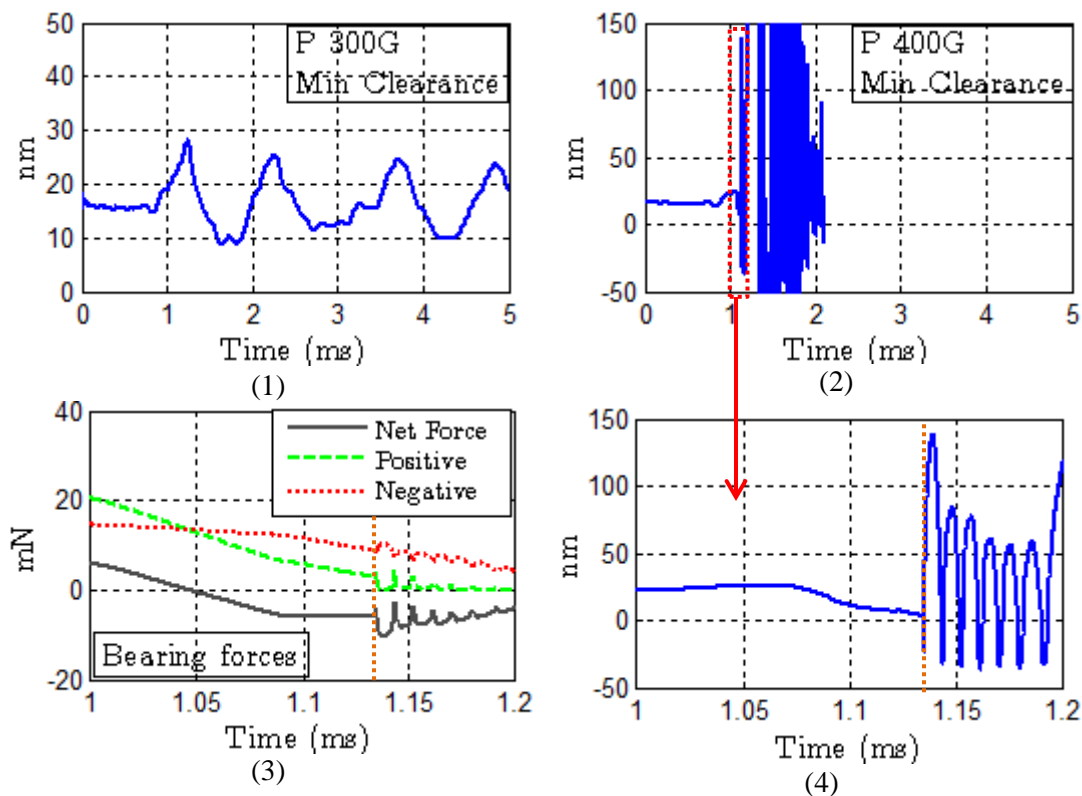
Figure 3.12 Failure mechanism for shock with short pulse width: (1) minimum clearance for positive shock 300 G; (2) minimum clearance for positive shock 400 G; (3) air bearing force corresponding to the case in (2); (4) zoom in of minimum clearance in (2).

3.3.2.1Failure Mechanism: positive shock with pulse width 0.5 ms

From Figure 3.12(1), it is seen that the slider is able to fly over the disk successfully when the shock amplitude is 300 G as the minimum clearance is larger than zero all the time. Nevertheless, the slider crashes on the disk when the amplitude is increased to 400 G (Figure 3.12(2)). From the zoom-in part of the minimum clearance (Figure 3.12(4)), the minimum clearance decreases from positive to negative directly without any oscillation. The air bearing forces presented in Figure 3.12(3) show that the net bearing force (grey curve) has decreased to a negative value before the minimum clearance becomes zero. The slider is pulled back to the disk due to the negative net bearing force until it crashes on the disk. This phenomenon is called the "head-slap". It can be explained as follows: when the relative displacement between the slider and the disk is increasing, the air between them is expanding, so the net bearing force will decrease to zero when the head disk spacing is big enough and the HAA's bending modes will be excited. The phase difference between the HAA and disk vibration causes the head-slap and HDI failure.

The slider' relative pitch and roll at a zoom-in period (1-1.5 ms) are plotted in Figure 3.13(1) and (2). It shows that the air bearing instability leads to negative values of pitch and roll. The x and y coordinates of the slider's minimum clearance location presented in Figure 3.13(3) and (4) indicate that the slider contacts the disk firstly at the inner trailing edge corner and then moves along the inner edge and leading edge. The slider-disk contact is also shown in Figure 3.14.
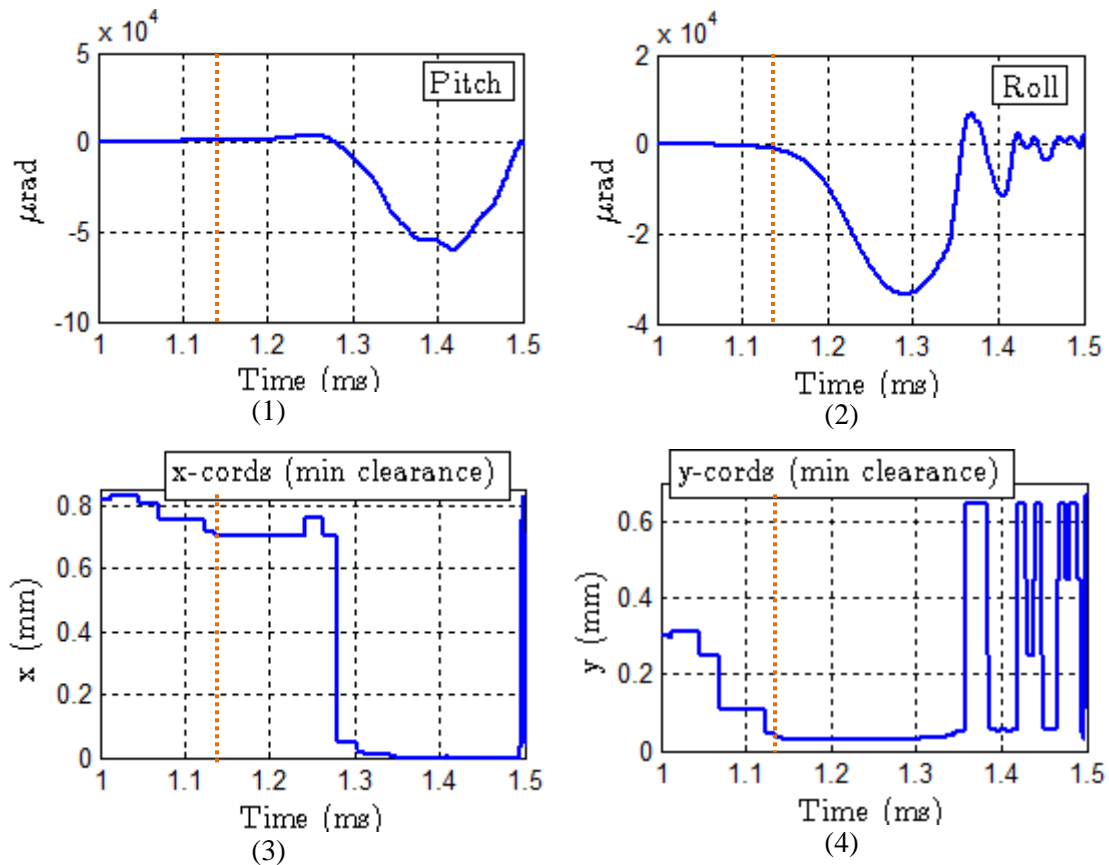
Figure 3.13 Slider's flying parameters for positive shock 400 G: (1) relative pitch; (2) relative roll; (3) x-coordinates for slider's minimum clearance point; (4) y-coordinates for slider's minimum clearance point.
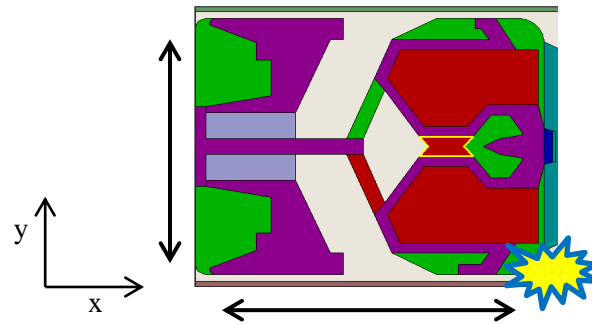
Figure 3.14 Slider's crash location

3.3.2.2 Failure Mechanism: negative shock with pulse width 2.0 ms

The minimum clearance in Figure 3.15(1) shows that the slider flies over the disk without any contact when the negative shock amplitude is 1500 G. However, the slider crashes on the disk (Figure 3.15(2)) if the shock amplitude is increased to 1600 G. From the zoom-in part of the minimum clearance (Figure 3.15(4)), it can be seen that the slider oscillates for a while before it
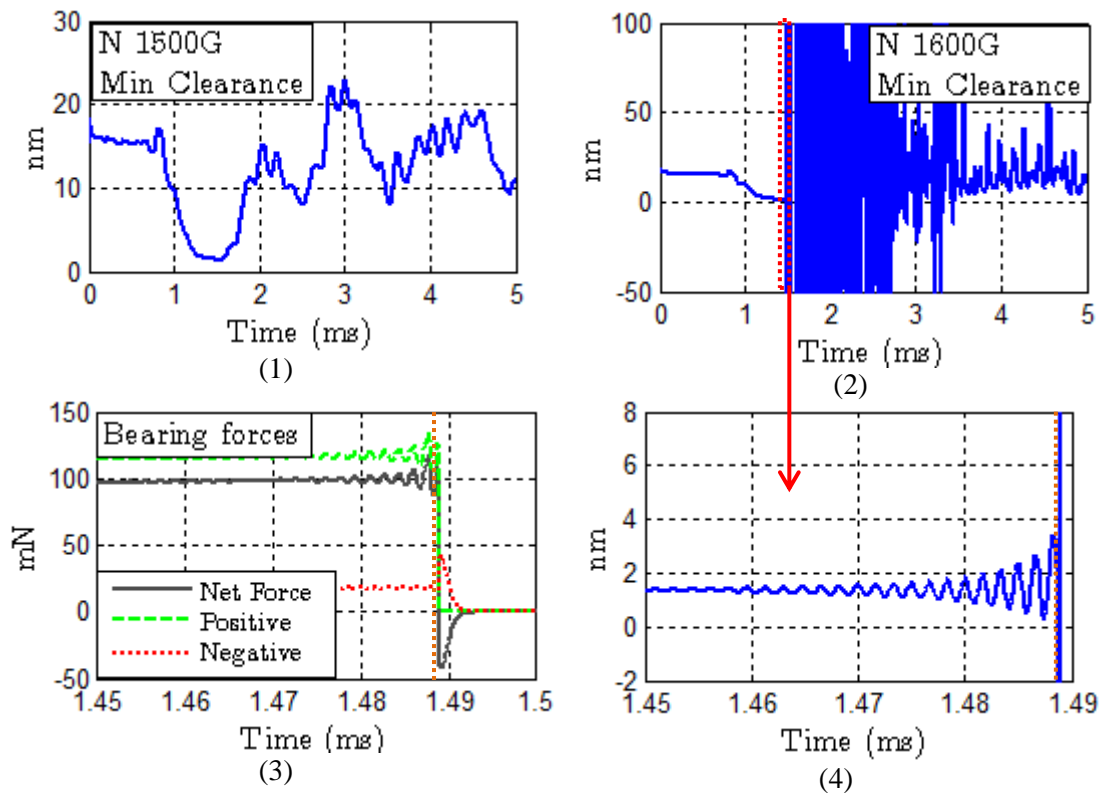
Figure 3.15 Failure mechanism for shock with long pulse width: (1) minimum clearance for negative shock 1500 G; (2) minimum clearance for negative shock 1600 G; (3) air bearing force corresponding to the case in (2); (4) zoom in of minimum clearance in (2).

starts to contact the disk. Figure 3.15(3) shows that the net air bearing force is positive before the minimum clearance becomes zero. Thus, the air bearing is stable before the slider crashes on the disk. In this negative shock case, the air flow is compressed so that the air bearing becomes very

stiff. That is why the net bearing force in Figure 3.15(3) is relatively large. The slider crashes on the disk only when the inertia load of the shock overcomes the air bearing force.

The x and y coordinates of the slider's minimum clearance location are presented in Figure 3.16. It indicates that the slider contacts the disk firstly at the leading edge center, and then moves along the leading edge. The crash location movement can be seen clearly in Figure 3.17.

(1)   (2)
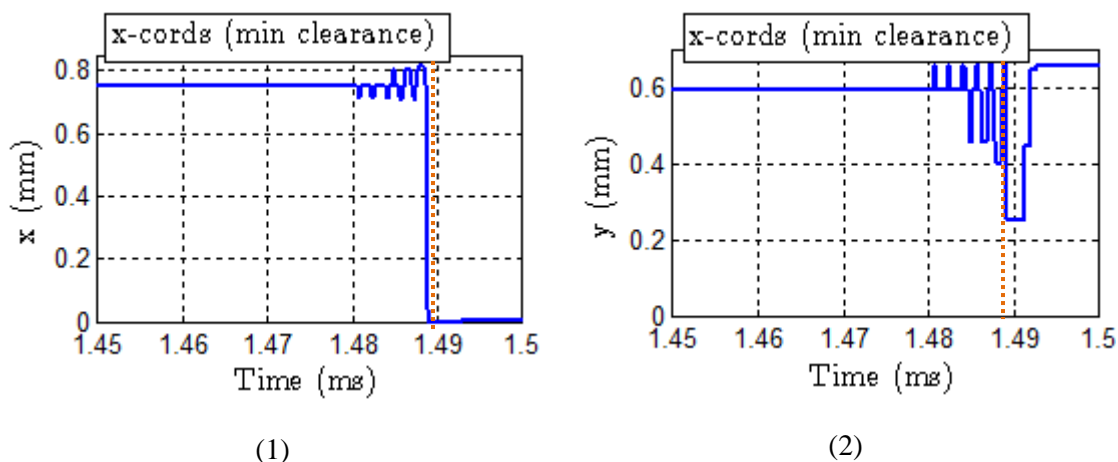
Figure 3.16 Slider's flying parameters for negative shock 1600 G: (1) x-coordinates for slider's minimum clearance point; (2) y-coordinates for slider's minimum clearance point.
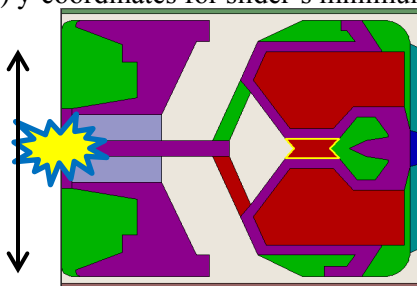
Figure 3.17 Slider's crash location

3.3.3 Critical Shocks

Critical shock is used as a measurement to determine the reliability of a mobile disk drive. It is defined as the maximum shock before the HDI fails. Figure 3.18 and Figure 3.19 present the critical shocks as functions of shock pulse width for the four models when the HDD undergoes positive and negative shocks, respectively. From both figures, it is observed that the critical shock amplitude increase with the increase of pulse width. The case with long pulse width means a disk drive drops on a soft floor such as carpet while the case with short pulse width models a disk drive falling on a hard floor like concrete. A HDD is easier to be damaged when it is dropped on a hard floor. That is why a smaller critical shock is obtained for short pulse width cases. Comparing the critical shock magnitudes for positive cases with negative cases, it is found that the negative critical shock amplitudes are larger than the positive critical shock amplitudes when the pulse width is long. The reason can be explained as: the air between the slider and disk expands when the drive experiences a positive shock, so the air bearing becomes weak; for a negative shock case the air is compressed so that the air bearing is very stiff. As the failure

mechanisms are the same for the positive and negative shock cases when the pulse width is short, the critical shocks shown in the two figures are very close. The critical shock difference for the four models indicates that Model I predicts higher values for both positive and negative cases, while Model III predicts the lowest values except in a negative shock case with long pulse width. As the minimum clearance is smaller in Case II than in the other cases when the drive is under a negative shock with long pulse width, the negative critical shock of Case II with pulse width of 3.0 ms is smallest. The critical shocks of Model IV, which is closest to a real HDD, have an almost constant offset from the critical shocks of Model I for both positive and negative cases except for the shock cases with a pulse with of 3.0 ms.
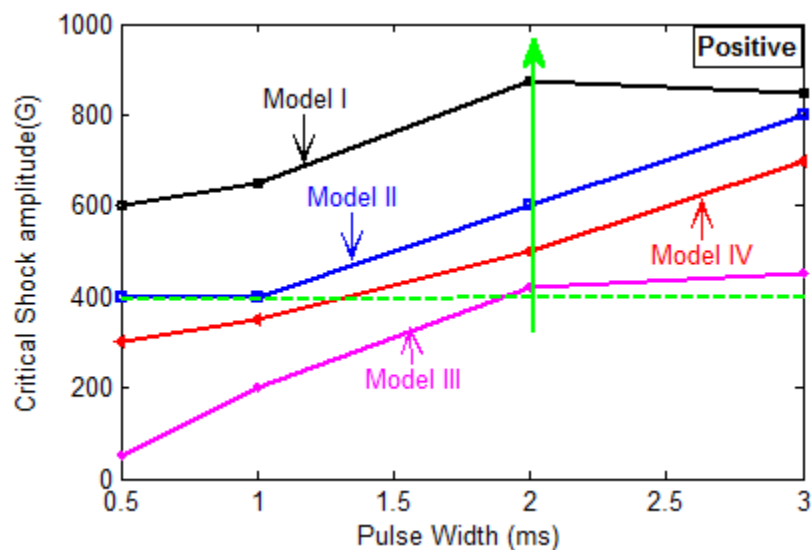
Figure 3.18 Critical shocks of the four models for positive shock
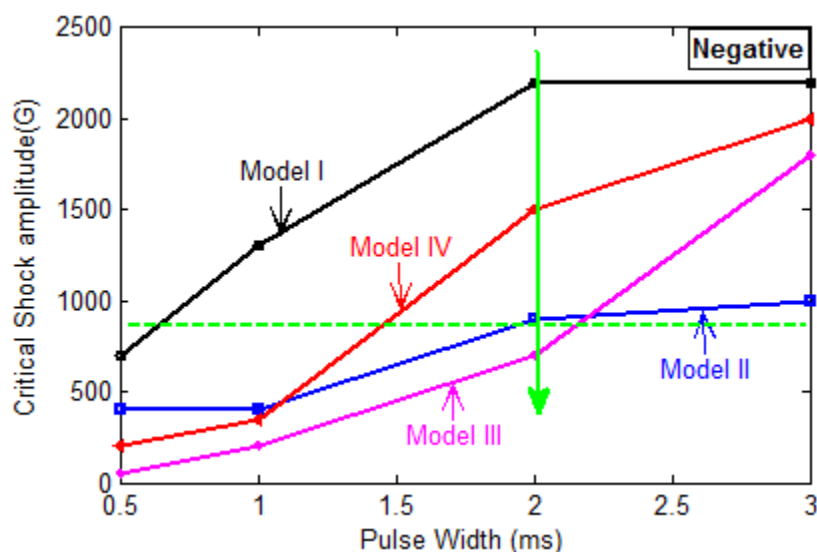
Figure 3.19 Critical shocks of the four models for negative shock

3.4   Operational shock simulation for a TFC Slider

As the TFC technology has been applied to most state-of-art HDDs, we carried out an op-shock simulation for a TFC slider to investigate the thermal protrusion effects on the HDI response during a shock. The ABS design and thermal protrusion profile used in this study are shown in Figure 3.20. The rectangle dotted area is the region that has been protruded out due to the thermal expansion of a heater element. As the critical shocks of the full HDD model have an almost constant offset from that of the disk model, the disk model is used in this investigation.

(1)   (2)
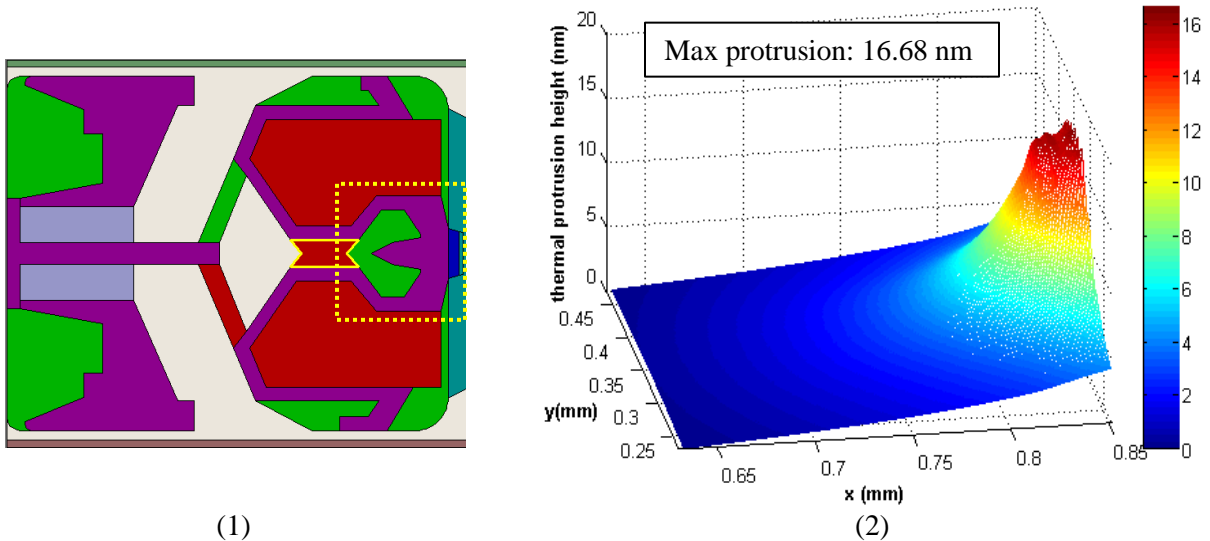
Figure 3.20 Shock simulation for a TFC slider: (1) ABS design; (2) thermal protrusion profile

Static analysis of a TFC slider's flying attitude shows that its minimum clearance is smaller, pitch is slightly larger and roll is almost the same when comparing with the results for a non-TFC slider. More details of the analysis of TFC sliders can be found in [53]. Figure 3.21 compares the HDI responses of a non-TFC slider and a TFC slider for positive shock cases with shock amplitude of 800 G and pulse width of 2.0 ms. Figure 3.21(1) and (4) show that, before the shock is applied (< 0.5 ms), the minimum clearance of the non-TFC slider is larger than that of the TFC slider, which is the same as the static analysis. During the shock period, however, the minimum clearances are quite similar for these two sliders. Moreover, both of them have depressions at around 1.5 ms due to the phase difference between the HAA and the disk vibrations. The non-TFC slider's pitch (Figure 3.21(2)) during the shock period is slightly larger than the TFC slider's pitch and a larger pitch usually leads to a smaller minimum clearance. Because of that, the minimum clearances for the two sliders are similar to each other during the shock period although there is a protrusion underneath the TFC slider. For negative shock cases, the HDI response differences for the two sliders are the same as in the static analysis and we predict that a TFC slider is easier to crash on the disk because the slider's minimum clearance is smaller.

Next we investigate the HDI failure mechanisms in order to understand how the TFC slider crashes on the disk. As the failure mechanisms are different for positive and negative shock cases, we select both cases with pulse width of 2.0 ms in this study. The failure mechanism for positive

shock is explained in Figure 3.22 and Figure 3.23. From Figure 3.22, it is found that the slider crashes on the disk because of the "head-slap" caused by the air bearing instability. It is the same as the failure mechanism for the non-TFC slider. Moreover, the contact regions also occur on the inner edge and leading edge. However, the negative shock failure mechanism (Figure 3.24) is quite different from the previous analysis for the non-TFC slider. The slider crashes on the disk directly without any oscillation (Figure 3.24(4)) and the air bearing force does not decrease to zero after the slider contacts the disk at around 1.08 ms. One reason might be that the slider only contacts the disk with a small region and all other parts of the slider can still fly over the disk to construct the air bearing. This is verified by Figure 3.25, which shows that the slider only contacts the disk at the trailing edge center. As the maximum thermal protrusion is also located around the trailing edge center, we can conclude that the TFC slider crashes on the disk with the protrusion tip during a negative shock.
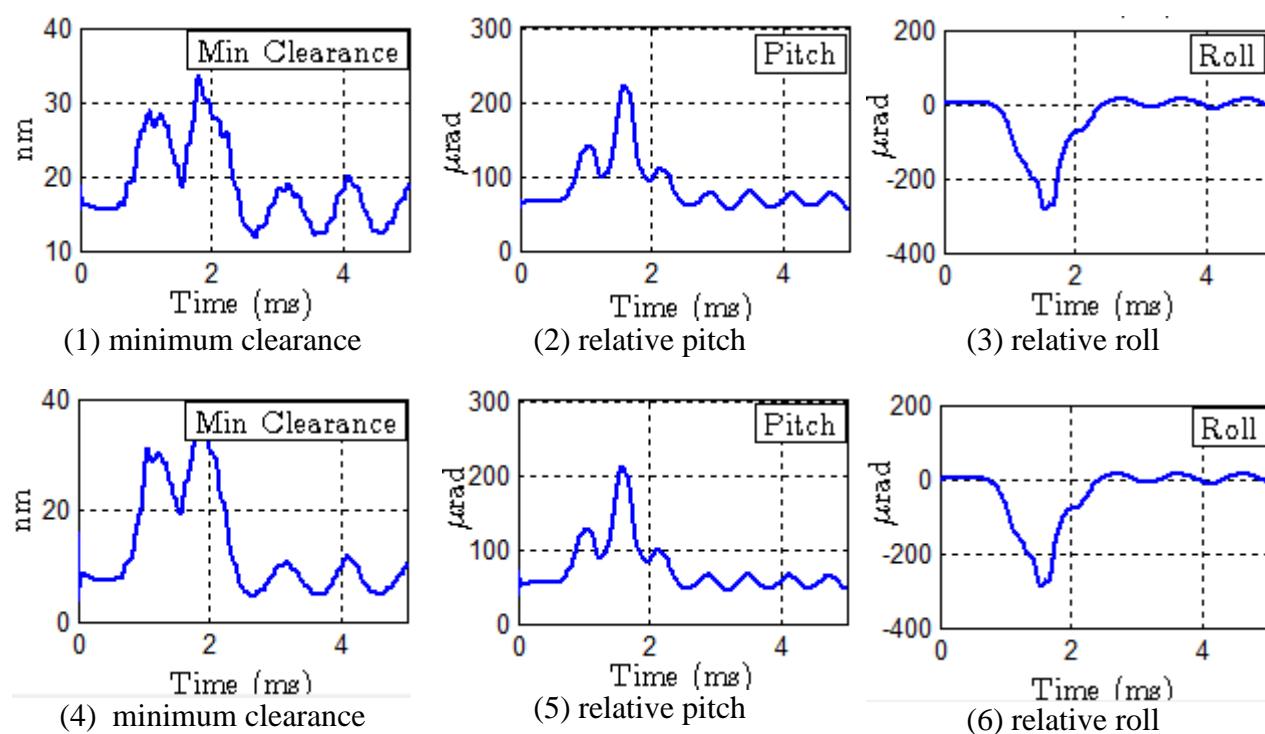
Figure 3.21 HDI response for non-TFC and TFC sliders during a positive shock with amplitude 800 G and pulse width 2.0 ms: (1) (2) (3) are for non-TFC slider; (4) (5) (6) are for TFC slider.
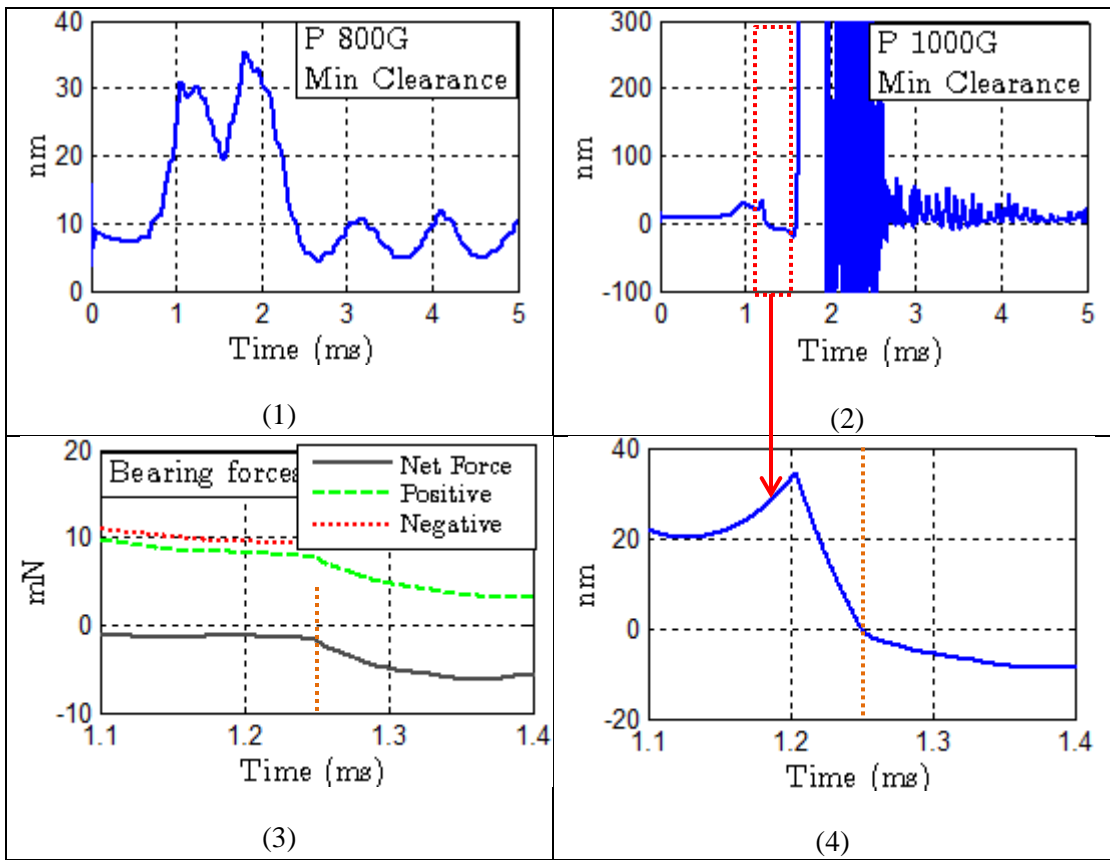
Figure 3.22 TFC slider failure mechanism for positive shock: (1) minimum clearance for positive shock 800 G; (2) minimum clearance for positive shock 1000 G; (3) air bearing force corresponding to the case in (2); (4) zoom in of minimum clearance in (2).
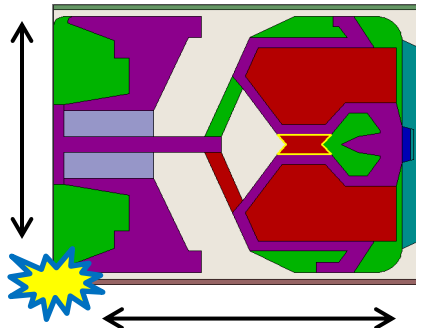
Figure 3.23 TFC slider's crash location during positive shock
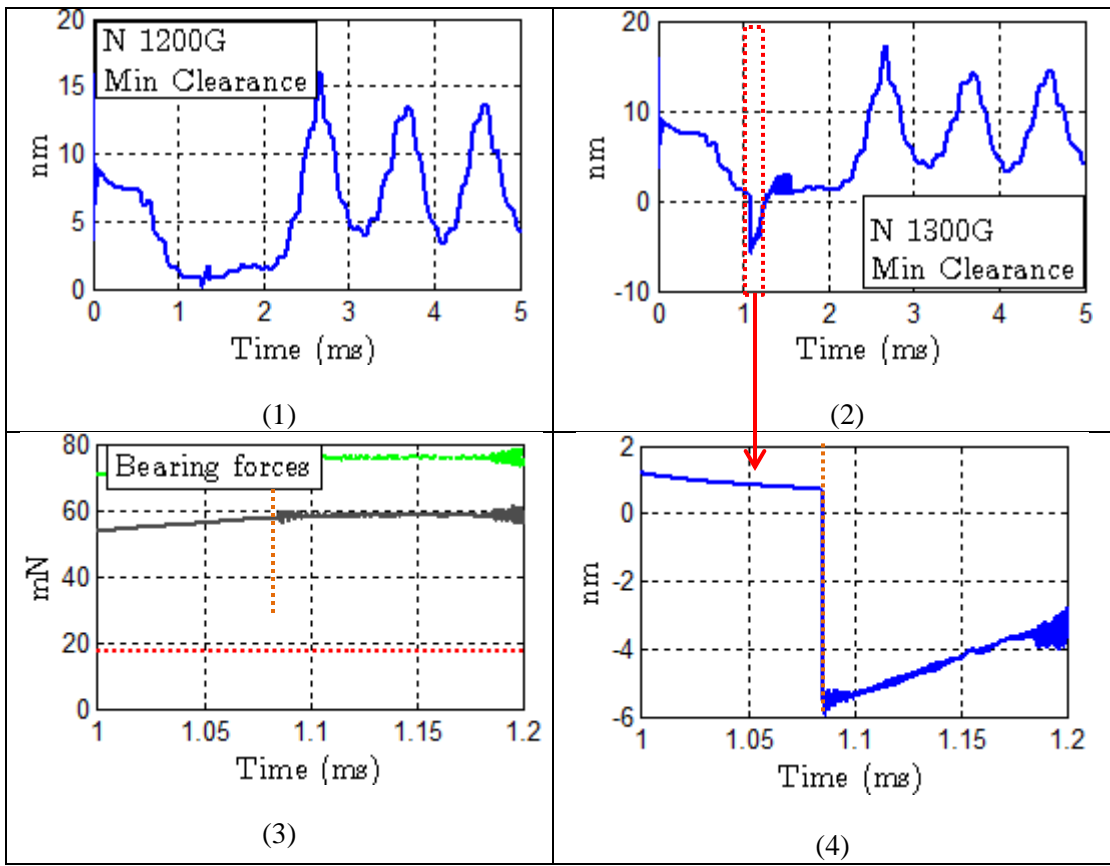
Figure 3.24 TFC slider failure mechanism for negative shock: (1) minimum clearance for negative shock 1200 G; (2) minimum clearance for negative shock 1300 G; (3) air bearing force corresponding to the case in (2); (4) zoom in of minimum clearance in (2).
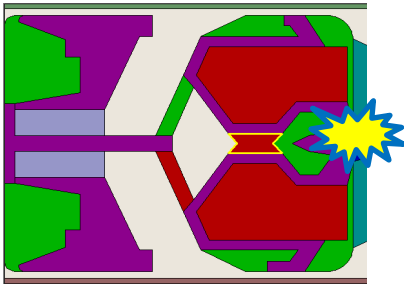
Figure 3.25 TFC slider's crash location during negative shock

The positive and negative critical shocks with different pulse widths for the TFC and non-TFC sliders are plotted in Figure 3.26. It shows that the positive critical shocks are very close to each other for these two sliders. It can be explained as follows: the two sliders have almost the same minimum clearances when they are experiencing the same positive shock and the HDI failure mechanisms are the same for the two sliders during positive shocks. However, the negative critical shocks of the TFC slider are much smaller than that of the non-TFC slider. This difference is mainly caused by the different failure mechanisms. A TFC slider can more easily crash on the disk during a negative shock because the extra protruded tip tends to contact with the disk more easily.
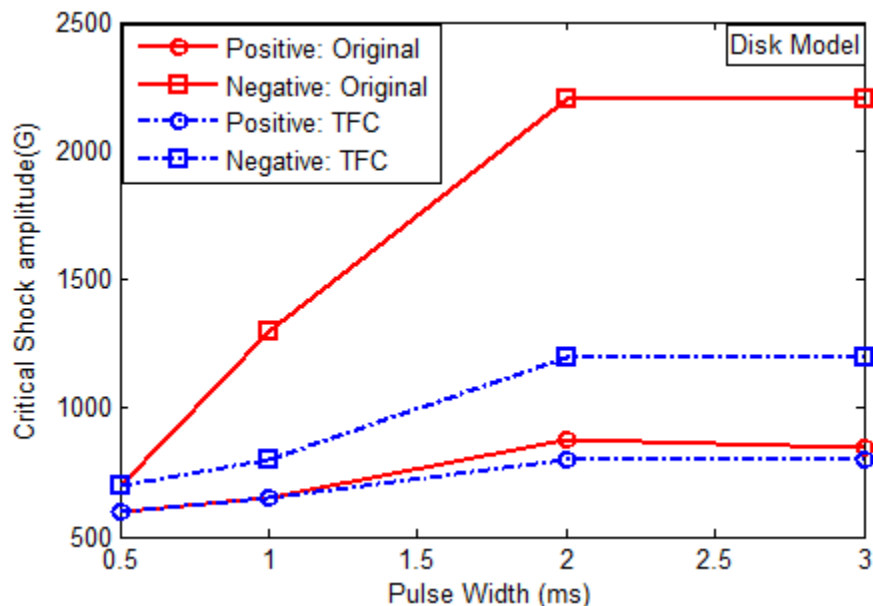
Figure 3.26 Critical shocks comparison between non-TFC slider and TFC slider

3.5 Conclusion

In this chapter, the shock responses of the mechanical system and HDI have been investigated using the multi-body op-shock model developed in Chapter 2. We first studied different components' effects on the responses of the structure and the HDI by simulating the four models: the disk model, the disk support model, the actuator model and the full model. It is found that the components have significant effects on the HDI response. The air bearing is mainly affected by the disk and the HAA in Model I; while in Model II it is mainly affected by the base plate and the HAA; for Model III and Model IV, the disk and the base plate play a more prominent role on the HDI response. The HDI failure mechanisms are also investigated for different shock cases. The analysis shows that, for a negative shock with long pulse width, the slider crashes on the disk when the inertia force of the shock overcomes the air bearing force; for all other shocks, the failure of the HDI is caused by the "head-slap" when the air bearing becomes unstable.

The critical shock is a very essential criterion to tell the robustness of an air bearing system. The critical shock study for the four models shows that the disk model predicts higher amplitude critical shock values for both positive and negative shocks. The full model, closest to the real

HDD model, can also resist large positive and negative shocks and there is an almost constant offset between the critical shocks of the disk model and the full model, which indicates that the component level (disk model) tests may be useful for predicting the drive level (full model) results. For all the four models, the drive can resist a large critical shock if the shock pulse width is longer. Negative critical shocks are usually larger than positive critical shock values for the same model especially when the shock pulse width is long. This difference of the positive and negative critical shock values is mainly due to the different failure mechanisms.

As the TFC technology is currently widely used in most of the HDDs, the thermal protrusion effects on the HDI response during a shock has also been investigated. It is found that the negative critical shock value with long pulse width reduces significantly when the TFC power is on. That is because the thermal protrusion tip tends to contact the disk. The failure mechanisms for other shock cases are the same with or without the TFC power is on, and there is no significant difference in the critical shock values between the TFC slider and non-TFC slider.

Chapter 4 Ramp Effects in Head Disk Interface Response during Operational Shock Events

4.1 Introduction

The ramp LUL technology in HDDs was introduced in the mid-1990s as a better alternative to contact start-stop (CSS) [54]. In the CSS method, the sliders, which carry the R/W transducers, rest on a laser landing textured zone on the disk surface when the power is off, and stay on the disk until the power is turned on. There are several limitations for the CSS method, such as serious wear problems, less usage of disk media surface for data, etc. The ramp LUL technology has been proved to be a historic breakthrough because of the advantages of increasing areal density, greater durability, more efficient power utilization and superior shock resistance. In this method, the slider is lifted off the disk and parked on the ramp which sits near the outer radius of the disk (Figure 4.1) when the power is off. During a powering-on process, the slider is moved off the ramp and over the disk surface when the disk reaches an appropriate spinning speed and establishes its air bearing. Most of the current commercial mobile drives apply the LUL ramp technology.

However , the application of the LUL ramp in the HDDs introduces the possibility of collision between the disk and ramp during the op-shock as the ramp sits on the side closest to the disk. So it is extremely important to study the ramp effects on the HDI response during an op-shock event. Various experimental and simulation studies [16-28] have been done to investigate the shock response of the mechanical system and the HDI in the past. However, the LUL ramp was not implemented in their models. Rai and Bogy [29, 55] proposed a method in which both the structural and the air bearing were modeled in detail and were coupled with each other. However, in their research the ramp was modeled as a rigid body (Figure 4.2) and was fixed; hence the flexibility of the ramp effects was neglected.

In this investigation, a deformable ramp model is developed and the ramp constraint is implemented to the disk's vibration. Numerical analyses using three ramp models (the no-ramp model, the rigid ramp model and the deformable ramp model) are carried out to study the ramp effects on the HDI response.

4.2 Ramp Models

As we discussed in Chapter 2, the HDI in a mobile drive consists of a slider and a spinning disk, which are coupled through an air bearing. Hence the stability of the HDI depends on the dynamic response of the structural components in a HDD. The current model consists of a slider-disk pair and a ramp which is at the outer edge of the disk. The deformable ramp model is created in commercial FE software ANSYS and is shown in Figure 4.3.
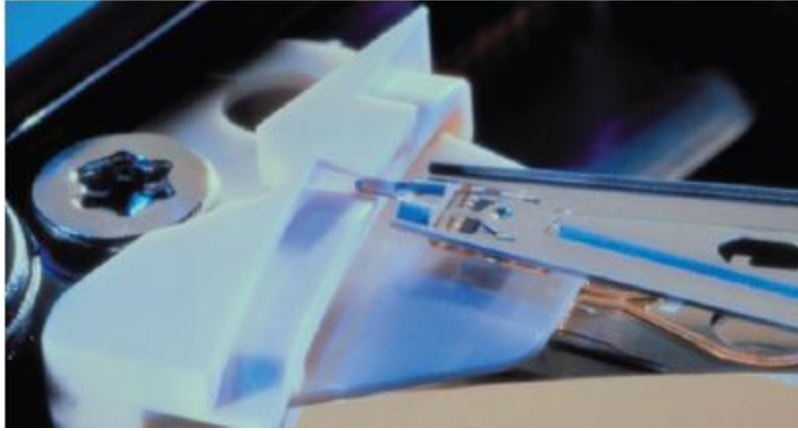
Figure 4.1 A slider parking on the ramp [54]
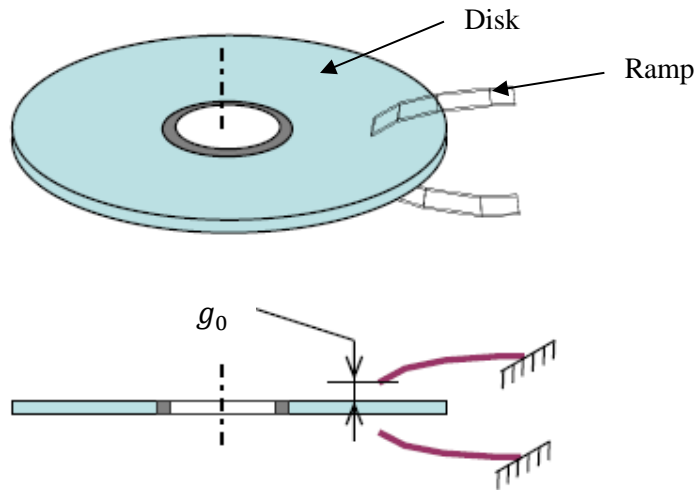
Figure 4.2 Rigid ramp model and g_0 is the clearance between the ramp and disk.
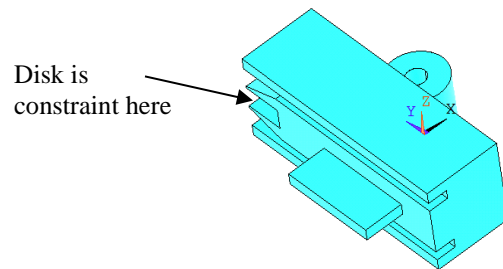
Figure 4.3 Deformable ramp model

The constraint imposed by the ramp on the spinning disk can be expressed as:

$$\left|w_{disk}(r_{ramp}, \theta_{ramp})\right| \leq \left|w_{ramp}\right| + g_0 \tag{4.1}$$

where g_0 is the minimum designed static clearance between the disk and the ramp and is chosen to be 100 μm in this investigation. w_{disk} is the disk transverse displacement at the ramp position, which is determined by the radius r_{ramp} and angular θ_{ramp}. w_{ramp} is the ramp displacement, which is equal to zero in the rigid ramp model.

So the ramp constraint can simply be written as:

$$[Q]\{u\} = \{g_0\}. \tag{4.2}$$

For the top ramp, $[Q] = [1 \quad -1]$, $\{u\}=\begin{Bmatrix} w_{disk} \\ w_{t\_ramp} \end{Bmatrix}$; while for the bottom ramp, $[Q] = [-1 \quad 1]$, $\{u\}=\begin{Bmatrix} w_{disk} \\ w_{b\_ramp} \end{Bmatrix}$. w_{t_ramp} and w_{b_ramp} are the top and bottom ramp displacements, respectively.

4.3 Dynamic Formulation and Its Transient Solution

The disk-ramp contact is simplified as a point-to-point contact, so a Lagrange multiplier method is used to model the ramp constraint to the disk's displacement. So the dynamic equation of motion can be written as:

$$\begin{cases} [M]\{\ddot{u}\} + [C]\{\dot{u}\} + [K]\{u\} + [Q]^T\{\lambda\} = \{F\} \\ [Q]\{u\} = \{g_0\} \end{cases}, \tag{4.3}$$

where λ is the reaction force arising due to the ramp constraint.

Discretizing the time into uniform time steps of Δt, the equation of motion at time $t = t_{n+1}$ is as follows:

$$\begin{cases} [M]\{\ddot{u}\}_{n+1} + [C]_{n+1}\{\dot{u}\}_{n+1} + [K]_{n+1}\{u\}_{n+1} + [Q]^T_{n+1}\{\lambda\}_{n+1} = \{F\}_{n+1} \\ [Q]_{n+1}\{u\}_{n+1} = \{g_0\} \end{cases}. \tag{4.4}$$

Similarly used in Chapter 2, the Newmark-Beta scheme is implemented to solve the above equation. After some algebraic calculation, the final equation of motion can be written as:

$$\begin{bmatrix} [A]_{n+1} & [Q]^T_{n+1} \\ [Q]_{n+1} & [0] \end{bmatrix} \begin{Bmatrix} \{\ddot{u}\}_{n+1} \\ \{\lambda\}_{n+1} \end{Bmatrix} = \begin{Bmatrix} \{X\}_{n+1} \\ \{Y\}_{n+1} \end{Bmatrix}, \tag{4.5}$$

where

$$[A]_{n+1} = [M] + \gamma\Delta t[C]_{n+1} + \beta\Delta t^2[K]_{n+1}, \tag{4.6a}$$

$$\{X\}_{n+1} = \{F\}_{n+1} - [C]_{n+1}\{\dot{\tilde{u}}\}_{n+1} - [K]_{n+1}\{\tilde{u}\}_{n+1}, \tag{4.6b}$$

$$\{Y\}_{n+1} = \left(\frac{1}{\beta\Delta t^2}\right)(\{g_0\} - [Q]_{n+1}\{\tilde{u}\}_{n+1}). \tag{4.6c}$$

The simulation process is quite similar to the simulator for the multi-body op-shock model. The main difference is in the computation of the structural displacements. In this ramp model two steps are needed to determine the structural displacement at each time step. The program flow chart to calculate the structural displacement is shown in Figure 4.4. In the first step, we

assume there is no disk-ramp contact, so we only need to solve the equation $[A]_{n+1}\{\ddot{u}\}_{n+1} = \{X\}_{n+1}$. After the accelerations, velocities and displacements of the disk and the ramp have been calculated, the constraint equation $[Q]_{n+1}\{u\}_{n+1} = \{g_0\}$ is used to check whether the disk contacts the ramps. If contact occurs, then Eqn. (4.5) is solved; otherwise the program goes to the next step directly.

Assuming no disk ramp contact and solve structural dynamic equation

If $[Q]\{u\} \geq \{g_0\}$ No

Compute the structural displacement

Yes

Add disk ramp contact constraint equation and solve structural dynamic equation

Next step
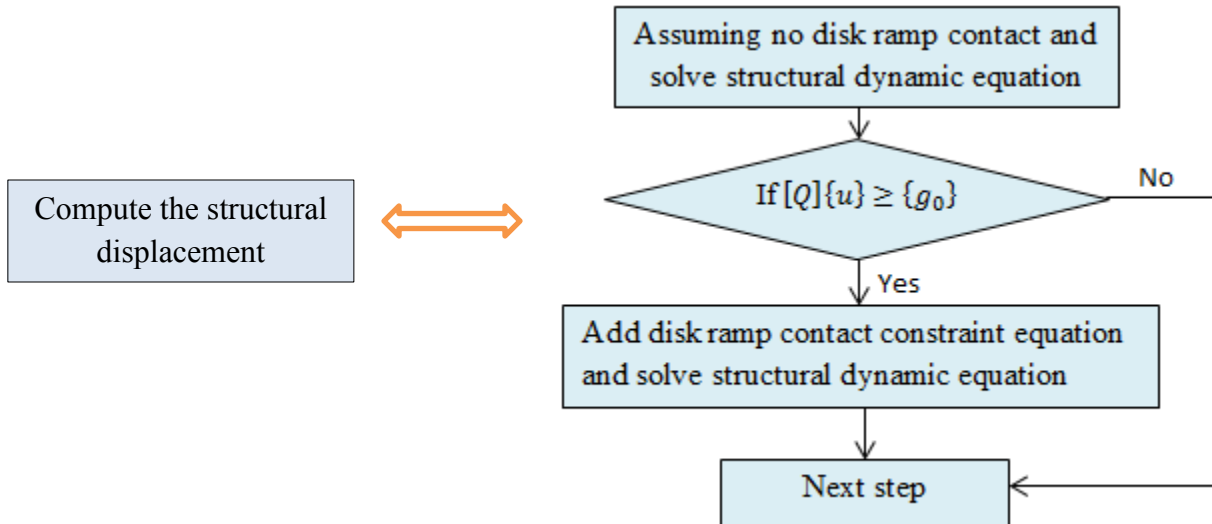
Figure 4.4 Flowchart to determine the structural displacement in the ramp model

4.4 Ramp Effects on the Head Disk Interface Response

We will first use the disk model to study the ramp effects on the HDI response.

4.4.1 Three Ramp Models for Shock Case with Pulse Width of 2.0 ms

In this section we choose a positive shock with amplitude of 400G and pulse width of 2.0 ms to study the HDI responses in three cases: the no-ramp model, the rigid ramp model and the deformable ramp model. Figure 4.5 shows the disk's absolute displacement at the slider's center position for the three cases. Figure 4.5(1) shows that the disk moves smoothly during the simulation time and there is no disk-ramp contact force as shown in Figure 4.6(1). The disk's displacement in the rigid ramp model (Figure 4.5(2)) shows that the disk could not move upwards any more after 1 ms, and the maximum disk's displacement at the slider's center is about 50 µm. The reason is that the slider is flying on the mid-radius of the disk and the disk's outer radius' displacement is about 100 µm. Figure 4.6(2) confirms that the disk contacts the ramp at 1 ms. For the deformable ramp model, it is also found that the disk contacts the top ramp at about 1 ms as can be seen in Figure 4.6(3). However, the disk moves upwards continuously even after contact with the top ramp (Figure 4.5(3)). Moreover, the disk moves smoothly during the simulation period, which is different from the rigid ramp model.

Figure 4.7 plots the movement of the disk's outer radius and the top ramp for the moveable ramp model. It clearly shows three collisions between the disk and the top ramp while the disk continues its original movement direction after collisions.

(1)   (2)   (3)
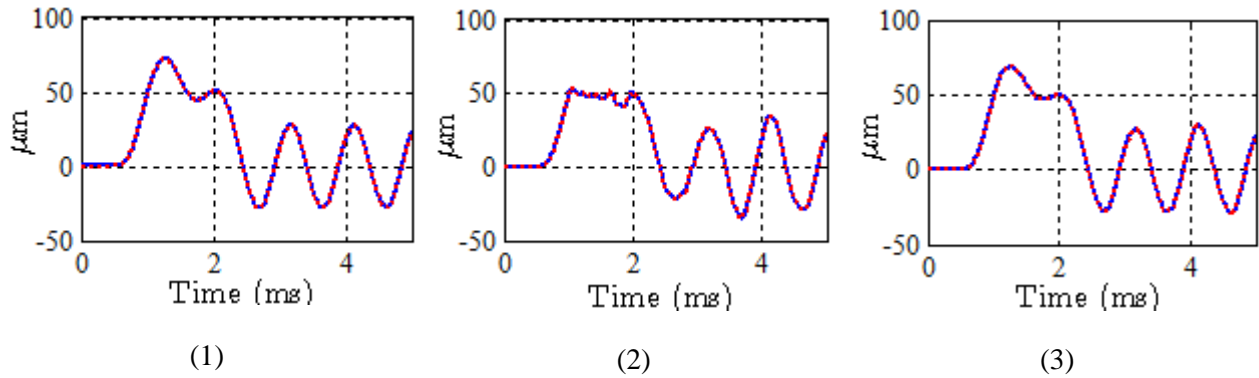
Figure 4.5 Disk absolute displacement at slider center position: (1) no ramp model; (2) rigid ramp model; (3) deformable ramp model.

(1)   (2)   (3)
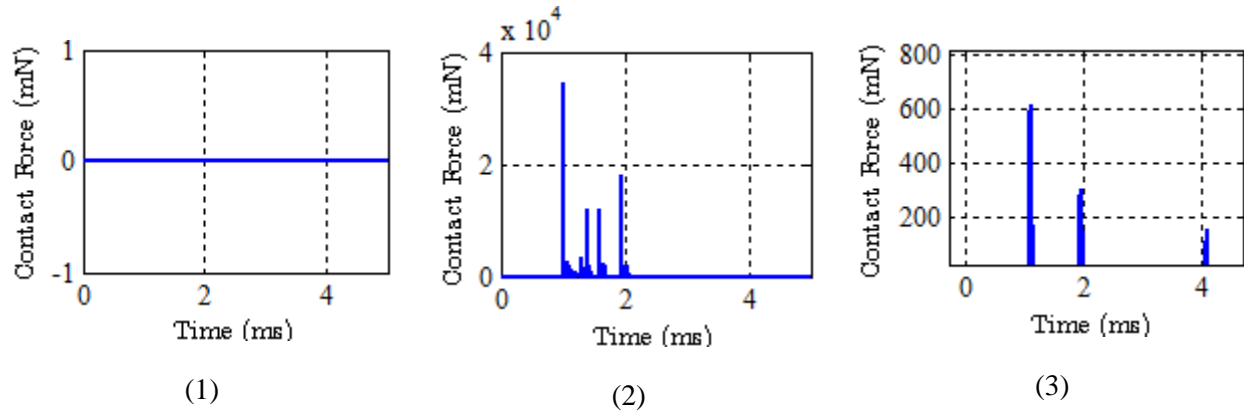
Figure 4.6 Disk-ramp contact forces: (1) no ramp model; (2) rigid ramp model; (3) deformable ramp model
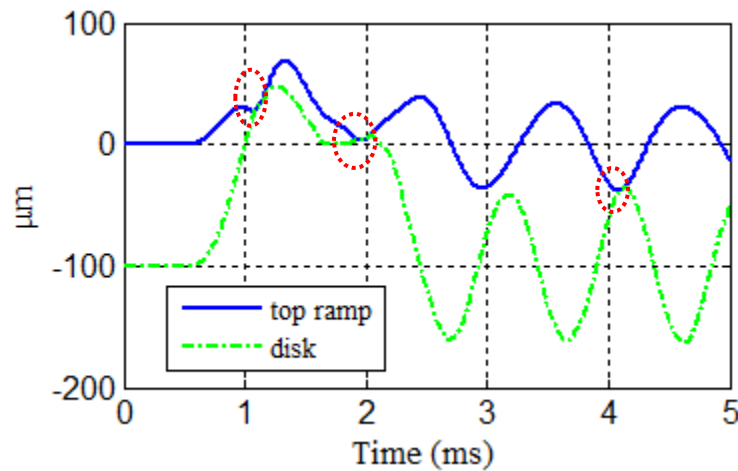
Figure 4.7 Disk and top ramp displacement at ramp position
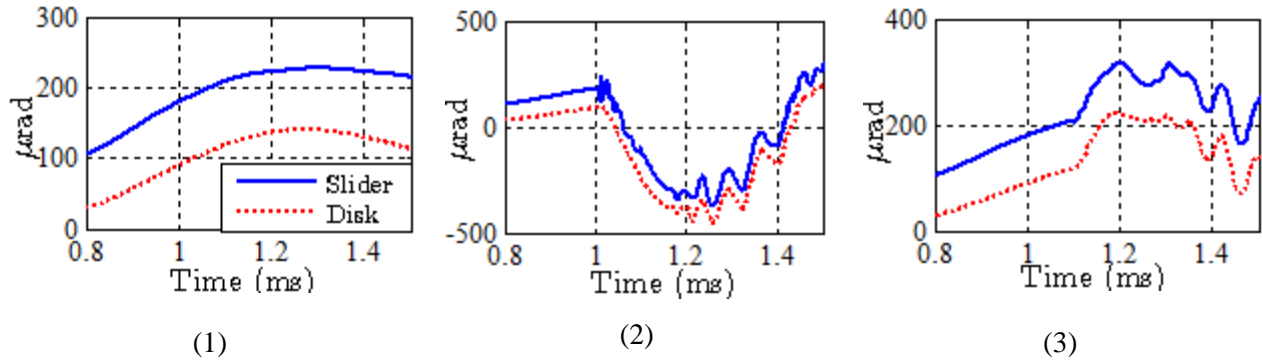
Figure 4.8 Disk absolute pitch at slider center position: (1) no ramp model; (2) rigid ramp model; (3) deformable ramp model.
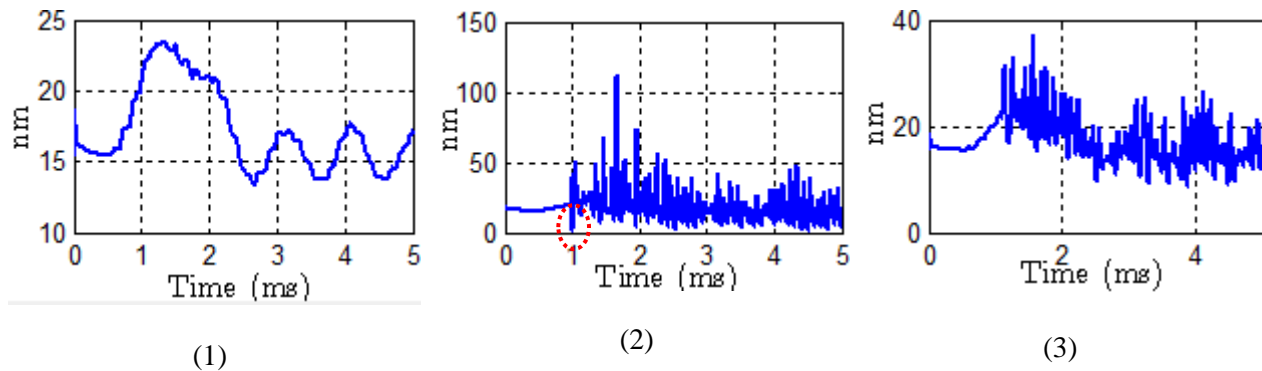
Figure 4.9 Minimum clearance between the slider and disk: (1) no ramp model; (2) rigid ramp model; (3) deformable ramp model

Figure 4.8 shows the zoom-in parts (0.8~1.5 ms) of the disk's (dotted red line) and the slider's (solid blue line) absolute pitches at the slider's center position. Similar to the disk's displacement, the pitches change smoothly in the no-ramp model. In the rigid ramp model, the disk has a big circumferential slope change due to the disk-ramp contacts. The change of the disk's circumferential slope mostly contributes to its pitch in the slider's coordinate system. Therefore, the disk has a sudden pitch change at around 1 ms as shown in Figure 4.8(2). The solid blue line in Figure 4.8(2) indicates that the slider's pitch tries to follow the pitch of the disk. However, the suspension's high frequency bending modes and the air bearing's pitch modes are excited during this period (see the oscillations), which may lead to an unstable air bearing. Figure 4.9(2) is the minimum clearance between the slider and the disk. It shows that the slider contacts the disk at 1 ms, which may be caused by the air bearing instability. In the deformable ramp model, the disk also has a circumferential slope change (dotted red line in Figure 4.8(3)), so we can still see the pitch changes for the disk and the slider. Although the slider follows the disk's movement much better in the deformable ramp model than in the rigid ramp model, the suspension's higher frequency bending modes are excited as well, as can be seen in Figure 4.9(3). However, the slider can still fly over the disk successfully.

From the above comparison of the three models, it seems that the ramps can adversely affect the HDD's working performance during the op-shock event. However, the deformable ramp model, which is closer to the real HDD ramp model, has a better HDI response than the rigid ramp model.

4.4.2 Shock Case with Pulse Width of 0.5 ms
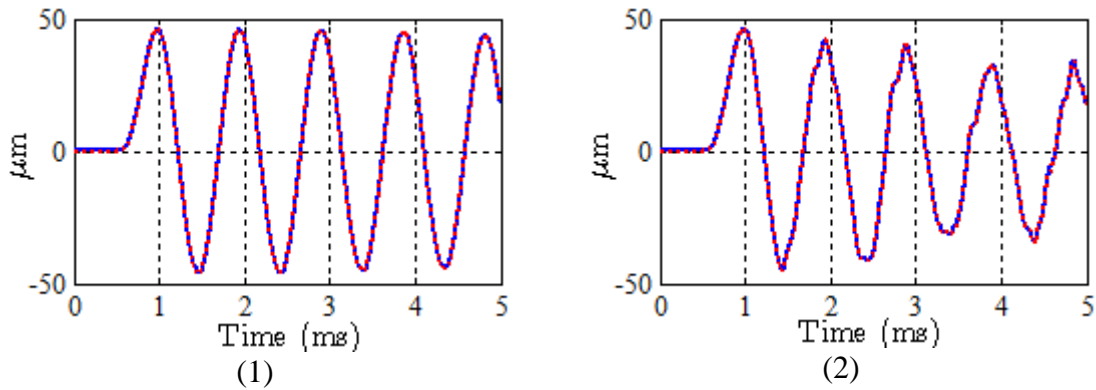
Figure 4.10 Disk absolute displacement: (1) rigid ramp model; (2) deformable ramp model.
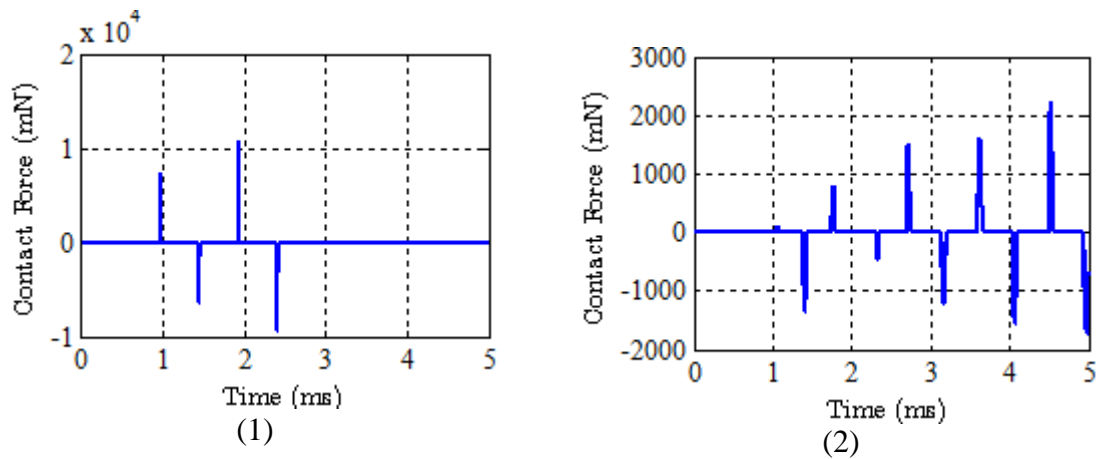
Figure 4.11 Disk-ramp contact force: (1) rigid ramp model; (2) deformable ramp model.
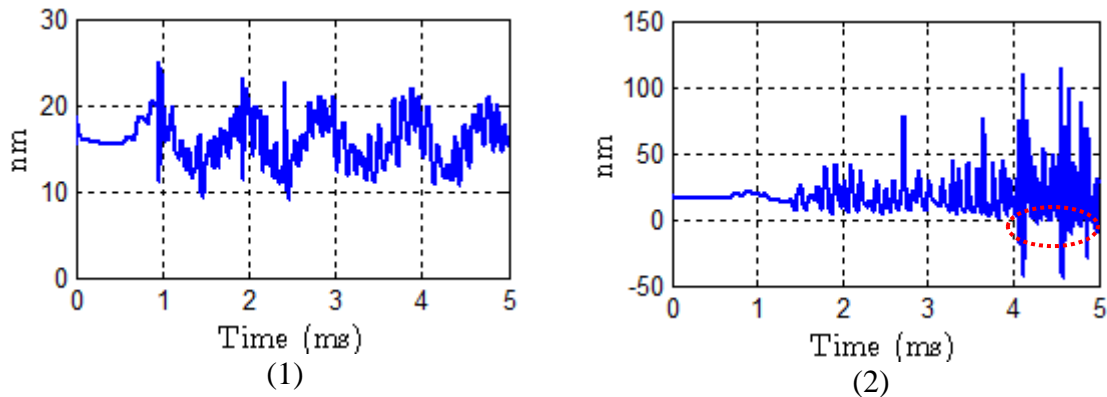
Figure 4.12 Minimum clearance: (1) rigid ramp model; (2) deformable ramp model.

In this section, an op-shock with shock amplitude of 200G and pulse width of 0.5 ms is applied to the rigid ramp model and the deformable ramp model. As the excitation frequency is 1 kHz for this shock, which is close to the disk's first mode frequency, the disk's first mode gets excited and its vibration amplitude should be almost constant if there is no disk-ramp contact. Figure 4.10(1) shows that the disk vibrates at an almost constant magnitude and the maximum

displacement is slightly less than 50 μm. The contact force figure in Figure 4.11(1) indicates that the disk contacts the ramps four times. However, the disk-ramp contacts do not affect the disk's movement much as can be seen in Figure 4.11(1). That is because the disk's maximum displacement at the ramp position just approaches the disk-ramp minimum clearance. Moreover, the slider can fly over the disk successfully as can be seen in Figure 4.12(1). However, the structural and HDI responses are quite different for the deformable ramp model. From Figure 4.10(2), it is found that the disk's displacement at the slider's center position decays obviously. Figure 4.11(2) shows that the disk contacts the top and bottom ramps periodically, and the contact force amplitude increases when the time increases. It can be explained as: because there is a phase difference between the disk's and ramp's movement, the residual vibrations of the disk and ramp increase the disk-ramp contact force; the increasing disk-ramp contact force again changes the disk's displacement. The severe change of the disk's displacement also affects the slider's flying attitude and leads the slider to crash on the disk as shown in Figure 4.12(2).

4.4.3 Ramp Effects on the Critical Shocks

Figure 4.13 plots the critical shock as a function of shock pulse width for the three ramp models. The critical shock increases with the increase of pulse width for all three models with the same explanation as in Chapter 3. However, the positive and negative critical shocks are very close to each other in the two ramp models. That is because we consider both top and bottom ramps in the ramp models, and the disk has equal possibility to contact the top and bottom ramps during a positive or negative shock. It is also found that the deformable ramp model, which is closer to a real HDD ramp model, can resist larger critical shocks than the rigid ramp model does except when the pulse width is smaller which is explained in section 4.4.2.
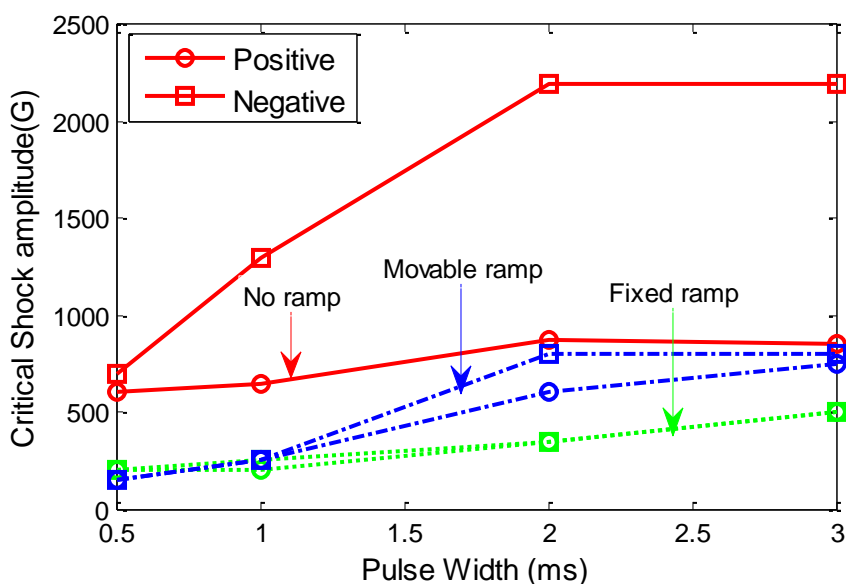
Figure 4.13 Critical shocks in three ramp models

4.5 Components' Effects on the Head Disk Interface Response Considering Ramps

In this section, we investigate the HDD components' effects on the HDI response by studying the ramp effects on the three HDD models: the disk model, the disk support model and the full model. The structural components of these three models can be found in Chapter 3. Figure 4.14 gives the disk's displacement at the slider's center position for the three models. Similar to the disk's displacement in the no-ramp models we got in Chapter 3, the disk's displacement in the disk model is much smaller than that in the other two models. Moreover, the disk-ramp contact force in the disk model is also much smaller than in the other two models as shown in Figure 4.15. There is a small difference between the disk responses of the disk support model and the full model due to the disk-ramp contact forces discrepancy shown in Figure 4.15(2) and Figure 4.15(3). The disk contacts with the top ramp in both models during the shock period (0.5~2.5 ms), while it contacts with both top and bottom ramps only in the full model after the shock because of a larger disk-ramp contact force and a more flexible structure in the full model.

Figure 4.16 presents the minimum clearance of the three models. It shows that, in all three models, the suspension's high bending modes are excited. The minimum clearance in the disk model indicates that the slider is far from contacting the disk; while in the other two models the slider barely escapes from crash.
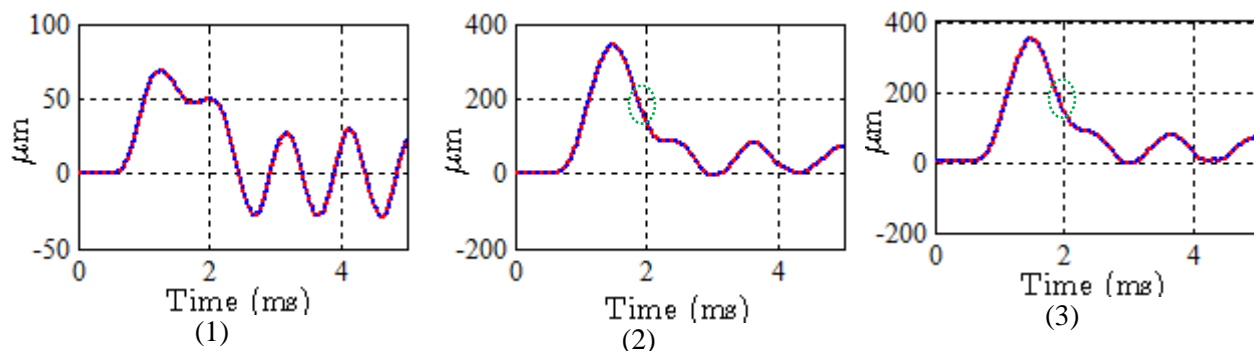
Figure 4.14 Disk absolute displacement at slider center position: (1) disk model; (2) disk support model; (3) full model.
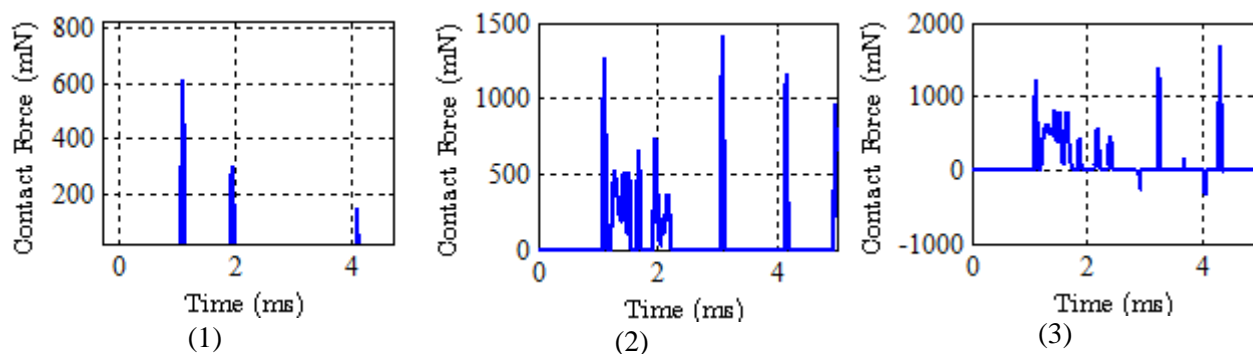
Figure 4.15 Disk-ramp contact force: (1) disk model; (2) disk support model; (3) full model.
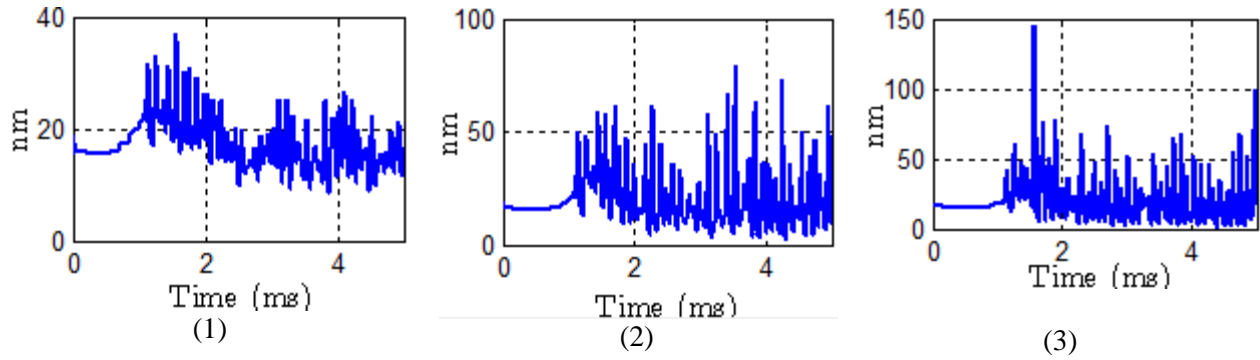
Figure 4.16 Minimum clearance: (1) disk model; (2) disk support model; (3) full model.
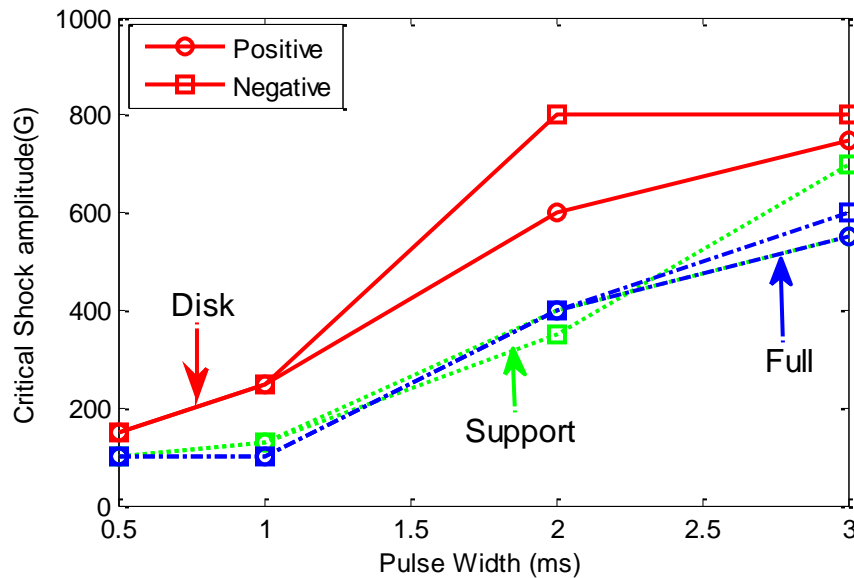
Figure 4.17 Critical shocks in three HDD models

Figure 4.17 shows the critical shocks for the three HDD models. As in the former analysis of the critical shocks, they increase with the increase of pulse width for all three models. The positive and negative critical shocks are very close for the disk support model and the full model because they have similar HDI responses during the shock. We also find that the critical shocks of the full HDD model, which is closest to the real HDD ramp model, has an almost constant offset from that of the disk model. This conclusion is the same as that obtained when the ramp model is not included.

4.6 Conclusion

The deformable ramp constraint has been implemented to the disk op-shock model. The structural and HDI responses are studied in comparison with the previously developed disk op-shock model with a rigid ramp. The slider can more easily crash on the disk in the rigid ramp model when the HDD is subject to a shock with longer pulse width. When experiencing a shock

with short pulse width, the disks and ramps residual vibrations can cause severe disk-ramp contacts or even air bearing instabilities in the deformable ramp case.

The deformable ramp model is also implemented with the disk support model and the full model. Similar to the no-ramp models investigated in the previous chapter, there is also an almost constant offset of critical shocks between the disk model and the full model if the ramp effects are considered.

Chapter 5 Numerical Solution of a Slider's Flying Attitude for Bit Patterned Media Disk

5.1 Introduction

The hard disk drive industry is continuously trying to achieve higher data storage densities and higher reliability. However, continuous increase of the areal density faces the challenge of thermal stability of recorded data. The proposal of the BPM disks is one of the promising methods to overcome this problem since in patterned media an individual recorded bit is stored in distinct magnetic islands. However, the BPM can change the topography of the disk surface and thus have an effect on the flying characteristics of the air bearing sliders. So achieving a stable flying attitude at the HDI becomes one of the main considerations for BPM.

For 1 Tbit/in^2 density, the pattern wavelength is estimated to be 25 nm with a feature size of 18 nm [56]. These sizes are much smaller than the air bearing slider's dimension. Several numerical techniques had been proposed to solve the slider's flying attitude on surfaces with regularly spaced surface features. Mitsuya et al. [57] introduced an Averaging method to simulate hydrodynamic lubrication of surfaces with two dimensional isotropic or anisotropic roughnesses. Later Mitsuya et al. [58] derived a simplified averaging Reynolds equation, involving flow factors resulting from Boltzmann molecular free flow, and applied this method to the moving roughness. Jai et al. [59] used a Homogenization method based on a double-scale approach to solve the hard disk problem with a rough slider and a rough disk. Later the Homogenization method was extended to the transient Reynolds equation derived in [60].

A number of researchers have worked on the flying characteristics of the air bearing slider over a BPM disk. Gupta et al. [61] applied the Homogenization method to simulate the static problem of the slider flying over a BPM disk with and without considering the effect of intermolecular forces, which occur at sub 5nm spacing. The relationships between the flying height, pitch, roll, stiffness and bit pattern parameters were investigated in this paper. Li et al. [62] investigated the flying characteristics of femto sliders (0.85mm×0.7mm×0.23mm) over the BPM disks using a direct simulation. This paper showed that a mesh size to bit diameter ratio smaller than 1:6 was required to guarantee a sufficiently high resolution of the air bearing pressure. To reduce the numerical complexity of the direct method, Murthy et al. [63] transferred the pattern from the disk surface to the slider surface and limited the region of the pattern to the center trailing pad of the slider. All the researches above showed the effect of the pattern height and pattern area ratio on the slider's flying height. However, these researches were all carried out for steady conditions. Myo et al. [64] used the direct Monte Carlo method to study the air bearing characteristics on the BPM disks. They found that the bearing forces are reduced with the increase of the bit pattern depth or the total recess AR. Knigge et al. [65] performed experiments on a disk with a flat zone and a patterned zone. They found similar results for the relationship between the flying height change and the pattern parameters. Nevertheless, because of the technical challenge of the BPM manufacture, experimental work is very limited.

In this study, we apply three methods (the Homogenization, the Taylor expansion Homogenization method and the Averaging method) applied in [66] to investigate the slider's dynamic flying attitude over a BPM disk. After the comparison of the computation times and

accuracy, it is found that the Taylor expansion Homogenization method is preferable to the other two. An empirical relation of a slider's flying height loss and bit pattern parameters (pattern height and pattern recession area ratio) is also verified using the Taylor expansion Homogenization method.

5.2 Modeling Techniques

The BPM is modeled as uniformly distributed cylinders on a flat disk as show in Figure 5.1 with the bit pattern parameters shown in Figure 5.2, in which h is the pattern height; p is the wavelength, and d is the diameter. So the area of one bit island is $\pi d^2/4$.
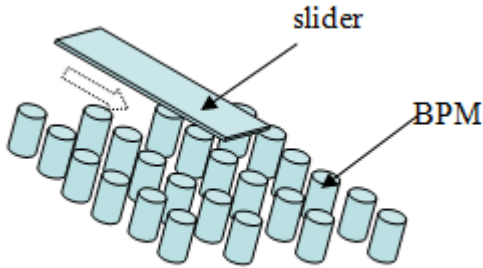
Figure 5.1 Model of BPM   Figure 5.2 Parameters of BPM
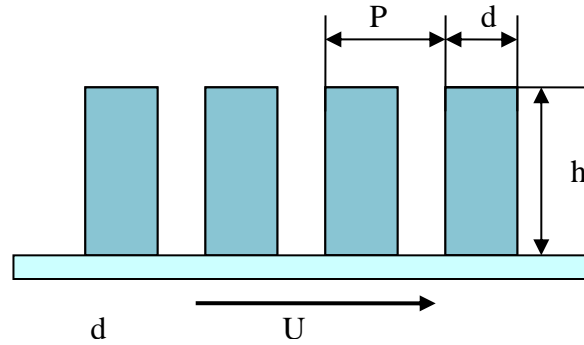
5.2.1 The Air Bearing Model

The governing equation for the gas lubrication between a slider and a disk is the generalized Reynolds equation:

$$\nabla \cdot (QPH^3 \nabla P) - \nabla \cdot \left(HP\underline{\Lambda} \right) = \sigma \frac{\partial (PH)}{\partial T} . \tag{5.1}$$

The meaning of Q, P, H, $\underline{\Lambda}$, σ and T can be found in chapter 2.

We assume the steady head-to-disk spacing on an un-patterned disk is $H_0(\underline{X}, T)$ and introduce two rapid variables $\underline{y} = \frac{\underline{X}}{\varepsilon}$ and $\tau = \frac{T}{\varepsilon}$, where ε is the pattern wavelength non-dimensionalized by the slider's length. Then the spacing can be rewritten as:

$$H \left(\underline{X}, T, \underline{y}, \tau \right) = H_0(\underline{X}, T) - H^D \left(\underline{y} - \tau \underline{e_U} \right), \tag{5.2}$$

where H^D is an elevation of the disk surface from a reference surface. $\underline{e_U}$ is the unit vector in the disk velocity ($\underline{U}$) direction. The introduction of the rapid variables requires a mesh size substantially smaller than the pattern feature size to solve Eqn. (5.1) directly. Obviously it is extraordinarily time consuming for the computation. Since the Averaging and Homogenization methods can be used to solve the roughness problem, and the bit pattern can be regarded as a

kind of uniform roughness, we prefer to use the Averaging and Homogenization methods to solve the BPM problem.

5.2.1.1 Averaging Method

For a moving disk, the averaging Reynolds equation ([57, 58]) is obtained as follows:

$$\nabla \cdot \left(QP\widetilde{H^3}\nabla P - \widetilde{H}P\underline{\Delta} \right) = \sigma \frac{\partial \overline{(PH)}}{\partial H}, \tag{5.3}$$

where

$$\widetilde{H^3} = \alpha_P \overline{H^3} + (1 - \alpha_P)\overline{\overline{H^3}} \tag{5.4}$$

and

$$\widetilde{H} = \alpha_S \overline{H} + (1 - \alpha_S)\overline{\overline{H}} + 2\beta(1 - \alpha_S)(\overline{H} - \overline{\overline{H}}). \tag{5.5}$$

where $\overline{H}$ is the arithmetic average spacing defined as $\overline{H} = \iint HdXdY/dXdY$ and $\overline{\overline{H}}$ is the harmonic average spacing which can be calculated by: $\overline{\overline{H}} = \overline{H^{-2}}/\overline{H^{-3}}$ and $\overline{\overline{H^3}} = 1/\overline{H^{-3}}$. As the bit pattern can be regarded as an isotropic projection model, the mixing rations α_P and α_S are chosen to be the same and are given in the Table 5.1[57]. They are equal to 1 for a longitudinal pattern and equal to 0 for a transverse pattern. β=1 is for the moving disk, and β=0 is for the

Table 5.1 Mixing ratios in the averaging method [57]

Pattern Height (PH)	Mixing ration (α)
0.01	0.5050
0.02	0.5082
0.05	0.5173
0.08	0.5257
0.1	0.5309
0.2	0.5533
0.5	0.5939
0.8	0.6135
1	0.6210
2	0.6356
5	0.6411
8	0.6416
10	0.6417

static disk. The advantage of the averaging method is that it can significantly save the computing cost because the node number for an averaging method can be as few as 200×200 while for the direct method it is around 500,000×500,000.

5.2.1.2 Homogenization Method

Another method, which can reduce the computational cost, is the Homogenization method. The Homogenization method introduced in [60] includes a global problem and a local problem. The global problem is very similar to the generalized Reynolds equation except that it involves two homogenization coefficient matrixes. The local problem is a set of partial differential equations used to calculate those coefficients.

The derivation of the homogenization problem required the following replacements to Eqn. (5.1) because of the introduction of two rapid variables and the identification of the terms (ε^n) on the left- and right- hand sides; then multiplication of the same power of ε:

$$\frac{\partial}{\partial T} \to \frac{\partial}{\partial T} + \frac{1}{\varepsilon}\frac{\partial}{\partial \tau} \ , \tag{5.6}$$

$$\nabla_X \to \nabla_X + \frac{1}{\varepsilon}\nabla_y \ , \tag{5.7}$$

$$P\left(\underline{X}, T, \underline{y}, \tau\right) \to P_0\left(\underline{X}, T, \underline{y}, \tau\right) + \varepsilon P_1\left(\underline{X}, T, \underline{y}, \tau\right) + \varepsilon^2 P_2\left(\underline{X}, T, \underline{y}, \tau\right) + \cdots . \tag{5.8}$$

After some algebraic calculation, we can get a so-called "homogenization problem", which allows us to determine P_0 and P_1. By introducing the two local problems:

$$-\nabla_y \cdot \left(Q P_0 H^3 \nabla_y \omega_i\right) = \nabla_y \cdot \left(Q P_0 H^3 \underline{e_i}\right), \tag{5.9}$$

and

$$-\nabla_y \cdot \left(Q P_0 H^3 \nabla_y \chi_i\right) = \nabla_y \cdot \left((H_0 - (1 - \frac{\sigma}{\Lambda})H^D)\underline{e_i}\right), \tag{5.10}$$

the homogenization problem can be decoupled, such that

$$P_1 = \nabla_X P_0 \cdot \underline{\omega} - P_0\underline{\Lambda} \cdot \underline{\chi} \ , \tag{5.11}$$

and P_0 can be calculated by the homogenization global problem:

$$\nabla_x \cdot [A^* \nabla_x P_0] - \nabla_x \cdot [P_0\Theta^*\underline{\Lambda}] = \sigma\frac{\partial(P_0\bar{H})}{\partial T} \ , \tag{5.12}$$

where the homogenization coefficients are:

$$A^* = \begin{bmatrix} \overline{Q P H^3(1 + \frac{\partial \omega_1}{\partial y_1})} & \overline{Q P H^3(1 + \frac{\partial \omega_2}{\partial y_1})} \\ \overline{Q P H^3(1 + \frac{\partial \omega_1}{\partial y_2})} & \overline{Q P H^3(1 + \frac{\partial \omega_2}{\partial y_2})} \end{bmatrix}, \tag{5.13}$$

and

$$\Theta^* = \begin{bmatrix} \overline{H} + \overline{\overline{QPH^3 \frac{\partial \chi_1}{\partial y_1}}} & \overline{\overline{QPH^3 \frac{\partial \chi_2}{\partial y_1}}} \\ \overline{\overline{QPH^3 \frac{\partial \chi_1}{\partial y_2}}} & \overline{H} + \overline{\overline{QPH^3 \frac{\partial \chi_2}{\partial y_2}}} \end{bmatrix}. \tag{5.14}$$

Here the double over-bars imply average with respect to the rapid variables $\underline{y}$ and τ; the single over-bar is the average with respect to $\underline{y}$. The functions ω_1, ω_2, χ_1 and χ_2 are 1-period solutions of the local problems solved in Eqn. (5.9) and (5.10).

For the steady state, the global and local problems can be reduced to the following equations.

Global problem:

$$\nabla_x \cdot [A^* \nabla_x P_0] - \nabla_x \cdot \left[P_0 \Theta^* \underline{\Delta} \right] = 0 , \tag{5.15}$$

where A^* and Θ^* are similar to Eqn. (5.13) and (5.14), except that there is no time integration for the matrix components.

Local problem:

$$-\nabla_y \cdot \left(Q P_0 H^3 \nabla_y \omega_i \right) = \nabla_y \cdot \left(Q P_0 H^3 \underline{e_i} \right), \tag{5.16}$$

and

$$-\nabla_y \cdot \left(Q P_0 H^3 \nabla_y \chi_i \right) = \nabla_y \cdot \left(H \underline{e_i} \right). \tag{5.17}$$

This method requires no more than 200×200 nodes to solve the Homogenization Reynolds equation (5.12) and (5.15), but it is still computationally more expensive than the averaging method because the local problems need to be solved on each of the 200×200 nodes. Nevertheless, the local problems are only solved on a unit cell which contains one bit pattern feature, 10×10 nodes are more than sufficient. Thus, the total number of nodes needed is around (200×200)·((10×10) ·2).

5.2.1.3 Taylor Expansion Homogenization Method

The Homogenization method can produce quite good results as discussed in [67], but it is also somewhat computationally expensive, especially for the dynamic cases. Buscaglia and Jai [68] proposed a new approach to reduce its computational cost by approximating the homogenization coefficients by a Taylor series expansion. We call this method the Taylor expansion Homogenization method. In this method the coefficients A^* in Eqn. (5.13) and Θ^* in Eqn. (5.14) are replaced by their Taylor expansions up to order n=4, and this approximation was shown to be sufficiently accurate. The Taylor expansions are as follows:

$$T_{A_n^*} = A^*(\alpha^0) + \sum_{i=1}^{n} \frac{1}{i!} \left((\alpha_1 - \alpha_1^0) \frac{\partial}{\partial \alpha_1} + (\alpha_2 - \alpha_2^0) \frac{\partial}{\partial \alpha_2} \right)^i A^*(\alpha^0) \tag{5.18}$$

$$T_{\Theta_n^*} = \Theta^*(\alpha^0) + \sum_{i=1}^{n}\frac{1}{i!}\left((\alpha_1 - \alpha_1^0)\frac{\partial}{\partial\alpha_1} + (\alpha_2 - \alpha_2^0)\frac{\partial}{\partial\alpha_2}\right)^i\Theta^*(\alpha^0) \tag{5.19}$$

Here the variable $\alpha = (\alpha_1, \alpha_2) = (H, P)$.

The complete Homogenization method needs to solve the local problems at every node while the Taylor expansion Homogenization method only needs to solve one set or several sets of local problems. The homogenization coefficients at the other nodes can be approximated by the Taylor expansion around the coefficients which have already been calculated by solving the local problem directly. So the total number of nodes needed in the Taylor expansion Homogenization method is about 200×200+2·n·10×10, where n is usually less than 10.

5.2.2 The Slider Model

The slider model is much simpler than the one shown in Chapter 2. Here the slider is modeled as a 3-DOF rigid body and the equation of motion can be expressed as:

$$m\frac{d^2z}{dt^2} + c_z\frac{dz}{dt} + k_zz = f_z(t) + \iint_A (p - p_s)dA, \tag{5.20}$$

$$I_\theta\frac{d^2\theta}{dt^2} + c_\theta\frac{d\theta}{dt} + k_\theta\theta = f_\theta(t) + \iint_A (p - p_s)xdA, \tag{5.21}$$

$$I_\beta\frac{d^2\beta}{dt^2} + c_\beta\frac{d\beta}{dt} + k_\beta\beta = f_\beta(t) + \iint_A (p - p_s)ydA. \tag{5.22}$$

In Eqns. (5.20)-(5.22), m, I_θ and I_β are the mass and inertia moments of the slider; z, ɵ and β are the slider's vertical displacement (from the steady state) at the slider's center, and its pitch and roll; $k_z, k_\theta, k_\beta, c_z, c_\theta$ and c_β are the stiffness and damping coefficients of the slider. $f_z(t)$, $f_\theta(t)$ and $f_\beta(t)$ are external excitation forces. p and p_s are pressure profiles in the vibration state and steady state.

5.3 Slider's Flying Attitude over a Bit Patterned Media Disk

The ABS designs of the femto-sized sliders used in this study are shown in Figure 5.3. We call the minimum flying height of a slider flying over an un-patterned disk as MFH_0. The MFH_0 of is about 11.5 nm for slider I while it is about 2 nm for slider II. In the following study, we first use a direct method to check the accuracy of the Homogenization method, and then investigate the sliders' flying heights using the above three methods in order to determine a most economical method.
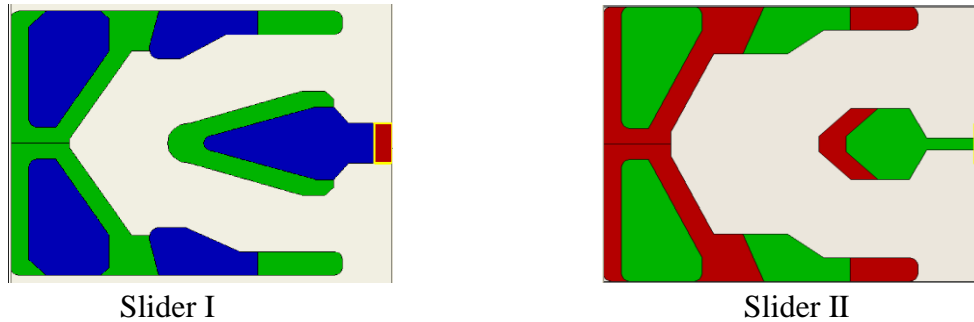
Slider I　　　　　　　　　　　　　　Slider II

Figure 5.3 Sliders used in this study

5.3.1 A Direct Calculation for Checking the Homogenization Method

We first use the CML Dynamic Simulator [15] to check the accuracy of the Homogenization method by simulating the flying height of slider I when it flyies over a BPM disk. In this direct method, the bit patterns are defined as cylinder-formed waviness. Because of the computing limitation, the pattern sizes in this direct simulation are chosen to be on the order of μm. While using the Homogenization method, the pattern sizes are chosen to be on the order of tens of nm.

Figure 5.4 shows a comparison of the simulated steady flying height using the direct method (with pattern wavelength 10 μm) and the Homogenization method. In this figure, the abscissa shows the BPM AR (area ratio), which is the area covered by the bit pattern divided by the total area, and PH represents bit pattern height non-dimensionalized by MFH_0. From this figure it can be seen that the change tendency of the minimum spacing with the change of the pattern height and the pattern AR is almost the same for these two methods: the minimum spacing increases with an increase of the bit pattern AR and decreases with an increase of the bit pattern height. It can be explained thusly: when the bit pattern AR increases, the disk is covered more by the raised bit pattern, so the pressure rises and the bearing force becomes larger than the suspension load. In order to balance the suspension load, the spacing should increase simultaneously. On the other hand, when the bit pattern height increases, if the slider's minimum flying height is MFH_0 from the top of the patterned disk, the spacing between the slider and the patterned disk's recessed parts increases, therefore the pressure decreases over these recessed regions. This leads to the spacing between the slider and the pattern's top surface decrease in order to regain balance. These results are very similar to what was obtained in [61] for the static cases. However, as seen from the figure, an offset of spacing is observed between the results of the direct method and the Homogenization method. The simulated flying height using the direct method is slightly higher than the simulated flying height using the Homogenization method.

Since the direct method uses a pattern size much larger than the pattern size used in the Homogenization method, we also investigate the effect of the pattern size on the simulated steady flying height, using the direct method in order to study the pattern size effects on the slider's flying height and the results are shown in Figure 5.5. In this simulation we chose the case with PH=0.75 and pattern AR=0.25. We selected three different pattern sizes: 100 μm, 10 μm and 5 μm respectively. The right figure of Figure 5.5 is a partial zoom-in of the left figure. The simulation results show that the average minimum spacing decreases as the pattern size decreases. So when the pattern size used in the direct method is reduced (approaching the real

pattern size), the calculated flying height moves in the direction of the flying height calculated by the Homogenization method. Thus we can say, with some assurance, that the direct method guarantees the accuracy of the Homogenization method.
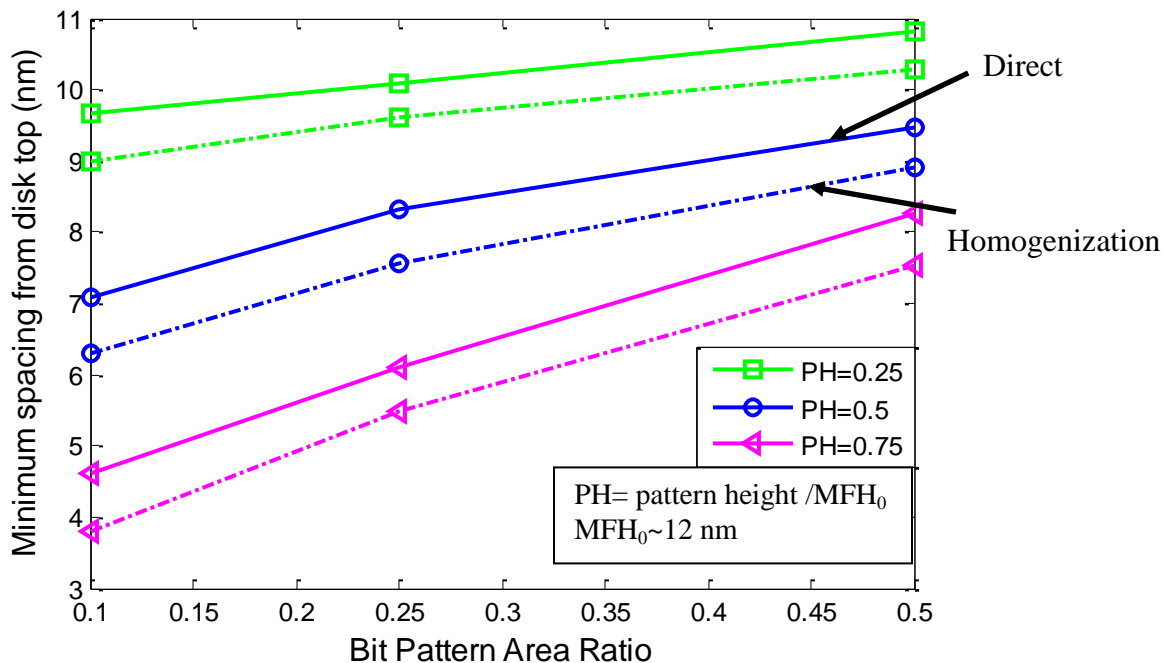
Figure 5.4 Comparison of steady flying height for direct method and Homogenization method
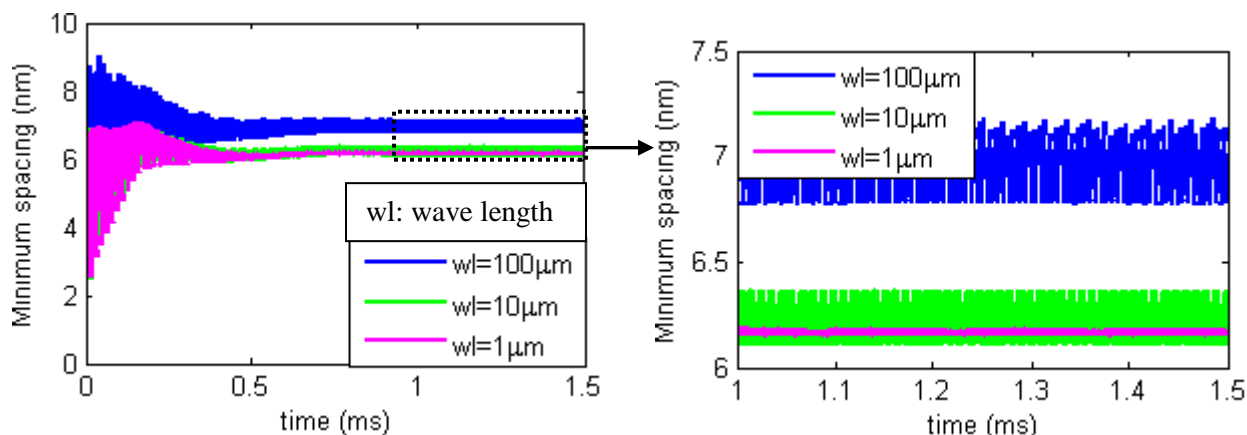
Figure 5.5 Pattern size effects on simulated flying height for direct method

5.3.2 An Economical Accurate Method

Figure 5.6 shows a comparison of the minimum flying height measured from the pattern media top surface using the three methods for slider I: Averaging, Taylor expansion Homogenization and complete Homogenization method. The complete Homogenization method is the Homogenization method introduced in section 5.2, and we call it the complete Homogenization method to differentiate it from the Taylor expansion Homogenization method.

Here, the complete Homogenization method is taken as the reference method, since it produces results very close to the direct simulation method, which has been shown in section 5.3.1 and also in [66]. The results show that, for the small bit pattern heights (PH=0.1,0.25), both the Averaging and Taylor expansion Homogenization methods give essentially the same change tendency in the minimum flying height to bit pattern area ratio and bit pattern height which are the same as we got in section 5.3.1. However, as the pattern heights increase, these two methods begin to produce some differences. In order to determine which method is more accurate, the slider's flying attitudes with two higher pattern heights (0.5, 0.75) are computed again using the complete Homogenization method. It is found that the minimum flying height calculated by the Taylor expansion Homogenization method is almost the same as that from the complete Homogenization method. Therefore, we can use either the Averaging method or Taylor expansion Homogenization method for smaller pattern heights (pattern heights less than a quarter of the minimum flying height), but for higher pattern heights it is better to use the Taylor expansion Homogenization method.

Table 5.2 gives the number of nodes and computation time for the three methods. The computation time for the Taylor expansion Homogenization method is almost on the same order as the Averaging method, and both of them are much faster than the complete Homogenization method. As the Taylor expansion Homogenization method is accurate for all ranges of PH, it is chosen as the most economical accurate method among these three and is used in the following study.
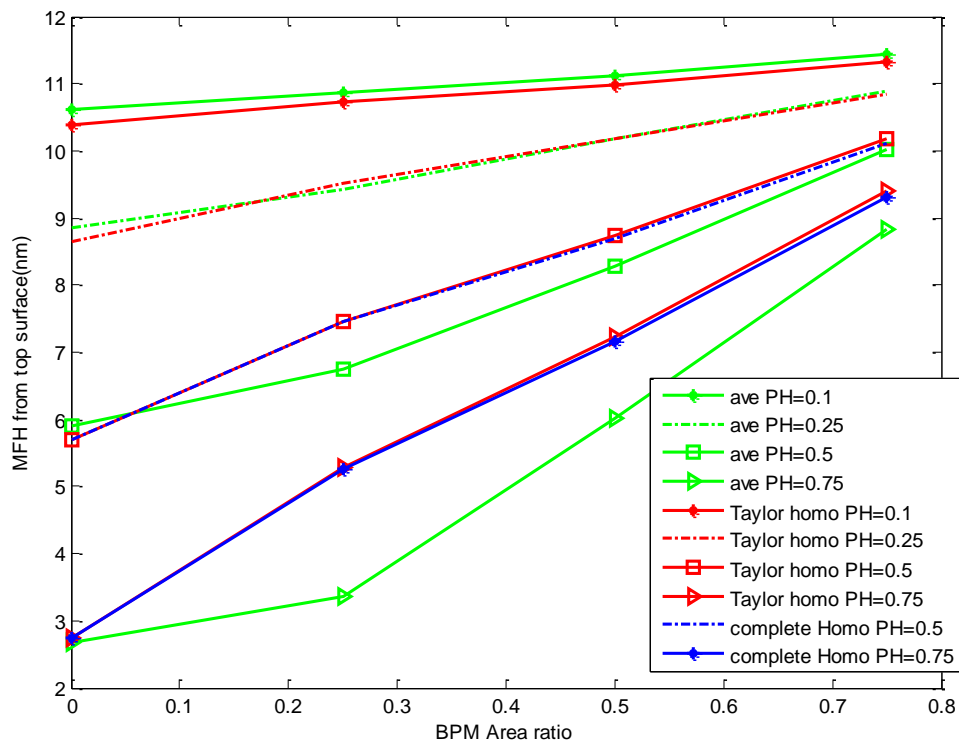
Figure 5.6 Comparison of minimum flying height from top surface of the pattern media using three methods

Table 5.2 Computing cost for the three methods

Modeling Techniques	Number of nodes needed	Computation time
Direct	500,000×500,000	N/A
Averaging	200×200	~3 hours
Complete Homogenization	(200×200)·((10×10) ·2)	~3+12=15 hours
Taylor expansion Homogenization	200×200+ 2·n·10×10 (n<10)	~3+0.5=3.5 hours

5.3.3 An Empirical Equation for the Slider's Flying Height over BPM Disk

First the empirical equation of the flying height loss as a function of the bit pattern height and the recess AR in the static solutions are verified (the static simulation gives almost the same result as the dynamics simulation, but it is much faster). Figure 5.7 shows the flying height loss with a change of the bit pattern height for different recess ARs; the number beside the line is the slope of that line. It indicates that the flying height loss is linearly proportional to the bit pattern height for every recess AR, and the slope of each line is close to, but not exactly the same as, the recess AR represented by that line. Figure 5.8 shows the flying height loss with a change of the pattern recess AR for different pattern heights. From this figure some nonlinearity is observed, especially for higher pattern heights. This nonlinear effect was also obtained by a direct simulation [63], and it was explained as: a change of the bit pattern diameter leads to a change of the pattern profile not only in the slider's width direction but also in the slider's length direction so that the side flow is prevalent in this case. However, for small pattern heights, the flying height change can still be considered as a linear function of the recess AR. Moreover, the relationship between the flying height loss and the dimensional bit pattern height is almost independent of the sliders' designs as we can see the two different sliders give almost the same flying height loss in Figure 5.9. Thus, we conclude that for the small bit pattern height (such as for a more planarized bit pattern media), the empirical relationship proposed by Knigge et al. [65] is still reliable:

$$\Delta\text{FH} = h \cdot \frac{A_{recess}}{A_{total}}, \tag{5.23}$$

where h is the dimensional pattern height (see Figure 5.2), and $A_{recess}/A_{total} = 1 - \pi d^2/(4p^2)$. However, for high pattern heights, especially higher than MFH_0, the equation above is not very accurate. It is required to simulate more cases to obtain a quadratic curve if needed.
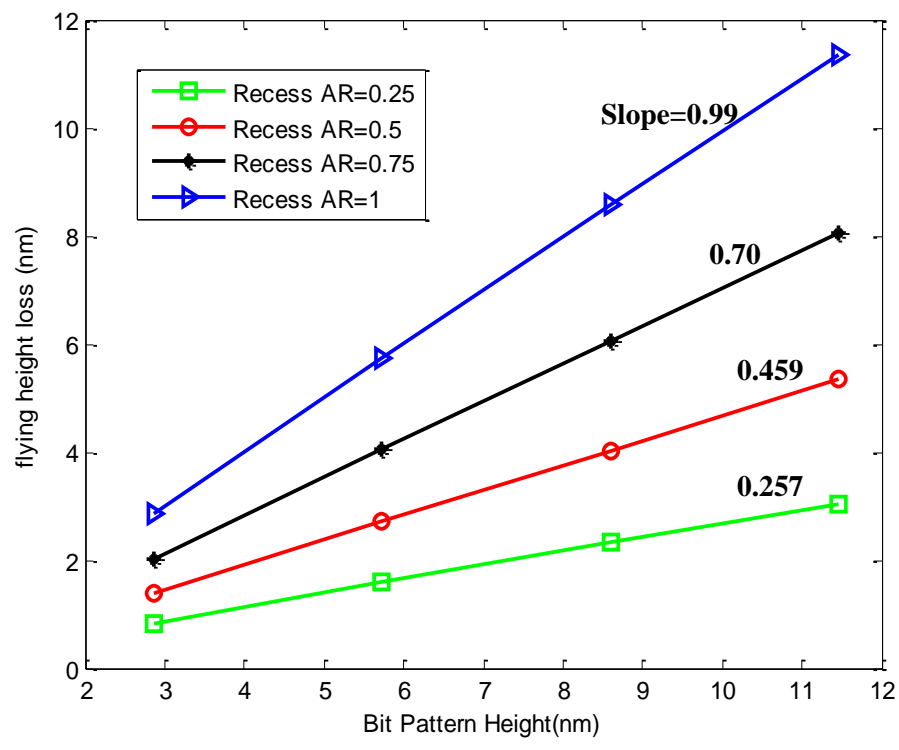
Figure 5.7 Flying height loss with bit pattern height for different recess area ratios
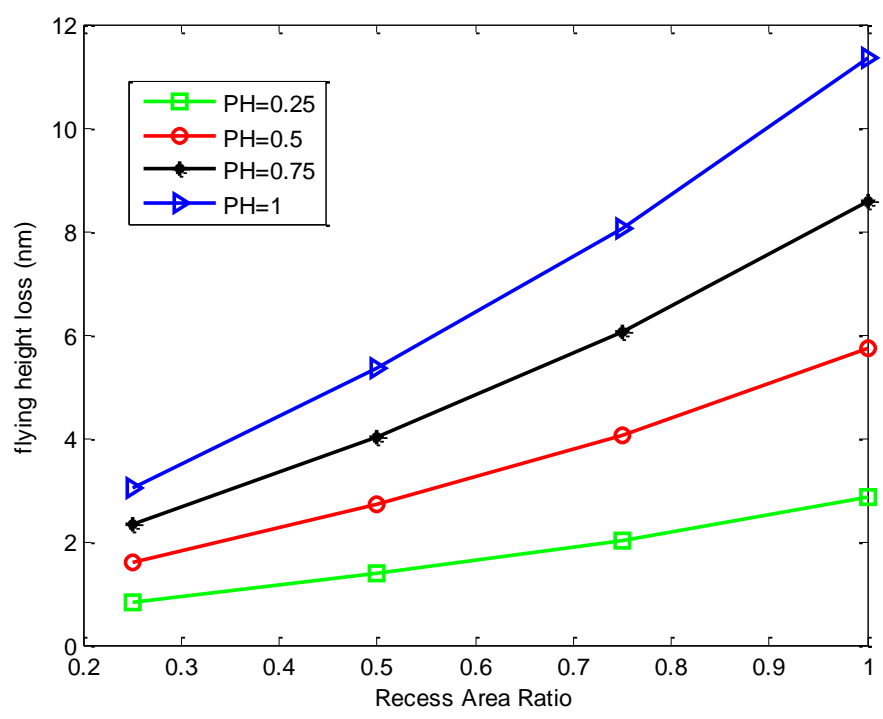
Figure 5.8 Flying height loss with recess area ratio for different bit pattern heights
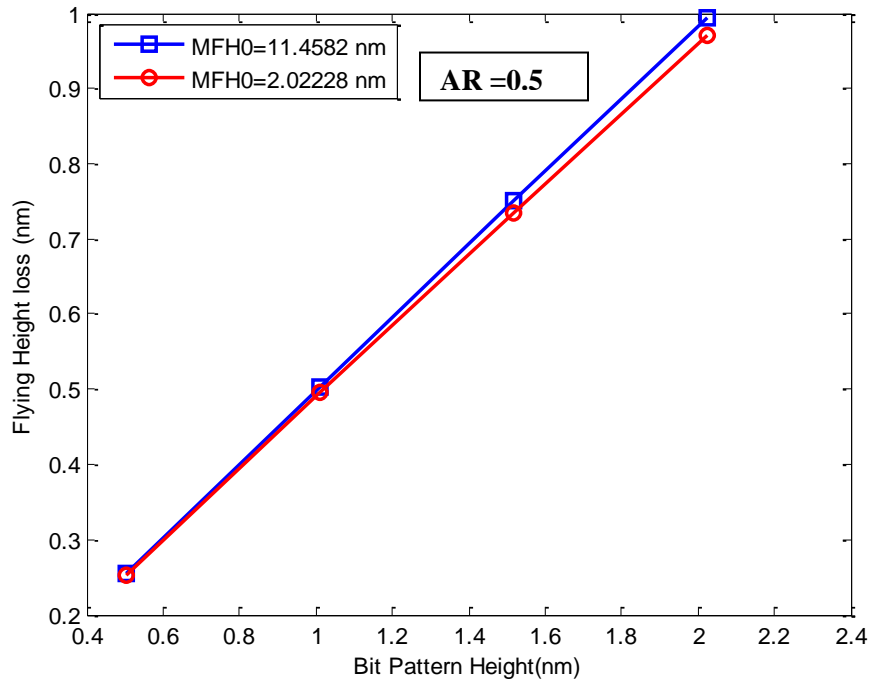
Figure 5.9 Flying height loss with bit pattern height for slider I and slider II

5.4 Conclusion

In this chapter we investigated three modeling techniques to simulate the time-dependent HDI problem for BPM disks. It was found that the Taylor expansion Homogenization method is the most economical accurate method for all ranges of pattern heights while the Averaging method is only reliable for small pattern heights.

Then the Taylor expansion Homogenization method was applied to investigate the slider's flying attitude on the BPM disk. For small pattern heights, the minimum flying height loss is almost a linear function of the pattern height and AR. The experimentally observed empirical relation in [65] is verified. For larger pattern heights, we need to consider nonlinearities.

Chapter 6 Examples of Air Bearing Dynamics over BPM Disks and Servo Sectors

6.1 Introduction

The Slider's flying attitude changes during the transition between the data and servo zones, which have different patterned designs, were investigated by several researchers. Li and Bogy [69] studied a slider's dynamics on a BPM disk with different patterned types on the data and servo zones. It was found that the effects of the bit aspect ratio, which is defined as the ratio of one pattern periodical length to width, and the pattern arrangements can be ignored, and the flying characteristics during the transition between the two zones depend on the pattern height and pattern area ratio. Hanchi et al. [70] investigated the effects of discrete track pattern orientation shifts at data-servo zone transitions on the slider's flying stability, and they found that the orientation shifts between the data and the servo sectors could give rise to perturbations in flying height. The dynamic characteristics of a slider flying over various servo patterns were studied in [71]. They showed that the air-flow field was disturbed, and flying amplitude modulation during the transitions was observed.

A system identification method, applying the CML Dynamic Simulator with modal analysis, was first proposed for the analysis of the dynamic characteristics of air bearings by Zeng et al. [72]. An improved method based on [72] that employed the multiple input/multiple output orthogonal rational fractional polynomial method to estimate the modal parameters was presented by Zeng and Bogy [73]. However, little work has been done to investigate the dynamic stability and system parameters of the air bearing between sliders and BPM disks.

In this study the slider's flying height changes, during the transitions between the data and servo zones, are investigated. Then a system identification method, which involves simultaneously solving the equations of motion of the slider and the Homogenization Reynolds equation, is used to obtain the air bearing system's parameters in order to study the air bearing stability problem.

6.2 Slider's transition between different BPM types

6.2.1 BPM types that produce different flying heights

We first investigate the slider's dynamic flying attitude at transitions over different pattern types, as might be associated with data and servo zones. The slider we used in this study is the same as the slider I in chapter 5. Figure 6.1 is a schematic of a slider flying at the transition between a data zone and a servo zone. We assume the circumferential wedge of each servo zone is about 2 degrees. So the servo circumferential length is about 1.1 mm at the computed radius and the femto slider's length is 0.85 mm.
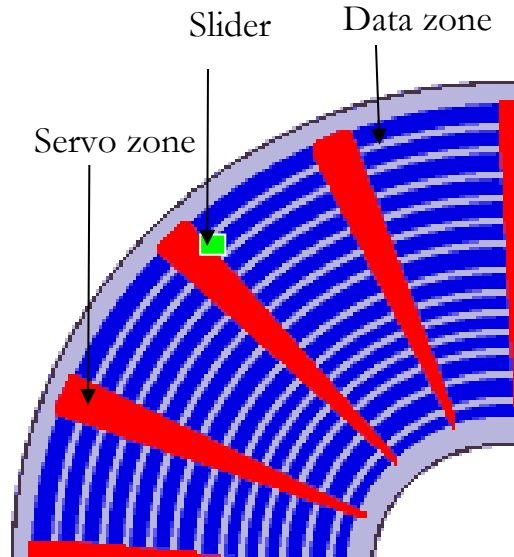
Figure 6.1 A slider flying at transition between data zone and servo zone

Figure 6.2 shows the minimum flying height change when the slider experiences a transition between two different pattern types. Here, we assume the first pattern type (PH=0.25, AR=0.25) covers 10 times more area than the second pattern type (PH=0.25, AR=0.5). From the figure, we see that the minimum flying height increases and decreases periodically during the transitions. The minimum flying height on the first bit pattern (data zone) is almost the same as the flying height obtained in Figure 5.6 for the same bit pattern type, but the minimum flying height on the second bit pattern (servo zone) is slightly smaller than the flying height obtained in Figure 5.6. That is because the circumferential length of the second bit pattern is not long enough for the slider to obtain a steady flying condition.
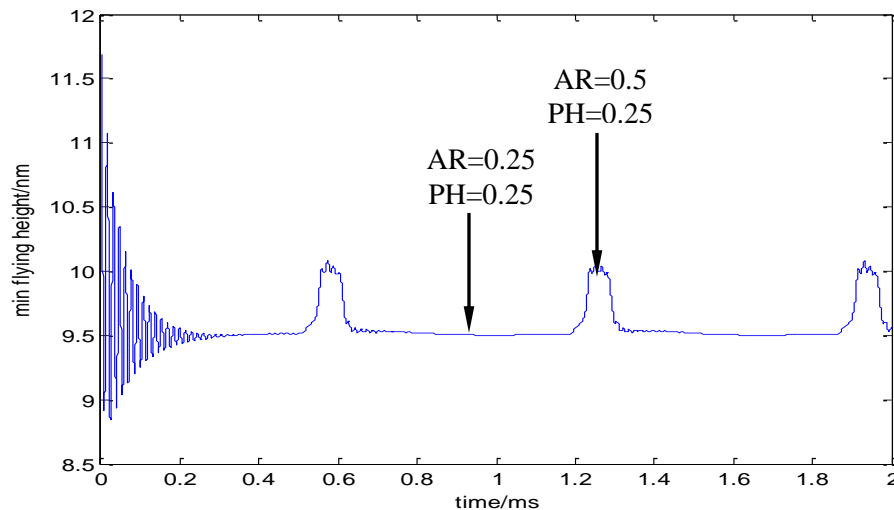
Figure 6.2 Minimum flying height when the slider transition between different pattern types (same pattern height but different area ratio)
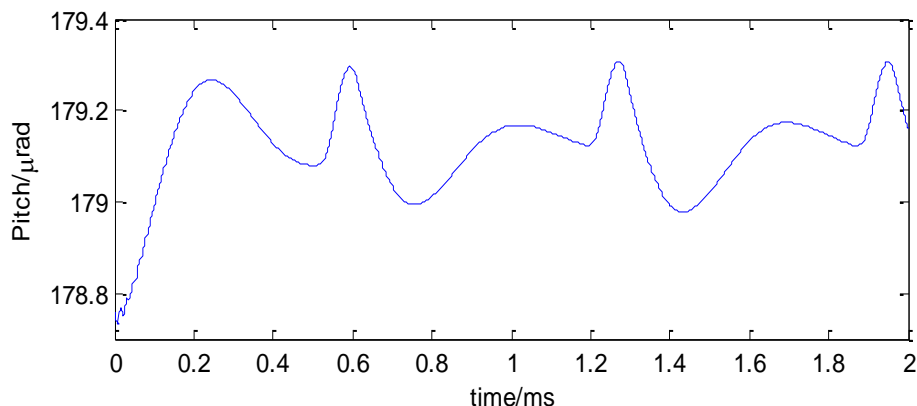
Figure 6.3 The pitch change when the slider transition between different pattern types
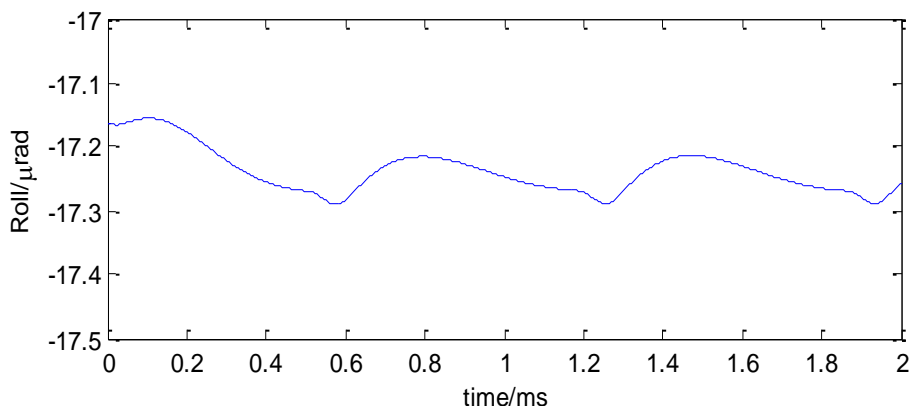
Figure 6.4 The roll change when the slider transition between different pattern types

At the time the slider begins to fly from the first bit pattern to the second, one part of the slider is on the first bit pattern and the other part is on the second bit pattern. This is the reason why the slider has a gradual change during the transition. After the slider has entirely transformed to the second bit pattern, it begins to seek a new steady attitude.

From Figure 6.3 and Figure 6.4, we find the pitch and roll also change periodically when the slider experiences a transition between different pattern types. The peak-peak value of pitch is around 0.3 µrad. The change of roll is even smaller, and the peak-peak value is less than 0.1 µrad. So we can ignore the transition effect on the pitch and roll.

We also investigate the slider's flying attitude on a patterned disk with a smaller servo zone. The circumferential wedge of the servo zone is 0.2 degrees (one tenth of that in the previous case), which is much closer to the real disk's servo zone size. After the simulation starts, the slider first flies on the first pattern type (data zone) until it attains a steady flying condition and then it begins to experience transitions as shown in Figure 6.5. The slider's periodic motion can also be observed for this case. During transitions, the minimum flying heights on both pattern types oscillate because the circumferential length on each zone is not long enough for the slider to obtain a steady flying height. The average minimum flying height on the data zone is very

close to the minimum flying height we got in the previous transition study, but the flying height at the servo zone is much smaller than the one we got before. When the slider flies from the data zone to the servo zone, the flying height increases since these two zones have the same pattern height but the area ratio is larger in the servo zone than it is in the data zone. Before the slider is totally flying to the servo zone, its leading edge begins to transfer to the data zone again because the circumferential length of the servo zone is smaller than the slider's length. Therefore, the minimum flying height starts to decrease after a small increase (see servo zone part in Figure 6.5), and the peak-peak value is less than 0.5 nm, which is much smaller than that in the previous case. If, in a real disk, the circumferential wedge of the servo zone is smaller than 0.2 degrees, the peak-peak value will be even smaller.
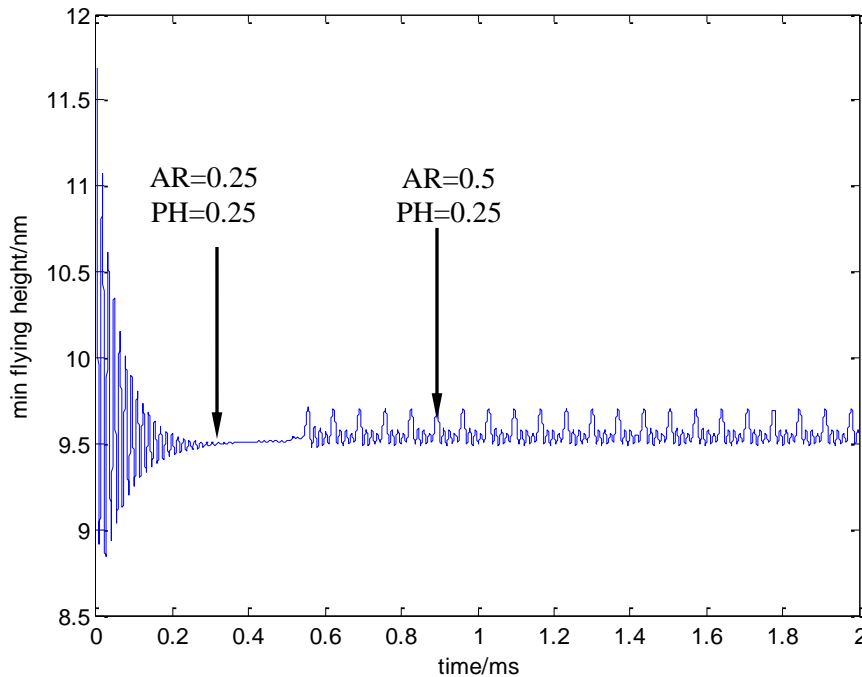
Figure 6.5 Minimum flying height when the slider transition between different pattern types (smaller servo zone)

6.2.2 BPM types that produce the same flying height

Here, we investigate the slider's flying attitude at transitions over different pattern types which can produce the same minimum flying height. Figure 6.6 shows the slider's minimum flying height using the Taylor expansion Homogenization method. The horizontal straight line is used to find two different pattern types which can produce the same minimum flying height. We choose the minimum flying height of 7.5 nm for which the corresponding pattern types are: AR=0.25, PH=0.5 and AR=0.52, PH=0.75. We also choose the circumferential wedge of the servo zone to be 0.2 degrees. Figure 6.7 shows the minimum flying height change when the slider experiences transitions between the selected two pattern types. As before, the slider flies on the first pattern type until a steady state is reached and then it starts to experience the transitions. It turns out that the slider's flying attitude has almost no change after the slider

obtains a steady condition on the first pattern type. The slider's pitch and roll, shown in Figure 6.8 and Figure 6.9, are the same as the slider's pitch and roll if it only flies on the first pattern type.
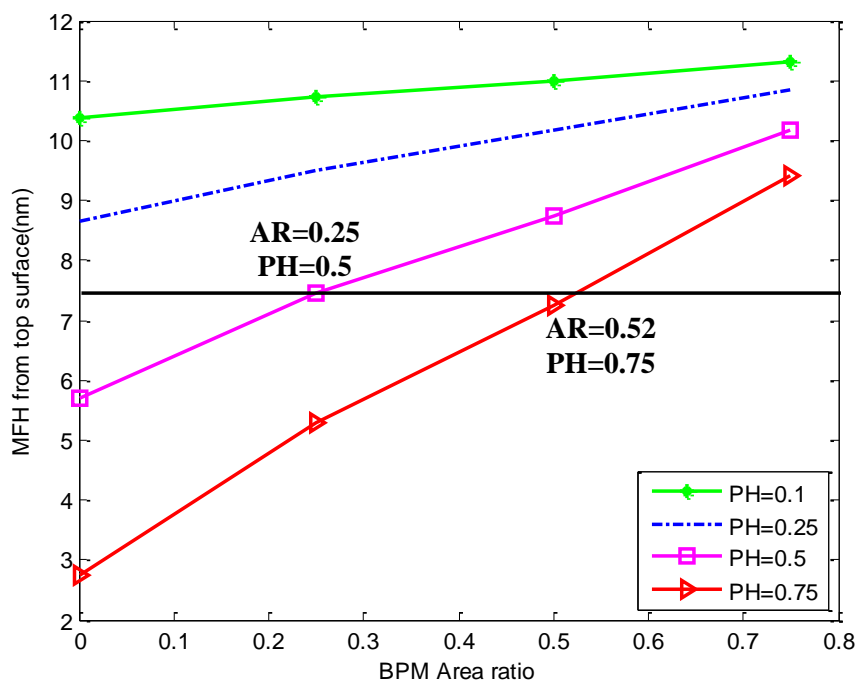
Figure 6.6 Two pattern types which can produce the same minimum flying height
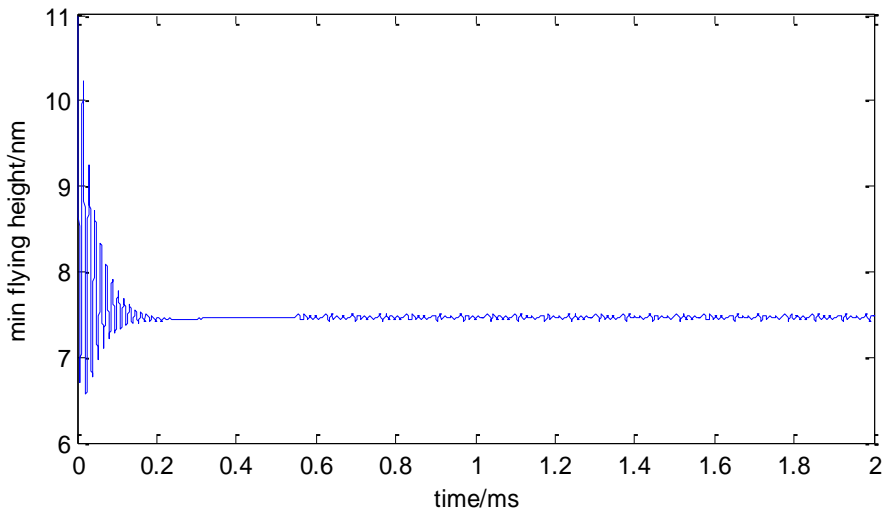
Figure 6.7 Minimum flying height when the slider transition between two pattern types which can produce the same minimum flying height
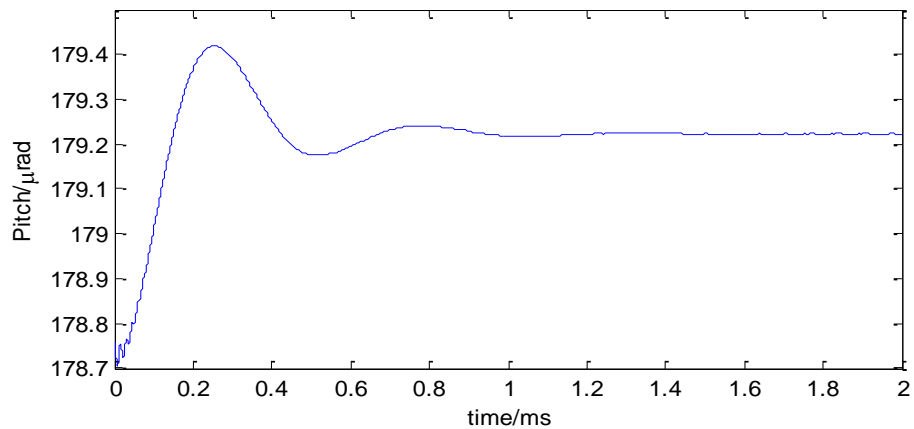
Figure 6.8 The pitch change when the slider transition between different pattern types
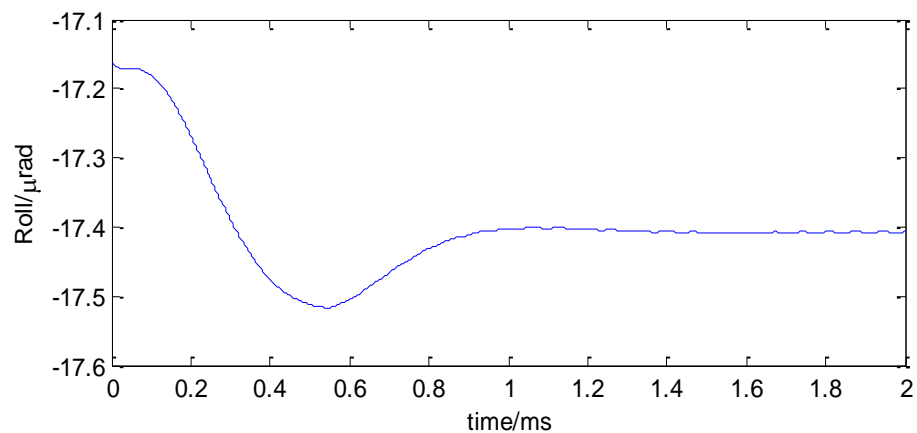
Figure 6.9 The roll change when the slider transition between different pattern types

6.3 Slider dynamic stability

In this section we investigate a slider's dynamic stability on various pattern designs [74]. The ABS design studied in this section is shown in Figure 6.10. We first use the Taylor expansion Homogenization method to obtain the slider's steady flying height on different patterned designs, the results of which are shown in Figure 6.11. This figure shows that the minimum flying height decreases with an increase of recess AR; the flying height also decreases with an increase of pattern height. So it indicates that the minimum flying height is smaller if the pattern height is higher or the recess AR is larger.
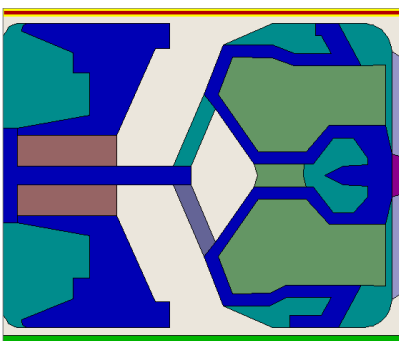
Figure 6.10 ABS design
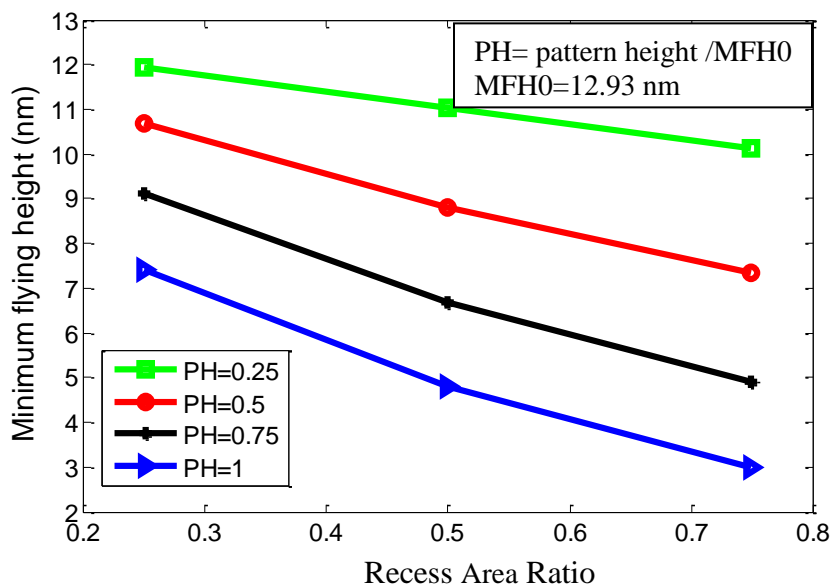
Figure 6.11 The slider's steady minimum flying height on various pattern designs

Next we use the system identification method [73] to obtain the air bearing system parameters such as stiffness, mode shape and mode frequency. In order to study the bit pattern effects on the air bearing system's parameters, we first study the case, in which the slider is flying over a smooth disk. The mode shapes and their corresponding frequencies are shown in

Figure 6.12. It shows that the first mode (numbered 1) is a pitch mode with frequency 177 kHz, and its nodal line is close to the trailing edge; the second mode is a roll mode with frequency 188 kHz with its nodal line located almost at the slider center line; the third mode is nearly a pure pitch mode with frequency 362 kHz, and its nodal lines is close to the leading edge.
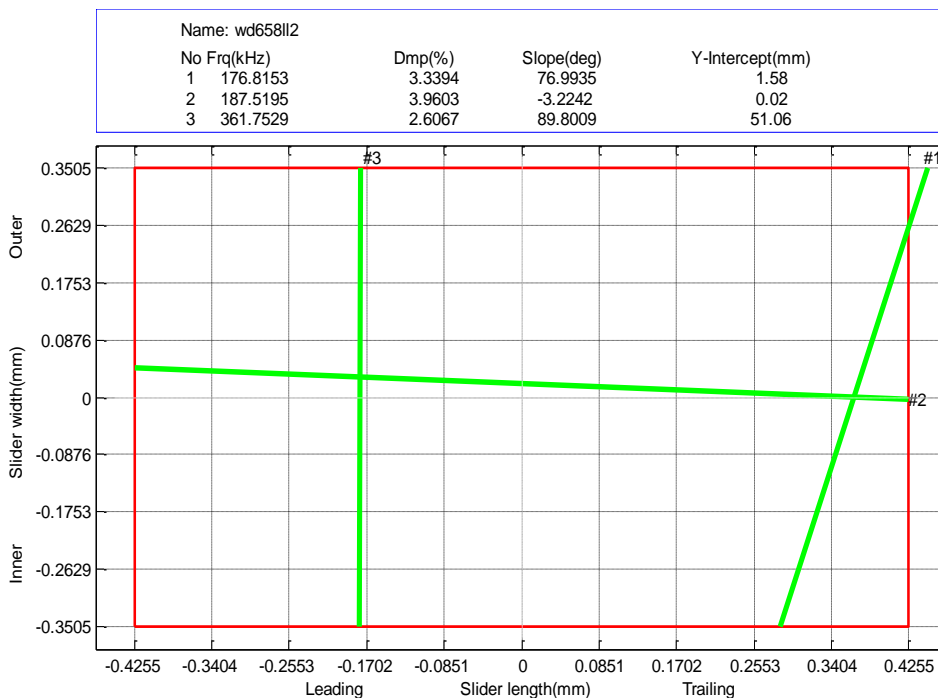
Figure 6.12 Results when the slider is flying on a smooth disk

Next we studied the frequency and stiffness changes with the changes of pattern height and pattern AR. The frequencies (kHz) of the first pitch mode are listed in Table 6.1, in which each row has different recess ARs and each column has different pattern heights. To show the results more clearly, we plot the first two rows in the left figure of Figure 6.13and plot the first column in the right figure. These results show that the first pitch mode frequency increases with an increase of recess AR, and also increases with an increase of pattern height. As shown in Figure 6.11, the minimum flying height decreases with an increase of recess AR and pattern height, and the first pitch mode nodal line is close to the trailing edge where the minimum clearance occurs. So the increase of the first pitch mode frequency can be considered as an effect of further compression of the air film. Referring back to Table 6.1, it is observed that there are three frequencies, marked by the bold font, that do not follow the frequency increasing tendency. As shown in Figure 6.14, the stiffness decreases as recess AR or pattern height increases. Moreover, continuous increase in the pattern height or recess AR leads to a negative stiffness which means that instability appears under these conditions. This indicates that a partially planarized patterned media is required in order to improve the dynamic stability of the HDI.

Table 6.1 First mode frequencies on BPM disks

Rec AR PH	0.25	0.5	0.75
0.25	177.671	178.471	179.062
0.5	178.517	179.265	179.742
0.75	179.102	179.445	**173.839**
1	179.516	**177.427**	**167.496**
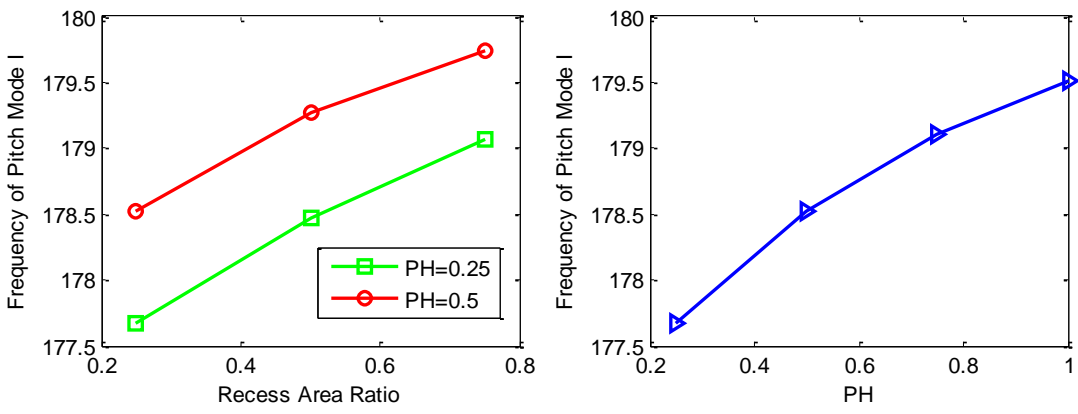
Figure 6.13 First mode frequencies on BPM disks
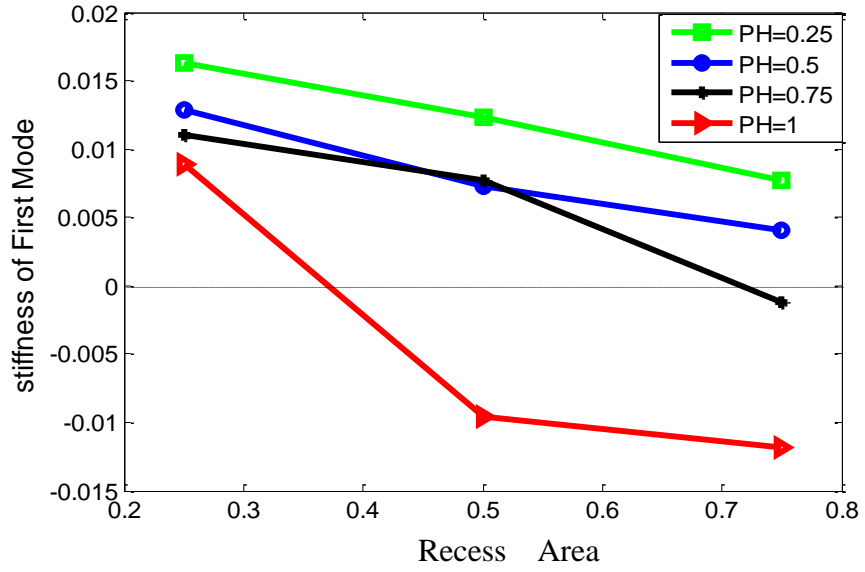
Figure 6.14 First mode stiffness on BPM disks

Figure 6.15 shows that the frequency of the third mode decreases with increases of recess AR and pattern height. The decrease of frequency may indicate a decrease of stiffness. Figure 6.16 and Figure 6.17 give the stiffness of the second and third modes when the slider is flying on different pattern designs. The results show that the stiffness decreases as recess AR increases and also decreases as pattern height increases. These results also indicate that a partially planarized pattern media is needed in order to maintain a steady HDI.
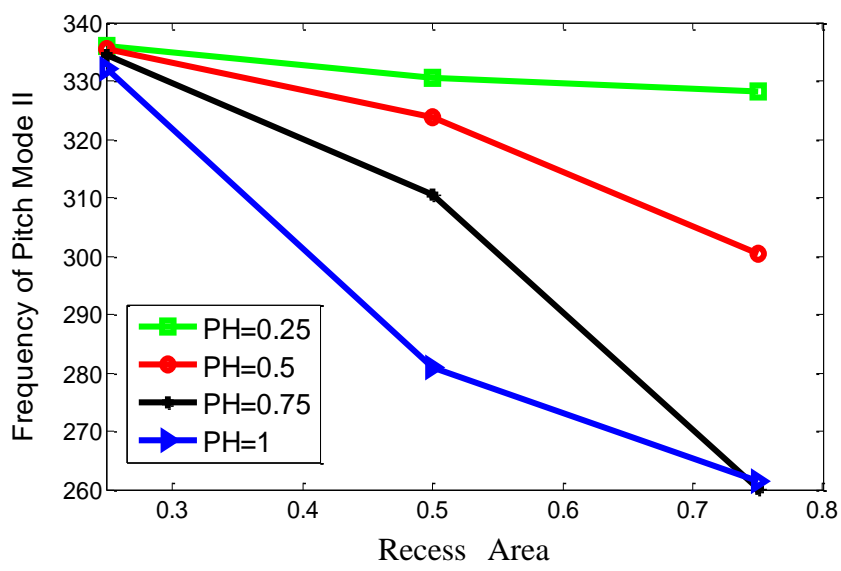
Figure 6.15 Third mode frequency on BPM disks
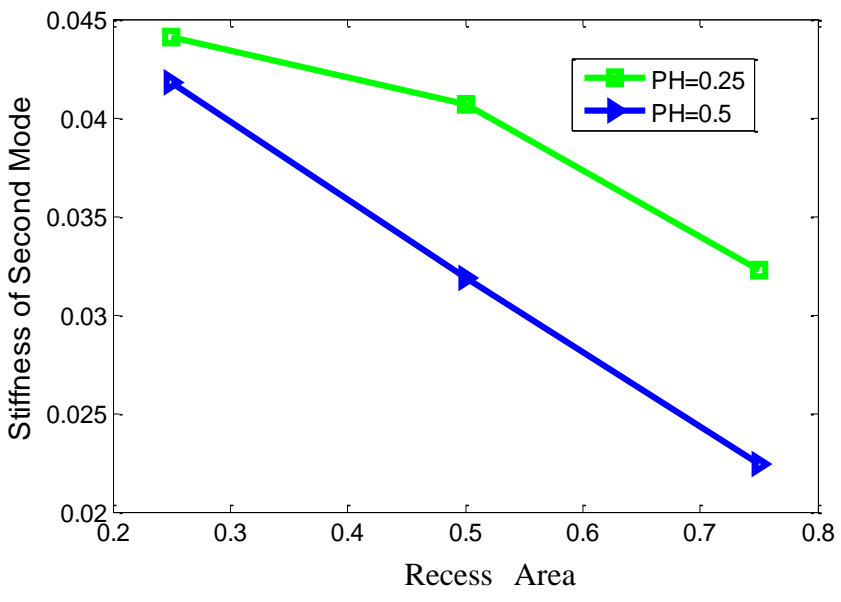
Figure 6.16 Second mode stiffness on BPM disks
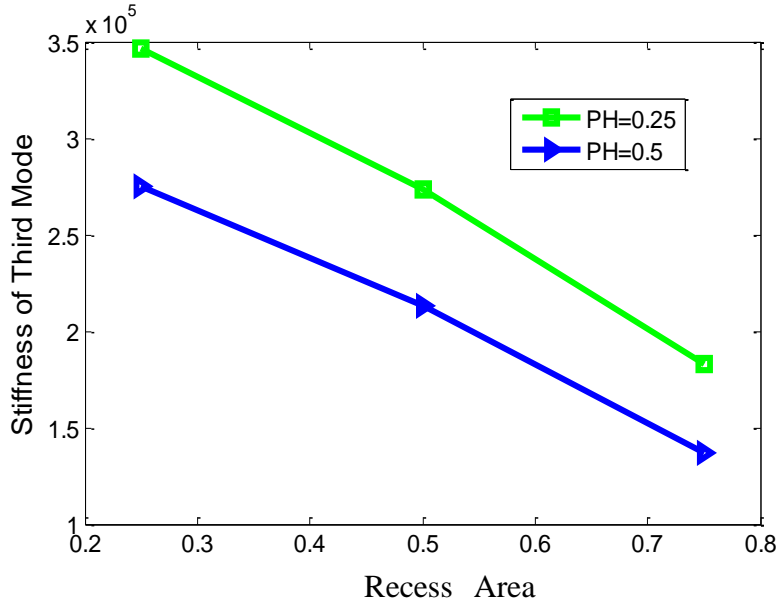
Figure 6.17 Third mode stiffness on BPM disks

6.4 Conclusion

In this chapter we first studied the slider's flying condition changes during the transition between different pattern designs on the data and servo zones. We found the slider's flying attitude changes periodically when it experiences periodical pattern transitions. The flying attitude differences depend on the pattern designs (PH and AR) and periodical pattern size. If carefully chosen two patterns, which can give the slider the same flying height, the slider's flying condition almost keeps the same during all the transitions.

We then used the system identification method to study the air bearing system's stiffness, mode shape and frequency when the slider flies over different BPM disks. It was found that the first pitch mode frequency slightly increases with an increase of recess AR and pattern height, which can be explained as the effect of further compression of the air film. The stiffness decreases as recess AR or pattern height increases. Since a negative stiffness can be realized for certain values of pattern recess AR and pattern height, we conclude that a partially planarized patterned media is needed in order to guarantee the dynamic stability of the HDI.

Chapter 7 Local Adaptive Mesh Method for Highly Complex Air Bearing Surfaces

7.1 Introduction

In modern HDDs the head disk spacing has decreased to sub-3 nm to meet the demand of higher storage density. Various technologies such as TFC, BPM and HAMR have been proposed to achieve this objective. Besides the requirement of the small spacing, the slider is also required to have a stiff air bearing and constant flying height over the entire radius of the disk. To satisfy all these requirements, the ABS designs used in current hard disk drives have complicated rail shapes, multiple etch depths and highly recessed regions between the rails. Thus the pressure distribution between the slider and disk varies greatly in the head-disk interface. Accurate and efficient simulation of the air bearing pressure is a key issue in the design of sliders. Therefore a robust numerical scheme is required to efficiently solve the generalized lubrication equation, which is used to model the air bearing between the slider and disk.

There are several numerical methods available in the literature for solving the generalized lubrication equation [75-80], such as finite difference methods, FEMs and finite volume methods. The finite difference method has been widely used because of its efficiency if uniform meshes are suitable for the ABS design. However, for sliders with quite complicated ABS designs, generating good structured meshes becomes very difficult. So the finite element or finite volume method is preferred. The FEM is often chosen due to its easily generated unstructured meshes and its ability to capture arbitrary rail geometries. However, it is hampered by its large memory required for the unstructured meshes. The finite volume method avoids this memory problem, and it is good at maintaining mass conservation of the thin film between the slider and disk. Therefore, we use the finite volume method in the present study.

Lu [77] implemented a control volume method in the CML Air Bearing Simulator to solve the lubrication equation. In this scheme a pressure profile is first obtained on an initial uniform rectangular mesh. Then the grid lines are redistributed according to the pressure gradient or geometry gradient, so that the grids are more concentrated on the areas that have high gradients of pressure or flying height. The implementation of an adaptive grid with a multi-grid method significantly enhances the accuracy and stability of the simulation. This simulator has been widely used in the HDD industry because of its accuracy. However, in this scheme a local grid redistribution of a discretization cell causes the modification of all the discretization cells along those grid lines, which may lead to a dense mesh on some areas where only sparse meshes are needed, and it thereby increases the computation time without benefits. Wu et al. [80] developed an unstructured adaptive triangular mesh generation technique, which is integrated with the control volume method and multi-grid method to form an efficient air bearing simulator. The unstructured triangular mesh makes it easy to locally refine the mesh at critical regions. However, the storage of the unstructured mesh requires a large computer memory, thereby reducing its efficiency. Lu et al. [81] constructed an adaptive grid-generating algorithm, and integrated it with the multi-grid method, to form a numerical scheme for the slider's air bearing problem. In this scheme rectangular finer meshes are constructed over nodes of the current finest grid where the global error exceeds a predetermined tolerance. Since it uses different criteria in the multi-grid method and the local adaptive method, this scheme becomes time consuming. This scheme also

uses a multi-grid method. However, it continuously increases the grid level until the global error is smaller than a predefined tolerance, so the final grid level can be as high as 10-30, and mesh size could be 2^{-30} to 2^{-10} times of the original mesh size, which makes the final mesh extremely dense. Thus it requires a longer time to finish the simulation.

In this study, we implement a new local adaptive grid-generating algorithm [82] into the CML Air Bearing Simulator [77], in order to study the steady state flying conditions of some current complicated slider designs. An initial uniform rectangular mesh is generated to obtain the pressure profile. Then two criteria, based on pressure gradient and geometry gradient, are applied to refine the local mesh on some critical areas. Finally, two sliders are used to demonstrate the accuracy and efficiency of this method.

7.2 Numerical Modeling

7.2.1 The Governing Equation and the Control Volume Method (CVM)

The governing equation for the steady state gas lubrication between a slider and a disk is the Generalized Reynolds equation, which can be written as:

$$\frac{\partial}{\partial X}\left(QPH^3 \frac{\partial P}{\partial X} - \Lambda_x PH\right) + \frac{\partial}{\partial Y}\left(QPH^3 \frac{\partial P}{\partial Y} - \Lambda_Y PH\right) = 0 . \tag{7.1}$$

The meaning of Q, P, H and $\underline{\Lambda}$ can be found in chapter 2.

The control volume method of Patankar [83] is employed to solve the generalized Reynolds equation. The integration of Eqn. (7.1) over the control volume in Figure 7.1 gives,

$$J_e - J_w + J_n - J_s = 0 \tag{7.2}$$

where J_e and J_w are $J_x \Delta Y$ evaluated at the control volume faces e and w respectively; J_n and J_s are $J_y \Delta X$ evaluated at the control volume faces n and s respectively; J_X and J_Y are:

$$J_x = \Lambda_x PH - QPH^3 \frac{\partial P}{\partial X} \tag{7.3}$$

$$J_y = \Lambda_y PH - QPH^3 \frac{\partial P}{\partial Y} \tag{7.4}$$

So the final form of the equation at grid point P is written [77]:

$$a_p P_p = a_E P_E + a_W P_W + a_N P_N + a_S P_S + b \tag{7.5}$$
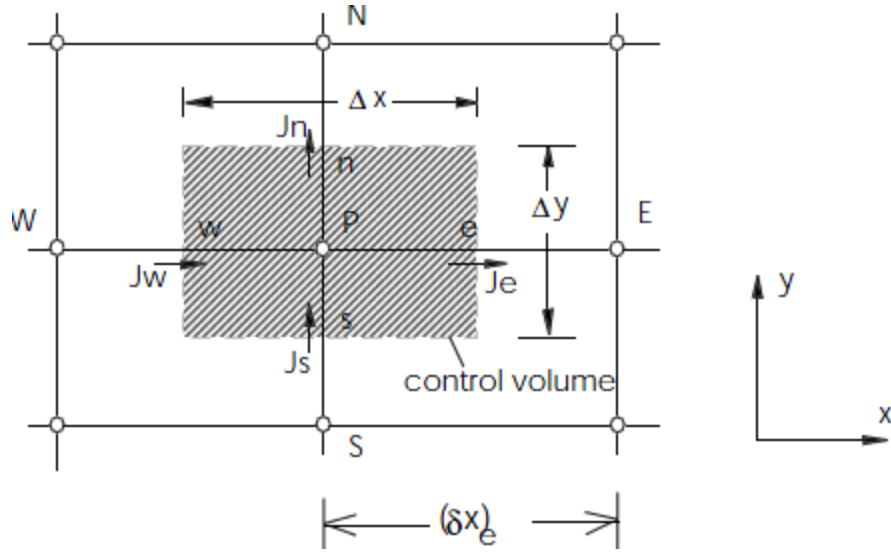
Figure 7.1 Illustration of the control volume (after Patankar [83])

7.2.2 Multi Grid Method

When solving Eqn. (7.5), a large number of grid points is needed, in order to obtain a high accuracy of the air bearing pressure, which also requires a large computation memory. So it is practical to use an iterative method. In this study we applied the FMG-FAS (full multi grid-full approximation storage) method used by Lu [77] and Shyy and Sun [84], which was designed to deal effectively with nonlinear problems.

Equation (7.5) can be expressed in the matrix form:

$$[A]\langle P \rangle = \langle b \rangle . \tag{7.6}$$

The above equation involves two levels of iterations. The inner iteration updates $\langle P \rangle$ for fixed $[A]$ and $\langle b \rangle$, while the outer iteration updates $[A]$ and $\langle b \rangle$ using the most recent $\langle P \rangle$. The computation is carried out over a series of five grids G_k, with the corresponding solutions $\langle P_k \rangle$, where k=1, 2,3,4,5, with k=5 representing the finest mesh. The FMG-FAS method can be understood by considering two levels of grid, h (fine mesh level) and H (coarse mesh level). The solution for $\langle P_h \rangle$ on grid G_h satisfies the equation

$$[A_h]\langle P_h \rangle = \langle b_h \rangle . \tag{7.7}$$

At convergence $[A_h]$ and $\langle b_h \rangle$ are based on the final solutions of $\langle P_h \rangle$. During the iteration procedure they are estimated based on the most recent values of $\langle P_h \rangle$. We denote them with an over bar, and so the pressure correction is $e_h = P_h - \bar{P}_h$. Unless the approximate solution $\langle \bar{P}_h \rangle$ satisfies Eqn. (7.7) exactly, there is a residual $\langle R_h \rangle$, which is given by:

$$\langle R_h \rangle = \langle \bar{b}_h \rangle - [\bar{A}_h]\langle \bar{P}_h \rangle. \tag{7.8}$$

Combining Eqn. (7.7) and (7.8), we write the fine grid form as:

$$[A_h]\langle \overline{P}_h + e_h \rangle - [\overline{A_h}]\langle \overline{P}_h \rangle = \langle b_h \rangle - \langle \overline{b_h} \rangle + \langle R_h \rangle. \tag{7.9}$$

Then we can transfer the above equation to grid H by applying a restriction operator $\left[I_h^H\right]$ that transmits the information from a fine grid to a coarse grid. Then Eqn. (7.9) can be written as:

$$[A_H]\langle I_h^H \overline{P}_h + e_H \rangle - [\overline{A_H}]\langle I_h^H \overline{P}_h \rangle = \langle b_H \rangle - \langle \overline{b_H} \rangle + \langle I_h^H R_h \rangle. \tag{7.10}$$

After Eqn. (7.10) is solved, the correction e_H can be transferred to the fine grid G_h, and the fine grid pressure is updated using:

$$P_h \leftarrow \overline{P}_h + I_H^h e_H. \tag{7.11}$$

where I_H^h is the interpolation operator that transfers the correction from the coarse grid to the fine grid. This procedure can be performed recursively to form the multi-grid V-cycle.

7.2.3 Local Adaptive Method

Different from the adaptive method in [77], in which the node number does not change during the mesh adaptation, this adaptive method produces new local nodes. After the pressure distribution is obtained on an initial uniform grid the pressure gradient or geometry gradient on node N is calculated on each node, and we denote it as $\varepsilon(N)$:

$$\varepsilon(N) = \begin{cases} \max\left(\frac{\partial P_N}{\partial x_N}, \frac{\partial P_N}{\partial y_N}\right), & \text{for pressure criterion} \\ \max\left(\frac{\partial H_N}{\partial x_N}, \frac{\partial H_N}{\partial y_N}\right), & \text{for geometry criterion} \end{cases}, \tag{7.12}$$

where $\frac{\partial P_N}{\partial x_N}$ is the pressure gradient in the x direction and $\frac{\partial P_N}{\partial y_N}$ is the pressure gradient in the y direction, and similarly for the geometry criterion. We first set a pre-defined tolerance Tol_1, which is usually equal to a ratio number r multiplied by the maximum pressure or geometry gradient:

$$Tol_1 = r \cdot \max(\varepsilon(N)). \tag{7.13}$$

If the gradient is larger than Tol_1, a finer mesh (mesh dimension decreased by half) gets created on this node. So the local adaptive criterion is:

$$\varepsilon(N) \geq Tol_1. \tag{7.14}$$

To demonstrate more clearly we plot a sample region in Figure 7.2; nodes 1, 2, 3, 4, 5 and 6 satisfy Eqn. (7.14), so the local meshes are produced on these six nodes (see the right figure). There are three types of nodes on this refined mesh: interior nodes, interior boundary nodes and global boundary nodes. For the interior nodes, the CVM form of Eqn. (7.7) is still applicable. However, for the interior boundary nodes, Eqn. (7.7) cannot be applied directly. Instead, a linear interpolation method is used. The pressure on this type of node is linearly interpolated from the pressure of those adjacent nodes. This is an applicable method to get information on those interior nodes. Moreover, from the results in the analysis section, we can say this method does not affect the accuracy much.
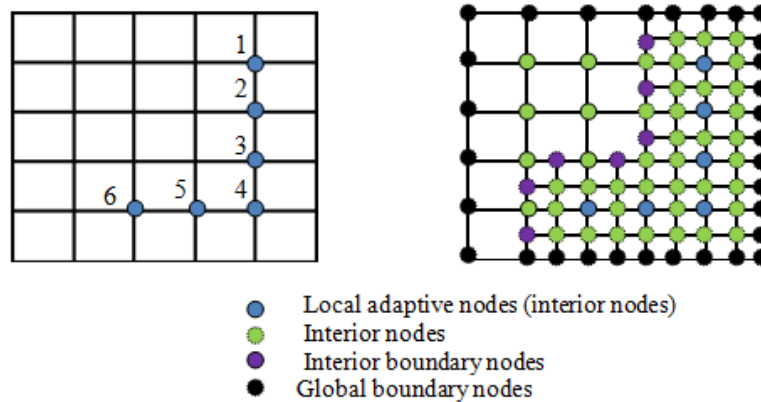
Figure 7.2 A typical two consecutive mesh structure

7.2.4 Local Adaptive Mesh Simulator Algorithm

The local adaptive method is integrated with the CVM and the multi-grid method to form a complete local adaptive multi-grid control volume algorithm. The flow chart is shown in Figure 7.3. After the simulation starts an initial uniform grid is generated, and the pressure is obtained after solving the Reynolds equation. The pressure gradient or geometry gradient is calculated (depending on the criterion option) on each node. If any of the gradients is larger than a pre-defined tolerance (Tol_1), the mesh then gets locally refined. After the new mesh is created, a new pressure profile is obtained by solving the Reynolds equation on this new mesh. The total force, considering the air bearing force, contact force, intermolecular force and electrostatic force, is calculated to determine how well it balances the suspension force. Newton iteration is applied to reduce the difference between the simulated force and suspension force until it is smaller than a predefined tolerance (Tol_2). Then the simulation is finished after adapting the mesh only once; otherwise we again follow the same steps used in the first adaptation.
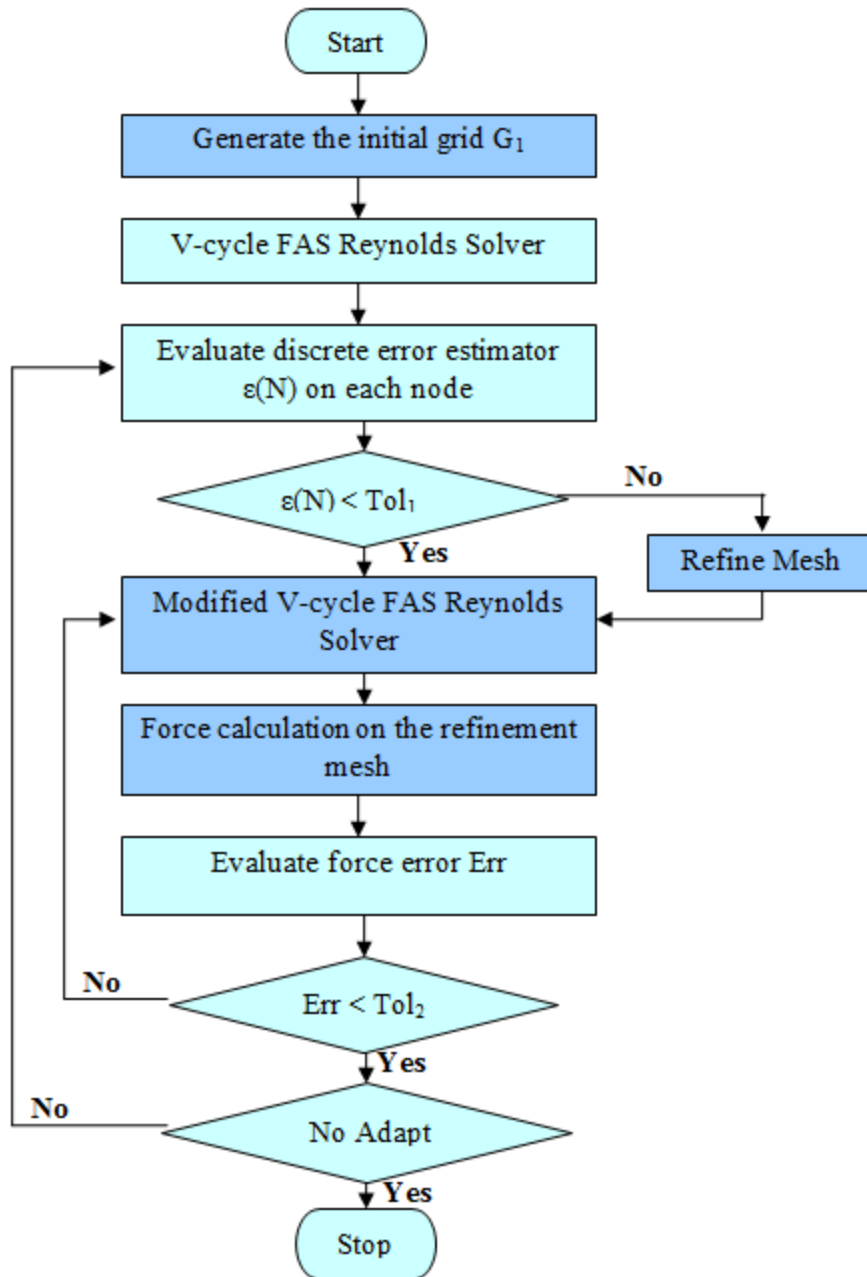
Figure 7.3 A Flow chart of local adaptive multi-grid CVM

7.3 First Slider's Flying Attitude

In this section, we use a first slider's design to test this local adaptive code, and compare the results with Lu's method [77], to study its accuracy and efficiency.

7.3.1 Uniform Mesh

If we set the "r" in Eqn. (7.13) larger than 1 in the new local adaptive mesh code, no local mesh will be generated, which means the final mesh is a uniform grid. For Lu's method we can also switch off the adaptive option so that the final mesh is a uniform grid. We compared the simulation results of Lu's method and this local adaptive method when both simulators finally employ uniform meshes. The results are shown in Table 7.1. From the comparison we see that the two simulation results (the slider's minimum flying height, nominal flying height, pitch and roll) have negligible differences. Thus, we conclude that this new local adaptive method code can also be used to simulate the air bearing problem in hard disk drives when there is no need for adaptive local mesh.

Table 7.1 Comparison with Lu's method when the final meshes are uniform grid

grid size: 145	Min FH (nm)	Nominal FH (nm)	Pitch (µrad)	Roll (µrad)
Lu's method	13.4686	10.878958	98.039114	6.5934417
Local adaptive	13.4687	10.879094	98.042139	6.5949570

7.3.2 Pressure Criterion

In order to test the accuracy of the local adaptive method of simulating the slider's flying attitude, we first need to get a reference flying height. Figure 7.4 shows the minimum flying height as a function of grid size using Lu's method. It shows the minimum flying height increases as the grid size increases and finally converges to a value, which we take as the reference flying height, since the simulation result is usually more accurate when the grid size is larger. For this case, we choose the reference flying height to be 13.6 nm.
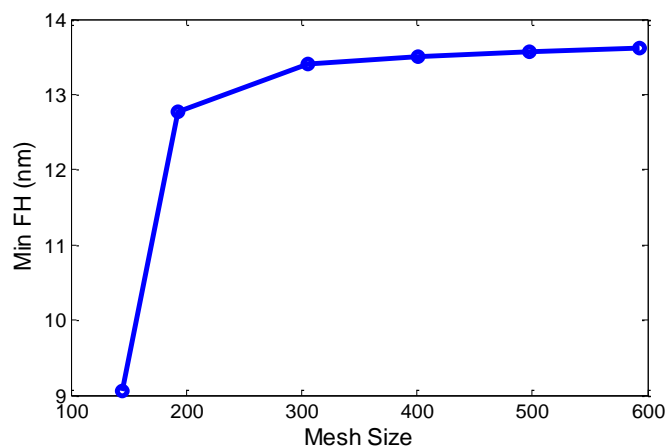
Figure 7.4 Minimum flying height with different grid size using Lu's method

Next we investigate the accuracy of the local adaptive method by setting different tolerances (Eqn. (7.13)), which lead to different local meshes. Here we use a much smaller grid size than the final mesh size in Figure 7.4. The result is shown in Figure 7.5. The x-axis is "r" in Eqn. (7.13). The blue line shows that the minimum flying height increases as the tolerance decreases. The green line shows the percentage of the minimum flying height difference from the chosen reference flying height. It shows the minimum flying height difference decreases with a decrease of tolerance, and the difference is very small (less than 0.1%). These results indicate that this new local adaptive method can give highly accurate results with a much smaller grid size. The corresponding final mesh and pressure profile for r=0.7 is plotted in Figure 7.6. We see that the local meshes are produced close to the trailing edge center or at the positions with larger pressure gradients. Although the refined meshes are only added into five areas near the slider's trailing edge, it still gives very accurate pressure profile (see Figure 7.7(1)).

Figure 7.5 Minimum flying height and its error for different tolerances (Pressure criterion)
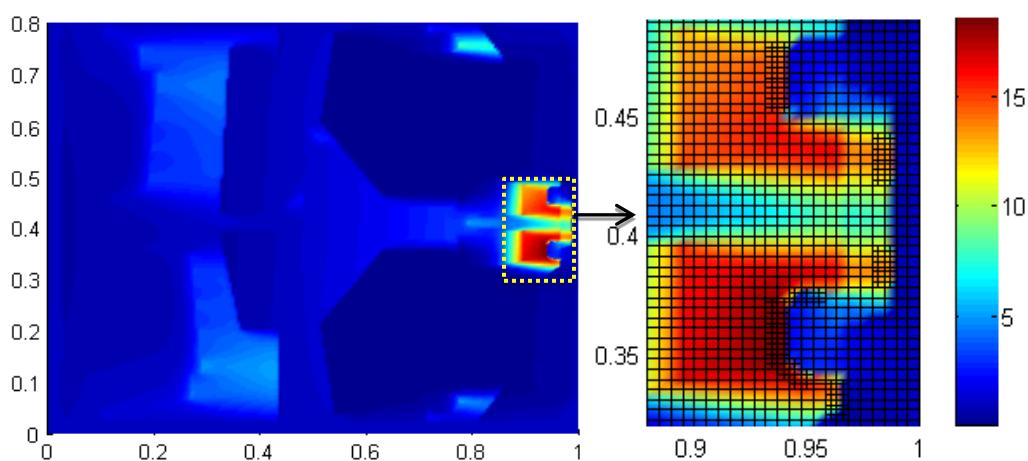
Figure 7.6 Pressure profile and corresponding local mesh for r=0.7 in Fig. 7.5

7.3.3 Geometry Criterion

In this case we use the same reference flying height of 13.6 nm as in the pressure criterion case. However, here we use the geometry criterion to produce the local meshes, which means that if the geometry gradient at a node is larger than Tol_1 then a local mesh is created on that node. The results are plotted in Figure 7.8. We draw the same conclusion as before, i.e., an accurate result can be obtained by using this local adaptive method with a much smaller grid size. The corresponding final mesh for r=0.7 is shown in Figure 7.9. The local meshes are produced at the positions with large flying height (or recess depth) changes, so they capture the ABS feature very well. There are few local refined meshes at the edge of trailing pad because the spacing gradients are not very big. However it does not affect the accuracy much in predicting the pressure distribution on the trailing pad as can be seen in Figure 7.7(2).

(1) pressure criterion   (2) Geometry criterion   (3) Lu's method
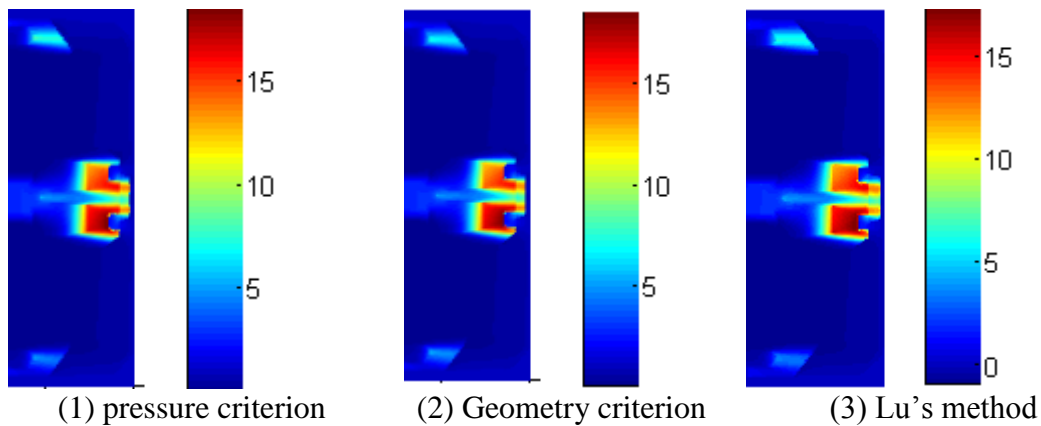
Figure 7.7 Pressure profile (Grid size 497x497 for Lu's method)
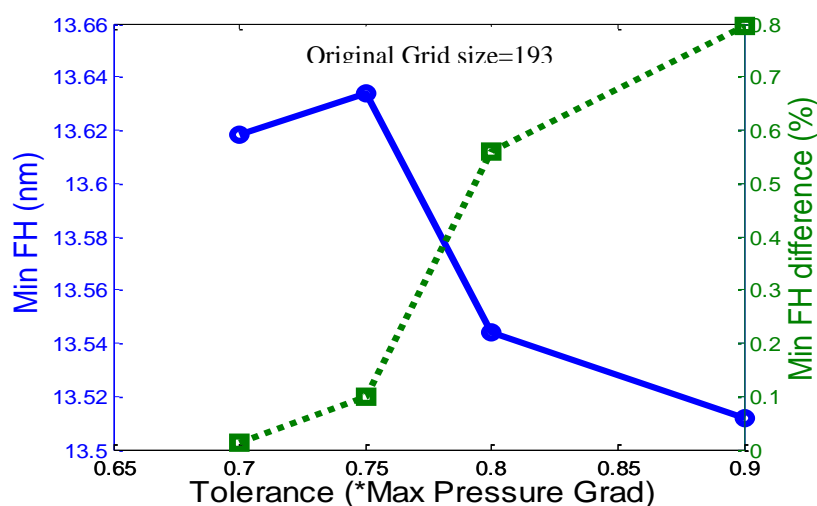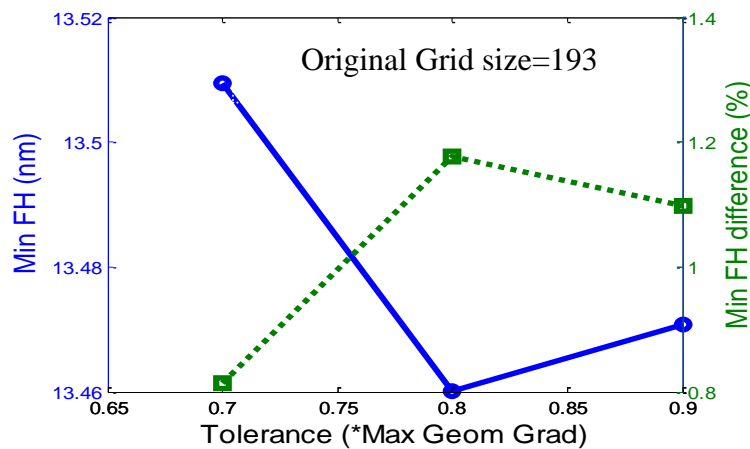

Figure 7.8 Minimum flying height and its error for different tolerances (Geometry criterion)
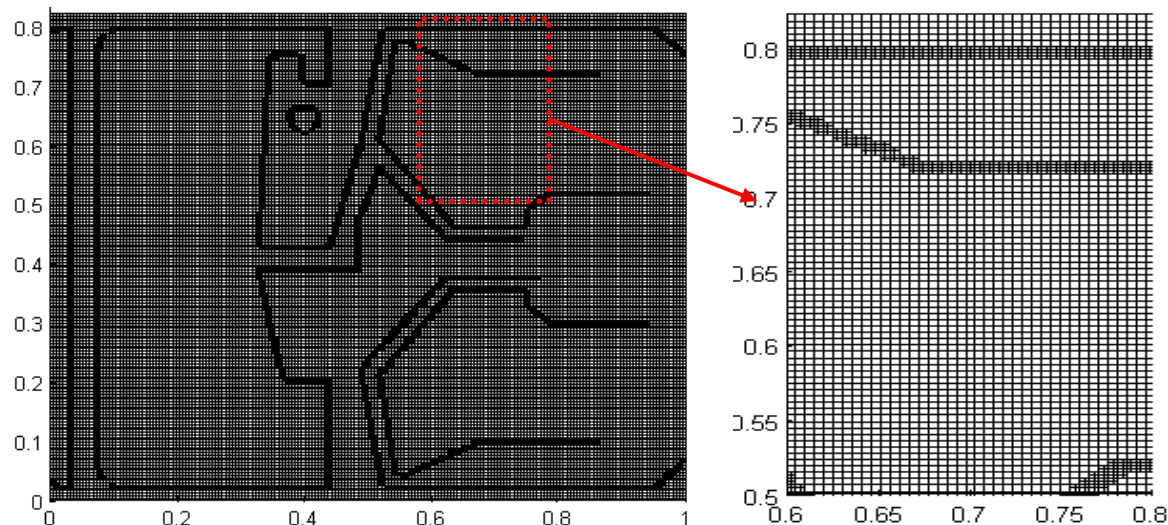
Figure 7.9 Corresponding local mesh for r=0.7 in Fig. 7.7

7.3.4 Efficiency

From the above three cases we conclude that this new local adaptive method can give highly accurate results whether there are local meshes or not. So it can be used to simulate the slider air bearing problem. In this section, we examine its efficiency, and the results are shown in Table 7.2, which shows that the local adaptive method using the pressure criterion can save computation time compared to Lu's method, so it is more efficient for the slider we used in this study. It also shows that when using the geometry criterion a longer time is required than when using the pressure criterion. That is mainly because the geometry criterion needs a smaller tolerance to get the same accuracy, which means more local meshes must be produced (see Figure 7.6 and Figure 7.9). So it is suggested to start by using the pressure criterion. However, for some immensely complicated ABS designs the geometry criterion may converge better than the pressure criterion. We will demonstrate this in the next section using a different slider design.

Table 7.2 Computation time of Lu's method and local adaptive method with the same accuracy

Three methods	Accuracy (FH different ~ 1%
Lu' Method	~5 min
Local adaptive (pressure)	~1 min
Local adaptive (geometry)	~ 6 min

7.4 Second Slider's Flying Attitude

The second slider considered has a rather complicated ABS design (we call it C_slider). We first use Lu's method to simulate the slider's flying condition. The slider's minimum flying height and the corresponding computation time with grid size is shown in Figure 7.10. It shows

that the minimum flying height does not approach a steady value as the grid size increases, especially for the case with grid size 385. The slider couldn't get a converged flying height on the disk. Moreover, the computation time for many cases is longer than what is required for most other ABS designs. We plotted the final mesh for the case with grid size 497 in Figure 7.11. It can be seen that the grid lines are concentrated near the trailing edge, slider center, outer and inner rails. For other parts there are only a few grid lines and the aspect ratio becomes extremely large (such as the zoom in part). This may be one of the reasons why the simulation does not converge very soon. The final mesh for the case with grid size 385 (no convergence case) is also plotted in Figure 7.12. It seems that the meshes are not very dense at the center rail. The mesh distribution in the dashed red boxed is not very good according to its large aspect ratio and its inability to capture the large changes of the recess depth. We also simulated the slider's flying condition using Lu's method without adaptive mesh, which means that the final mesh is uniform, and the results are shown in Figure 7.13. The minimum flying height does not approach a steady value very well using this method either especially for small grid cases. One of the reasons is that the mesh is not fine enough for the first three cases. From the above analyses, Lu's method is not very suitable for this ABS design. However, from Figure 7.10 and Figure 7.13 it appears that this slider's final steady minimum flying height is around 13 nm because the flying height converges to this value when the grid is very dense. Moreover, the experimental data from the slider's maker shows that the flying height is around 12.7 nm. Then we used the new local adaptive method with the two criteria (pressure and geometry) to simulate the flying height of the same ABS design and analyzed its convergence.
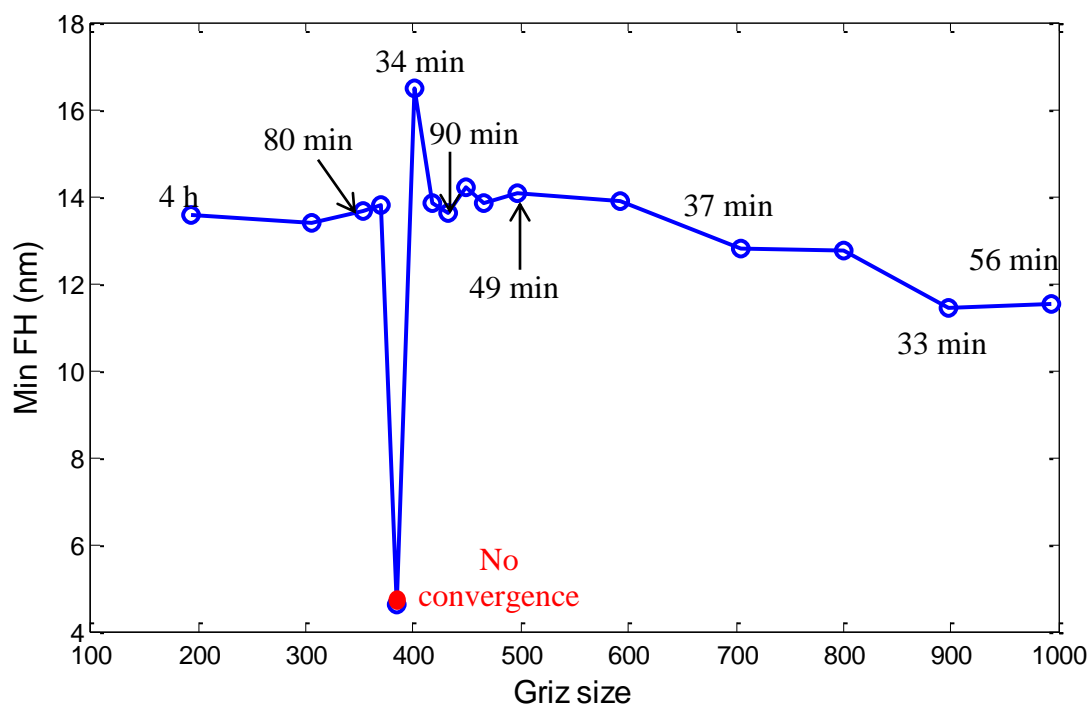
Figure 7.10 Flying heights and computation times with different grid size using Lu's method: the slider couldn't get a converged flying height on the disk with grid size 385; the cases without an indicated time have computing times less than 30 minutes.
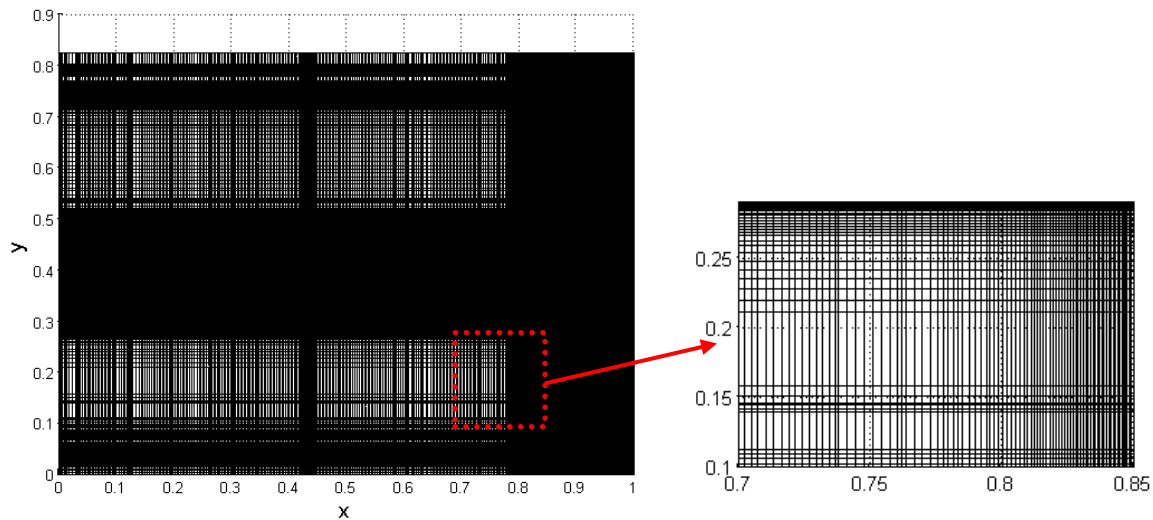
Figure 7.11 Final mesh with grid size 497 for C_slider using Lu's method
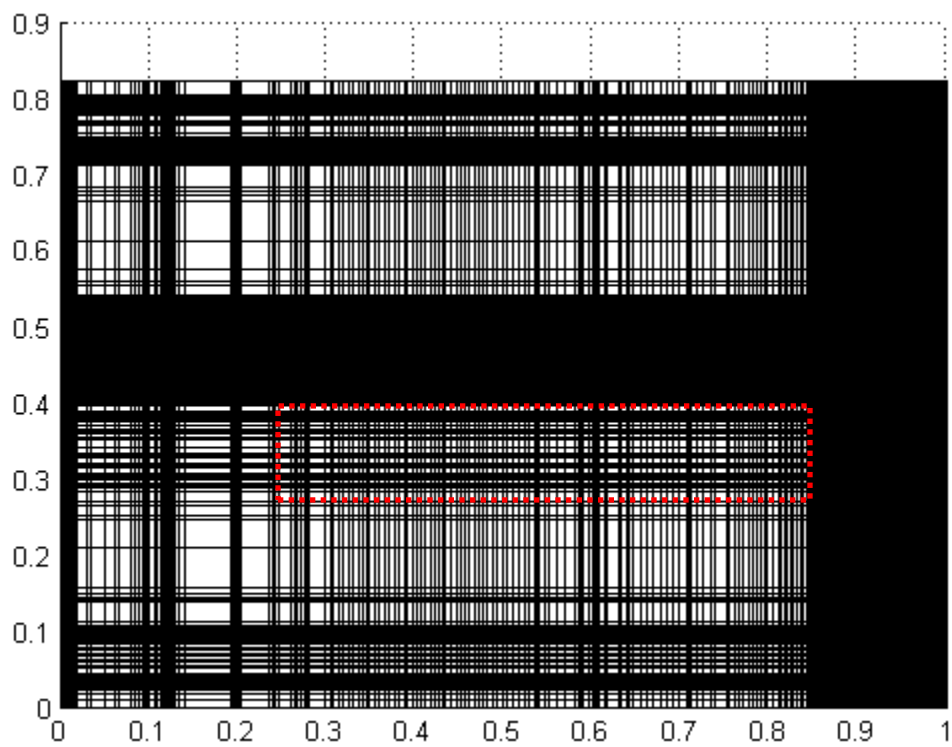
Figure 7.12 Final mesh with grid size 385 (no convergence case) for C_slider using Lu's method
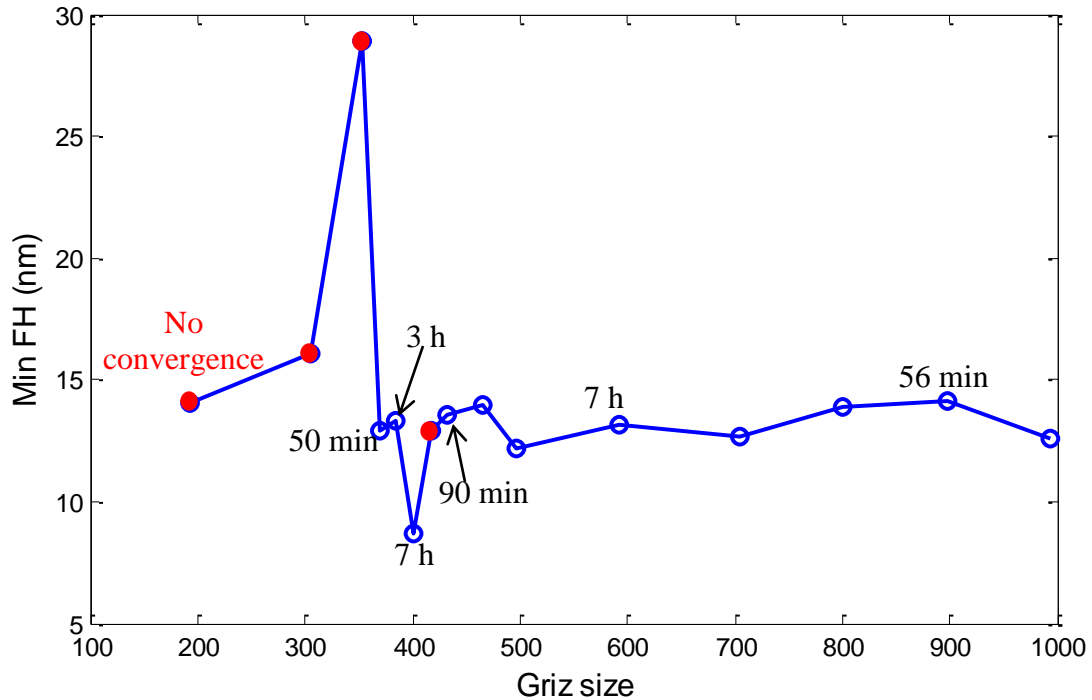
Figure 7.13 Flying heights and computation times with different grid size using Lu's method without adaptive mesh: Convegence is not obtained with grid size 193, 305, 353 and 417; the cases without an indicated time have computing times less than 30 minutes.

7.4.1 Pressure Criterion

The local adaptive simulation results for the minimum flying height with different tolerances using the pressure criterion for this C_slider are shown in Figure 7.14. We observe that the minimum flying height still does not converge very well with the reduction in the tolerance. The corresponding final mesh for r=0.2 is shown in Figure 7.15. The local meshes are produced close to the trailing edge center where there is high pressure and small flying height. The final mesh does not have a large aspect ratio, but it still cannot capture the high recess depth on the slider surface.
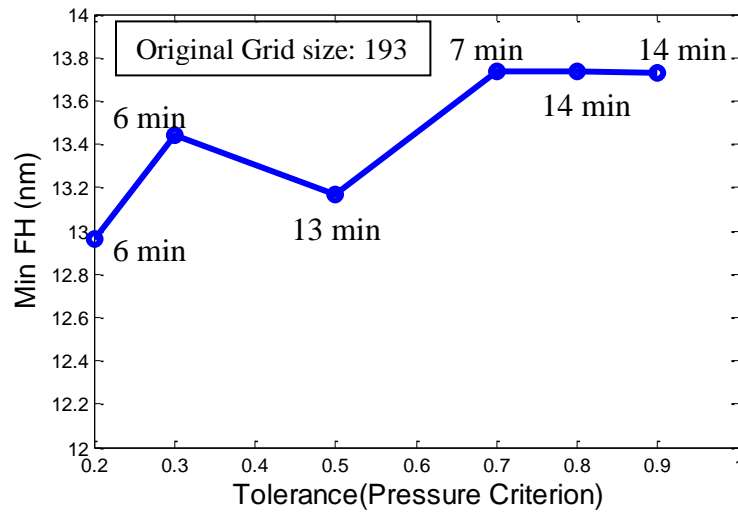
Figure 7.14 Minimum flying height with different tolerances (Pressure criterion for C_ slider)
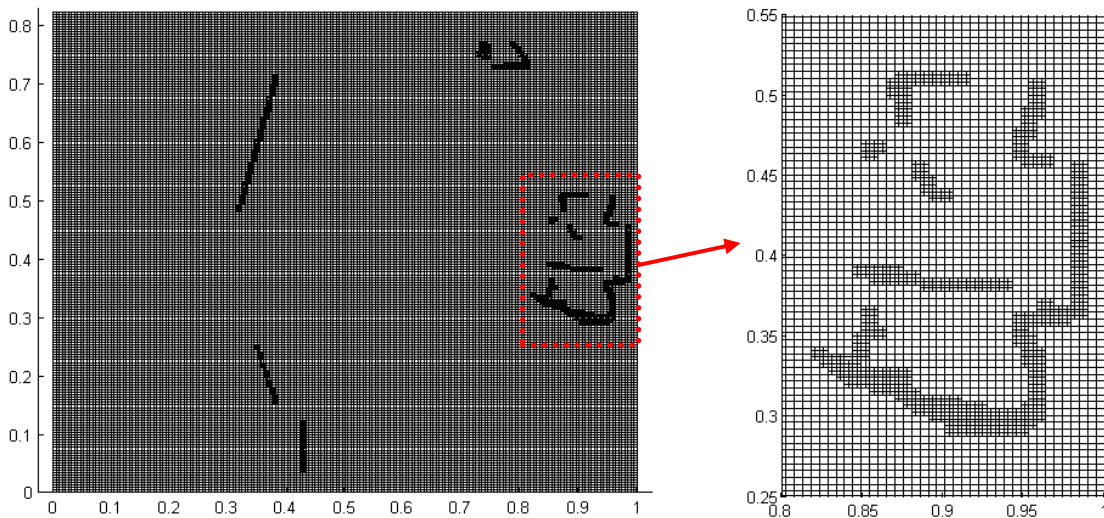
Figure 7.15 Corresponding local mesh for r=0.2 in Fig. 14

7.4.2 Geometry Criterion

The local adaptive simulated minimum flying heights, the corresponding computation times and the final element numbers with different tolerances, when using the geometry criterion, are shown in Figure 7.16. It shows that the minimum flying height converges to a constant value when decrease the tolerance. It also shows that the simulation time first decreases (r=0.9 to r=0.5), then increases (r=0.5 to r=0.2). The decrease of the criterion ratio r (r=0.9 to r=0.5) increase the local refined meshes, and the finer mesh can improve the convergence of the simulation. That is why the simulation time decreases at first. Further increasing the local meshes does not contribute much to the convergence improvement, but the simulation time increases
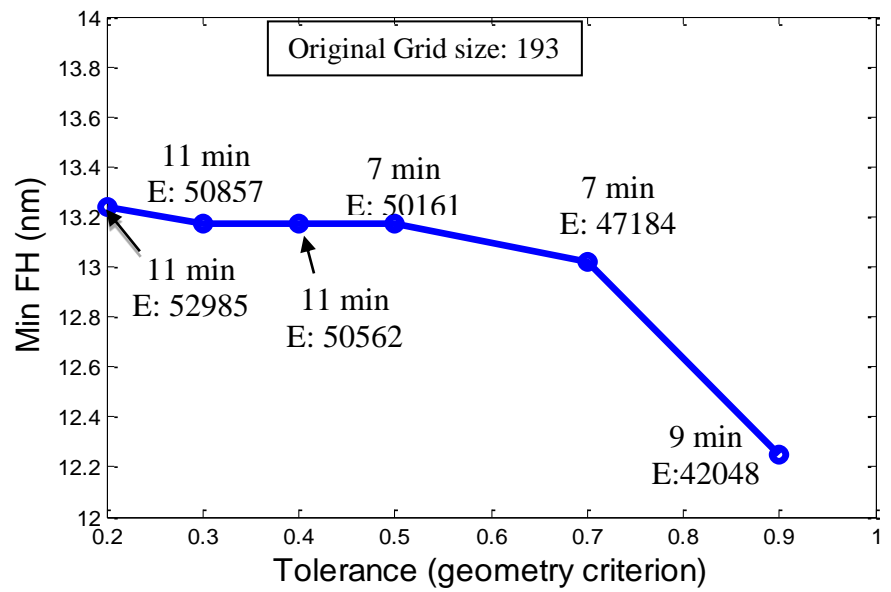
Figure 7.16 Minimum flying height with different tolerances (Geometry criterion for C_ slider); the "E" in this figure means element number.

because of the large mesh number. However compared to the Lu's method (Figure 7.10 and Figure 7.13) the computation efficiency improves significantly. So for this slider the local adaptive method with the geometry criterion is a better choice. The corresponding final mesh for r=0.2 is shown in Figure 7.17. The local meshes are produced at the positions with large recess depth transitions.
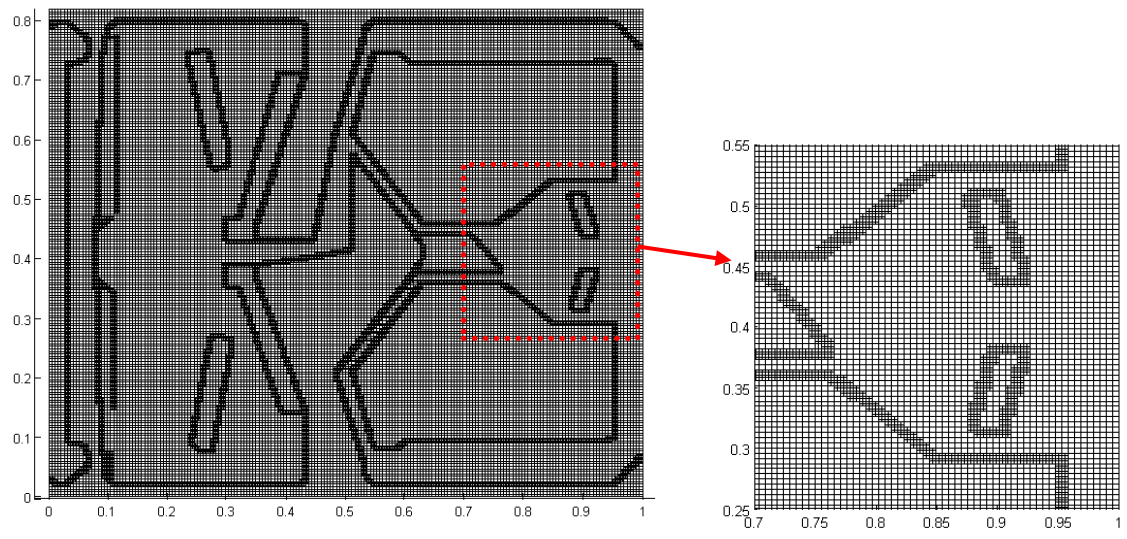
Figure 7.17 Corresponding local mesh for r=0.2 in Fig. 7.16

7.5 Conclusion

In this study we first developed a new local adaptive multi-grid control volume method to study the air bearing problem in HDDs. Then two ABS designs are used to test this method. For the first ABS design, three cases are considered: the first case with uniform mesh case, the second case with a local adaptive mesh using the pressure criterion and the third case with a local adaptive mesh using the geometry criterion. These simulations indicate that this local adaptive method saves computation time as well as retains a high accuracy.

In most cases it is not suggested to use the geometry gradient, because a smaller tolerance is required in order to obtain an accurate result and thus a longer computation time is required. However, for some designs, such as the second ABS (more complicated design), it can be seen that the local adaptive method with the geometry criterion is a better choice since the produced local meshes can capture most of the geometry sensitive regions.

Chapter 8 Conclusions and Future Work

8.1 Conclusions

A multi-body op-shock model is developed for a HDD to study the external shock effects on the mechanical and the air bearing systems. Full FE models for all the components and complete bearing models for the FDB and BB are possible, but it is likely to cause the computing extremely inefficient. A good alternative is to use the reduced model, which has been proved to be accurate enough to retain the lower frequency response of the system. A process of assembling the reduced models for all the components to get a complete system has been explained in Chapter 2. The FDB and BB are simplified as the spring-dashpot systems to save the computing efforts. The system's shock response applying the multi-body op-shock model has been investigated in Chapter 3. Analysis on different structural models (disk, disk support, actuator and full models), from component level to drive level, shows that the HAA, the disk and the base plate have played a great role on the HDI response. The study of critical shock, which is defined as the maximum shock before the HDI fails, demonstrates that the disk model predicts higher values for both positive and negative shocks. The full model, closest to the real HDD model, can also resist large positive and negative shocks. It is also found that a HDD works better when the drive drops on the floor with its top cover (negative shock case) than with its bottom (positive shock case) if there is only one slider-disk pair presented in the drive. However, the fact that there is usually more than one slider-disk pair in current HDDs means a shock which is positive for one pair becomes negative for another pair. So the difference of positive critical shock and negative critical shock does not exist for a drive with two or more slider-disk pairs. An op-shock simulation is also carried out for a TFC slider. The slider can more easily crash on the disk with TFC power on than with it off when the drive is subjected to a negative shock. That is because the thermal protrusion tip contacts the disk surface first during a negative shock event. For a positive shock event, however, the HDI responses are quite similar no matter the TFC power is on or off. That is because the failure mechanisms are the same.

A deformable ramp constraint has also been implemented to the multi-body op-shock model. It is found that the slider is not that easy to crash on the disk in the deformable ramp model than in the rigid ramp model, when the HDD is dropped on a soft floor (shock case with a longer pulse width). That is because the ramp can move up and down during the shock so that it the disk's moving direction could not be changed suddenly. Nevertheless, when the HDD is dropped on a hard floor (a shock with shorter pulse width), the residual vibrations of the disk and ramps can cause severe disk-ramp contacts or even air bearing instabilities.

This multi-body op-shock simulator is currently used by the disk drive industry to evaluate the work performance of a mobile HDD during a shock (private communications).

The BPM recording is one of the promising techniques for future disk drives to overcome superparamagnetic limit in order to increase the areal density to or even above 4 Tbit/in^2. However, the BPM can change the topography of the disk surface and thus has an effect on the flying characteristics of the air bearing sliders. Thus, a simulator to model a slider's flying condition over a BPM disk is very important. As the pattern size is on the order of nm, a mesh size of 500,000×500,000 is needed to simulate a femto slider's flying condition over a BPM disk directly. The direct method is hampered by its large memory requirement and expensive

computation. Three other methods (averaging method, Homogenization method and Taylor expansion Homogenization method) are introduced to simulate a slider's flying attitude over a BPM disk. Finally, the Taylor expansion Homogenization method is selected to investigate the air bearing dynamic stability as it is the most economical accurate method for all ranges of pattern heights. The relationship between the slider's flying height and bit pattern parameters (pattern height and recess AR) is identical with the empirical equation obtained from the experiment, which again confirms the accuracy of the Taylor expansion Homogenization method. The relationship shows that the slider's flying height decreases with the increase of the pattern height or the recess AR, which means that a pattern design with a high pattern height and a large recess AR is optimum to achieve small head media spacing and a high areal density. However, the pattern height or recess AR could not increase all the way since the air bearing instability appears in cases with high pattern heights and large recess ARs. If there are periodical transitions (like data zone and servo zone) with different pattern designs, the slider's flying attitude would also change periodically. Nevertheless, a careful selection of the two patterns, over which the slider has the same flying height, will give the slider an almost constant flying condition during all the transitions.

Finally a local adaptive multi-grid control volume method is developed to solve some air bearing problems with complicated ABS designs in hard disk drives. Two complicated ABS designs, which either need long computation time or could not get converged using the existed CML solver, are used to test this method. It is found that the new method can save computation time as well as retain high accuracy. Therefore, it is a very promising method as the ABS designs become more and more complicated in current HDDs.

8.2 Future Work

The multi-body HDD model developed in this thesis contains many details and has been made available for use to CML industry members. However, improvements to the methodology and the program will continue to be developed at CML.

We have presented the FDB in the spindle motor as a linear spring-dashpot system. This linear system is a good approximation in the case of an axial shock where the in-plane displacement of the rotor is small. However, in the case of an oblique shock there is a possibility that the rotating shaft can collide with the stationary sleeve. In such situations, the FDB model based on dynamic coefficients is no longer valid.

As seen in a ramp simulation, the disk-ramp collision force is on the same order as the shock inertia force, and it leads severe disk deformations. Moreover, the friction force between the disk and the ramps can affect the disk's rotating motion, which has adverse effects on the HDI stability. To capture the behavior in oblique and rotational shocks, it is required to model the surface contact between the stationary and rotating units. Therefore, it is necessary to model the non-linearity presented in the FDB.

In current simulator, the effects of the air bearing and other interfacial forces on the disk are ignored as it was observed that the slider's load was negligible in comparison to the inertia load during the shock. However, when slider crashes on the disk, the impact force is almost on the same order of the shock inertia force. Considering that, the slider's load becomes important and should be considered when investigating the disk's dynamic response.

Computational speed is still a big concern for the op-shock simulator. One possible direction could be done as following: creating the stationary part, which includes a housing, a base plate and a pivot shaft, as one model in the FE software. By doing this, the computation of coupling the three components can be saved. Similar simplification can be applied in the rotating part II.

Bibliography

[1]   L. D. Stevens, "The evolution of magnetic storage," *IBM J. Res. Develot.,* vol. 25, pp. 663-675, 1981.

[2]   IBM 350 disk storage unit, Available: http://www-03.ibm.com/ibm/history/exhibits/storage/storage_350.html

[3]   E. W. Pugh, "RAMAC in Historical Perspective," 2005. Available: http://www.magneticdiskheritagecenter.org/MDHC/MILESTONE/Emerson%20Pugh%20talk.pdf.

[4]   IBM 3340 direct access storage facility, Available: http://www-03.ibm.com/ibm/history/exhibits/storage/storage_3340.html

[5]   T. Coughlin, E. Grochowski, "Years of Destiny: HDD Capital Spending and Technology Developments from 2012-2016," *IEEE Santa Clara Valley Magnetics Society,* June 19th, 2012.

[6]   S. H. Charap, P-L. Lu, Y. He, "Thermal stability of recorded information at high densities," *IEEE Trans. Magn.,* vol. 33, pp. 978-983, 1997.

[7]   H.J. Richter, "Density limits imposed by the microstructure of magnetic recording media," *J. Magn.Magn. Matel.,* vol. 321, pp.: 467-476, 2009.

[8]   R. Wood, "Future hard disk drive systems," *J. Magn. Magn. Mater.,* vol. 321, pp. 555-561, 2009.

[9]   Y. Shiroishi, K. Fukuda, I. Tagawa, H. Iwasaki, S. Takenoiri, H. Tanaka, H. Mutoh, and N. Yoshikawa, "Future options for hdd storage," *IEEE Trans. Magn.,* vol. 45, pp. 3816-3822, 2009.

[10]   PCGuide. Available: http://www.pcguide.com/ref/hdd/op/index.htm, 2013.

[11]   P. E. K. Dallas W. Meyer, Joseph C. Liu, "Slider with temperature responsive transducer positioning," *United States Patent,* 1999.

[12]   T. Shiramatsu, T. Atsumi, M. Kurita, Y. Shimizu, H. Tanaka, "Dynamically controlled thermal flying-height control slider," *IEEE Trans. Magn.,* vol.44(11), pp. 3695–3697, 2008.

[13]   Hitachi Global Storage Technologies, Patterned Magnetic Media, Available: https://www1.hgst.com/hdd/research/storage/pm/index.html, 2010.

[14]   V. Ponnaganti, "Dynamics of Head-Disk Interaction in Magnetic Recording," *PhD thesis,* Stanford University, 1986.

[15]   Y. Hu, "Head-Disk-Suspension Dynamics," *PhD thesis,* UC Berkeley, 1996.

[16]   S. Kumar, V. D. Khanna, M. Sri-Jayantha, "A study of the head disk interface shock failure mechanism," *IEEE Trans. Magn.,* vol. 30(6), pp. 4155–4157, 1994.

[17]   T. Kouhei, T. Yamada, Y. Keroba, K. Aruga, "A study of head-disk interface shock resistance," *IEEE Trans. Magn.s,* vol. 31(6), pp. 3006–3008, 1995.

[18] A. M. Allen, D. B. Bogy, "Effects of shock on the head-disk interface," *IEEE Trans. Magn.,* vol. 32(5), pp. 3717–3719, 1996.

[19] J. R. Edwards, "Finite element analysis of the shock response and head slap behavior of a hard disk drive," *IEEE Trans. Magn.,* vol. 35(2), pp. 863–867, 1999.

[20] J. C. Harrison, M. D. Mundt, "Flying height response to mechanical shock during operation of a magnetic hard disk drive," *ASME J. Tribol.,* vol. 122(1), pp. 260–263, 2000.

[21] E. M. Jayson, J. M. Murphy, P. W. Smith, and F. E. Talke, "Shock and Head Slap Simulations of Operational and Nonoperational Hard Disk Drives," *IEEE Trans. Magn.,* vol. 38(5), pp. 2150–2152, 2002

[22] Q. Zeng and D. B. Bogy, "Numerical Simulation of Shock Response of Disk-Suspension-Slider Air Bearing Systems in Hard Disk Drives," *Microsyst. Technol.,* vol.8, pp. 289-296, 2002.

[23] E. M. Jayson, P. W. Smith, and F. E. Talke, "Shock modeling of the head– media interface in an operational hard disk drive," *IEEE Trans. Magn.,* vol. 39(5), pp. 2429–2431, 2003.

[24] A. N. Murthy, M. Pfabe, J. Xu, F. Talke, "Dynamic response of 1-in. form factor disk drives to external shock and vibration loads," *Microsyst. Technol.,* vol.13, pp. 1031–1038, 2006.

[25] F. F. Yap, H. Harmoko, M. Liu, N. Vahdati, "Modeling of hard disk drives for shock and vibration analysis-consideration of nonlinearities and discontinuities,", *Nonlinear Dyn.,* vol.50, pp. 717–731, 2007.

[26] M. Liu, F. F. Yap, H. Harmoko, "Shock response analysis of hard disk drive using flexible multibody dynamics formulation," *Microsyst. Technol.,* vol.13, pp. 1039-1045, 2007.

[27] M. Liu, F. F. Yap, H. Harmoko, "A model for a hard disk drive for vibration and shock analysis," *IEEE Trans. Magn.,* vol.44(12), pp. 4764–4768, 2008.

[28] P. Bhargava and D. B. Bogy, "Numerical simulation of operational-shock in small form factor hard disk drives," *ASME J. Tribol.,* vol. 129, pp. 153–160, 2007.

[29] R. Rai, and D. B. Bogy, "Effect of disk support system dynamics on the stability of head–disk interface during an operational shock in a mobile hard disk drive", *Microsyst. Technol.,* vol.18, pp. 1669-1675, 2012.

[30] Hard disk drive (HDD). Available: http://www.directindustry.com/prod/toshiba-europe-storage-device-division/hard-disk-drives-hdd-40449-367652.html

[31] H. Lamb, and R. V. Southwell, "The Vibrations of a spinning disk," Proc. Roy. Soc. London, vol. 99, pp. 272-280, 1921.

[32] R. V. Southwell, "On the free transverse vibrations of a uniform circular disc clamped at its centre: and on the effects of rotation," Proc. Roy. Soc. London, vol. 101,1921, pp. 133-153, 1922.

[33] J. Prescott, "Applied Elasticity", Dover, New York, 1946.

[34] W. D. Iwan and K. J. Stahl, "The response of an elastic disk with a moving mass system," *ASME J. Appl. Mech.*, vol. 40, pp. 445–451, 1973.

[35] W. D. Iwan and T. L. Moller, "The stability of a spinning elastic disk with a transverse load system," *ASME J. Appl. Mech.*, vol. 43(3), pp. 485–490, 1976.

[36] R. C. Benson, "Deflection of a Transversely Loaded Spinning Disk," *PhD thesis,* UC Berkeley, 1977.

[37] S. Timoshenko and S. Woinowsk-Krieger, "Theory of Plates and Shells," McGraw-Hill Book Co., New York, 1959.

[38] R. Rai, "Numerical Investigation of Operational Shocks and Vibrations in Mobile Hard Disk Drives," *PhD thesis*, 2010.

[39] G. H. Jang, J. H. Han, C. H. Seo, "Finite element modal analysis of a rotating disk–spindle system in a HDD with hydrodynamic bearings considering the flexibility of a complicated supporting structure," *Microsyst. Technol.*, vol. 11, pp. 488-498, 2005.

[40] R. J. Guyan, "Reduction of sti_ness and mass matrices," *AIAA Journal*, vol. 3(2), pp. 380, 1965.

[41] V. N. Shah and M. Raymund, "Analytical selection of masters for the reduced eigenvalue Problem," *Int. J. Numer. Meth. Eng.*, vol. 18(1), pp.89-98, 1982.

[42] G. H. Jang and S. Lee, "Determination of the dynamic coeffcients of the coupled journal and thrust bearings by the perturbation method," *Tribol. Lett.,* vol. 22(3), pp.239~246, 2006.

[43] B.-J. Shi, D.-W. Shu, S. Wang, J. Luo, H. Meng, Q. Ng, J. H.T. Lau, and R. Zambri, "Drop test simulation and power spectrum analysis of a head actuator assembly in a hard disk drive," *Int. J. Impact Eng.,* vol. 34, pp. 120-133, 2007.

[44] T. J.R. Hughes, R. L. Taylor, J. L. Sackman, A. Curnier, W. Kanoknukulchai, "A finite element method for a class of contact-impact problems," *Comput. Meth. Appl. Mech. Eng.,* vol. 8, pp. 249–276, 1976

[45] S. Fukui and R. Kaneko, "Analysis of ultra-thin gas film lubrication based on linearized boltzmann-equation: first report-derivation of a generalized lubrication equation including thermal creep flow," *ASME J. Tribol.,* vol. 110(2), pp. 253-262, 1988.

[46] S. Fukui and R. Kaneko, "A database for interpolation of poiseuille flow-rates for high knudsen number lubrication problems," *ASME J. Tribol.,* vol. 112(1), pp.78-83, 1990.

[47] V. Gupta and D. B. Bogy, "Effect of intermolecular forces on the static and dynamic performance of air bearing sliders: Part i - effect of initial excitations and slider form factor on the stability," *ASME J. Tribol.*, vol.128(1), pp. 97-202, 2006a.

[48] V. Gupta and D. B. Bogy, "Effect of intermolecular forces on the static and dynamic performance of air bearing sliders: Part ii - dependence of the stability on hamaker constant, suspension preload and pitch angle," *ASME J. Tribol.*, vol.128(1), pp. 203-208, 2006b.

[49]   J. D. Kiely and Y. T. Hsia, "Tribocharging of the magnetic hard disk drive head disk interface," *J. Appl. Phys.*, vol. 91(7), pp. 4631-4636, 2002.

[50]   J. A. Greenwood and J. B. P. Williamson, "Contact of nominally flat surfaces," *Proc. Roy. Soc. London A,* vol. 295, pp. 300-319, 1966.

[51]   P. Bhargava, "Numerical simulation of the head-disk interface in hard disk drives," *PhD thesis*, UC Berkeley, 2008.

[52]   N. M. Newmark, "A method of computation for structural dynamics," *Engng. Mech. Div., Proc. ASCE (EM 3)*, vol. 85, pp.:67-94,1959.

[53]   J. Zheng, "Dynamics and Stability of Thermal Flying-height Control Sliders in Hard Disk Drives," *PhD thesis*, UC Berkeley, 2012.

[54]   Hitachi. Ramp Load/Unload Technology in Hard Disk Drives. http://www.hgst.com/tech/techlib.nsf/techdocs/9076679E3EE4003E86256FAB005825F B/$file/LoadUnload_white_paper_FINAL.pdf, 2007c.

[55]   R. Rai, and D. B. Bogy, "Parametric study of operational shock in mobile disk   drives with disk–ramp contact," IEEE Trans. Magn., vol 47(7), pp. 1878-1881, 2011.

[56]   Z. Z. Brandic, E. A. Dobisz, T. W. Wu and T. R. Albrecht, "Patterned magnetic media: impact of nanoscale - patterning on hard disk drives," *Solid State Technology*, vol. 49,S7 Suppl., 2006

[57]   Y. Mitsuya, "A simulation method for hydrodynamic lubrication of surfaces with two-dimensional isotropic or anisotropic roughness using mixed average film thickness," *Bulletin of JSME*, vol. 27(231), pp. 2036-2044, 1984.

[58]   Y. Mitsuya and T. Koumura, "Transient-response solution applying ADI scheme to boltzmann flow-modified Reynolds-equation averaged with respect to surface-roughness," *ASME J. Tribol.*, vol. 117(3), pp. 430-436, 1995.

[59]   M. Jai, "Homogenization and 2-scale convergence of the compressible Reynolds lubrication equation modeling the flying characteristics of a rough magnetic head over a rough rigid-disk surface," *Math. Modelling Numer. Anal.*, vol. 29 (2), pp. 199-233, 1995.

[60]   G. Buscaglia, I. Ciuperca and M. Jai, "Homogenization of the transient Reynolds equation," *Asymptotic. Anal.,* vol. 32(2), pp.131-152, 2002.

[61]   V.Gupta, "Air Bearing Slider Dynamics and Stability in Hard Disk Drives," *PhD thesis,* UC Berkeley, 2007,

[62]   H. Li, H. Zheng, Y. Yoon and F. E. Talke, "Air bearing simulation for bit patterned media," *Tribol. Lett*., vol. 33, pp. 199-204, 2009.

[63]   A. Murthy, M. Duwensee and F. E. Talke, "Numerical simulation of the head / disk interface for patterned media," *Tribol. Lett.,* vol. 38, pp. 47-55, 2010.

[64]   K. S. Myo, W. Zhou, S. Yu and W. Hua, "direct monte carlo simulations of air bearing characteristics on patterned media," *IEEE Trans. Magn.,* vol. 47, pp. 2660-2663, 2011.

[65] B. E. Knigge, Z. Z. Bandic, D. Kercher, "Flying characteristics on discrete track and bit-patterned media with a thermal protrusion slider," *IEEE Trans. Magn.*, vol. 44, pp. 3656-3662, 2008.

[66] L. Li and D. B. Bogy, "Dynamics of air bearing sliders flying on partially planarized bit patterned media in hard disk drives," *Microsyst. Technol.*, vol. 17, pp. 805-812, 2011.

[67] M. Jai and B. Bou-Saïd, "A comparison of homogenization and averaging technique for the treatment of roughness in slip-flow-modified reynolds equation," *ASME J. Tribol.*, vol. 124, pp. 327-335, 2002.

[68] G. Buscaglia and M. Jai, "Sensitivity analysis and taylor expansions in numerical homogenization problems," *Numer. Math.,* vol. 85, pp. 49-75, 2000.

[69] L. Li and D. B. Bogy, "Numerical simulations of slider dynamics over patterned media with servo zones," *IEEE International Magnetics Conference*, Taipei, Taiwan, 2011.

[70] J. Hanchi, P. Sonda and R. Crone, "Dynamic fly performance of air bearing sliders on patterned media," *IEEE Trans. Magn.*, vol. 47(1), pp. 46-50, 2011.

[71] J. Li, J. Xu, and M. Kobayashi, "Slider dynamics over a discrete track medium with servo patterns," *Tribol. Lett.*, vol. 42(2), pp.233-239, 2011.

[72] Q. H. Zeng, L. S. Chen, and D. B. Bogy, "A modal analysis method for slider air bearing in hard disk drives," *IEEE Tran. of Magn.*, vol. 33, pp. 3124-3126, 1997.

[73] Q. H. Zeng and D. B. Bogy, "A modal analysis method for slider air bearing in hard disk drives," *ASME J. Tribol.*, vol.121(3), pp. 341-347, 1999.

[74] L. Li and D. B. Bogy, "Air bearing dynamic stability on bit patterned media disks," to be publies on *Microsyst Technol*, 2013.

[75] J. W. White, and A. Nigam, "A factored implicit scheme for the numerical solution of the Reynolds equation at very low spacing," *ASME J. Lubr. Technol.*, vol. 102(1), pp. 80-85,. 1980.

[76] C. Garcia-Suarez, D. B. Bogy, and F. E. Talke, ''Use of an upwind finite element scheme for air bearing calculations,'' *ASLE* SP-16, pp. 90–96, 1984.

[77] S. Lu, "Numerical Simulation of Slider Air Bearings," *PhD thesis*, UC Berkeley, 1997.

[78] E. Cha and D. B. Bogy, "A numerical scheme for static and dynamic simulation of subambient pressure shaped rail sliders," *ASME J. Trib.*, vol. 117(1), pp.36-46, 1995.

[79] P. Bhargava and D. B. Bogy, "An efficient FE analysis for complex low flying air-bearing slider designs in hard disk drives-part I: static solution," *ASME J. Trib.*, vol. 131(3), pp. 031902, 2009.

[80] L. Wu and D. B. Bogy, "Unstructured adaptive triangular mesh generation techniques and finite volume schemes for the air bearing problem in hard disk drives," ASME Journal of Tribology, vol. 122(4), pp.761-70, 2000.

[81] C.-J. Lu, S.-S. Chiou and T.-K. Wang, " Adaptive multilevel method for the air bearing problem in hard disk drives," *Tribol. Int.*, vol. 37(6), pp. 473-480, 2004.

[82] L. Li and D. B. Bogy, "Local adaptive multi-grid control volume method for the air bearing problem in hard disk drives," to be published on *J. of Tribology*, 2013.

[83] S. V. Patankar, "Numerical Heat Transfer and Fluid Flow," McGRAW-Hill, New York, 1980.

[84] W. Shyy and C.S. Sun, "Development of a pressure-correction/staggered-grid based mnulti grid solver for incompressible recirculating flows," *Comp. and Fluids*, vol. 22(1), pp. 5 l-76, 1993.